

Full-Scale Testing of the Fatigue Life of Laser Additive Manufacturing Repaired Alloy Steel Components

by

Kurtis Bell

A thesis submitted in partial fulfillment of the requirements for the degree of

Master of Science

in

Welding Engineering

Department of Chemical and Materials Engineering
University of Alberta

©Kurtis Bell, 2017

Abstract

Laser additive manufacturing, or laser cladding, is a weld overlay technique that is being increasingly used for hardfacing and corrosion resistant overlays and dimensional repairs of oil and gas, petrochemical, and mining components. However, laser cladding's use in industry is currently limited to non-critical applications due to a lack of applicable information on how laser cladding affects the fatigue life of industrial components. In this investigation, the effect of laser cladding is assessed on 2.750 inch (69.85 mm) diameter components. The material system comprises wrought quenched and tempered AISI-SAE 4140H steel overlaid with 13Cr steel, which is representative of refurbished driveshafts used in the upstream oil and gas and mining industries. The specimens were evaluated in four point rotating bending fatigue on a custom built apparatus. The effect of utilizing no preheat, 300°F (149°C), and 600°F (316°C) preheats was evaluated relative to unclad 4140H steel (control condition) using a randomized complete block experimental format. The fatigue results were analyzed using the Kaplan-Meier survival analysis and the log rank test. It was determined that laser cladding with a 300°F (149°C) or 600°F (316°C) preheat increases the fatigue life relative to unclad 4140H, or 4140H clad without the use of a preheat, at the 95.5% confidence interval.

The impact of laser cladding operations on the fatigue life of the samples was characterized through fractography, hardness surveys, and residual stress measurements by the hole drilling method. It was determined that the laser applied overlays, regardless of preheat level, had higher measured hardness than the unprocessed 4140 (overlay: $\overline{HV}_{\text{No Preheat}} = 418 \pm 21$ HV, $\overline{HV}_{300^\circ\text{F}} = 399 \pm 29$ HV, $\overline{HV}_{600^\circ\text{F}} = 430 \pm 27$ HV, 4140 substrate $\overline{HV} = 294 \pm 25$ HV). Laser processing of the samples was also found to induce large compressive residual stress states that were greater than 60% of the substrate yield stress. The increase in fatigue performance following laser cladding with a suitable pre-

heat is attributable to two factors: the large compressive residual stresses induced during laser operations, and the higher hardness of the overlay relative to the substrate material. The induced compressive residual stresses reduce the tensile stress applied during testing and create a lower effective stress state in the near surface region of the samples. The higher hardness of the overlay indicates a higher degree of resistance to the presence of discontinuities than the base material in regimes where the fatigue strength is dominated by material defects.

Preface

The material presented in this thesis comprises the author's research project under supervision of Dr. Patricio Mendez. This work has been funded by industrial sponsor Apollo-Clad Laser Cladding, a Division of Apollo Machine and Welding Ltd.

Chapter 1 is an introduction that states the goals of the research and outlines the thesis content. It was prepared in its entirety by Mr. Kurtis Bell.

Chapter 2 of this work is submitted to *Metallurgical and Materials Transactions A* as Bell, K. P., Cervera, C., Hamre, D., Findley, K.O., and Mendez P.F., 2017 "Full-Scale Testing of the Fatigue Life of Laser Additive Manufacturing Repaired Alloy Steel Components". In this portion of the study, Mr. Kurtis Bell was the principal author and was responsible for the experimental design and for the design of the custom fatigue testing apparatus, dubbed the *Rotatamatron 3000*. Mr. Bell, was also responsible for commissioning of the Rotatamatron 3000, performing the laser cladding, the testing of all samples, and subsequent analysis of the data with input from Dr. Patricio Mendez. Dr. Doug Hamre, Dr. Patricio Mendez, and Dr. Kip Findley provided technical input and support during the design and commissioning of the Rotatamatron 3000. Dr. Carlos Cervera and Dr. Patricio Mendez aided in the statistical analysis of the fatigue data. All listed authors reviewed the article prior to submission, and Dr. Mendez acted as the supervisory author.

Chapter 3 of this work has been prepared for submission to *Metallurgical and Materials Transaction A* as Bell, K.P, Findley, K.O., and Mendez, P.F., 2017 "Characterization of the Increased Fatigue Life of Alloy Steel Components Following Laser Additive Manufacturing Refurbishment". For this portion of the study, Mr. Bell was the principal author and was responsible for all experimental design, testing, and data analysis. Dr. Kip Findley and Dr. Patricio Mendez provided technical advice and support in inter-

preting the data. Both Dr. Findley and Dr. Mendez will review the article prior to submission, with Dr. Mendez acting as the supervisory author.

Six appendices are provided in order to present ancillary testing and data that could not be included in the concise framework required for publication. All appendices were entirely created, including data collection and analysis, by Mr. Bell.

To Whitney, without your love, patience, support, and understanding this work would not have been possible. You are my barefoot happiness.

“Life’s tough, but it’s a lot tougher if you’re stupid.”

- John Wayne

Acknowledgements

After nearly six years, the end is neigh. Admittedly, it feels a bit surreal. Completing my M.Sc. while working full time in industry has been an experience to say the least. It has brought with it some intense joys, some titanic struggles, some sadness, and a profoundly broadened consciousness. There have been so many people that have made this possible that I cannot hope to thank you all, but as always, I am willing to try.

First and foremost, I must thank Whitney Sloan for her vast reservoir of love, support, and above all, patience. I know the last six years have induced strain and necessitated sacrifices. Your support and understanding allowed me to pursue, and realize, a dream. It is hard to quantify how much that means to me. I love you an incredibly large amount.

It is also worth noting that none of this would have been possible without my friend and mentor Patricio Mendez. I still have no idea what possessed you to take a chance on an odd duck like myself, but thank-you. A thousand times, thank-you. Whether it was defending my Dionysian approach to UBC to the FGSR, or helping me navigate my personal and professional woes, you've always been willing to fight the good fight on my behalf. I hope that in the end I was worth all the headaches. Please know that my gratitude knows no bounds, and that you will always have a friend in me.

To my friends and family - thank you. Without your support I probably would've lost my tenuous grip on sanity. At times the line between functioning member of society and guy who yells at magpies in the park was a thin one, but you never let me cross it. Dad and Noemi, Mom and Glen, you guys have always been there for me, whether for a pep talk, a hot-tub, or a sanity check. Ditto for my Canadian and expatriate friends: Lawry, Grayson, Jyll, Drew, Gentry, Declan, John "welshy" Liddiard, Teddy, Doug and many others; thank you for helping me blow off steam, and for taking care of me at my best and my most helpless.

This work also would not have happened without the sponsorship of Apollo-Clad, A Division of Apollo Machine and Welding Ltd. The success of this project can be attributed in large part to three men: Doug Hamre, Andre Lahote, and John Liddiard. Doug, thank you for your willingness to mentor me and intercede on my behalf. You were a big part of why I loved my job, and I hope that we can continue talking rugby over IPA for years to come. To Andre, you wily Frenchman, thank you so much for taking the time to show me how things should be done. Without you, the Rotatamatron would never have been a reality. To John, thank you. You are a great friend and an awesome machinist, but your banter could use some work...

I would also like to mention the contribution from the CCWJ; I have seldom met a better group of people. No matter how busy or hectic things were, or were about to be, everyone in the lab always had time to help with a problem, provide advice, and otherwise help a part-timer navigate academia. Of special note are Gentry, Nairn, Steve, and Goetz. You guys made the CCWJ what it is (literally), and I feel privileged to have had the chance to both work you and enjoy a few "personal" pitchers with you all. I know I have made friends for life.

Finally, I would like to thank IRISNDT in general, and Matt Bell in particular. Although you didn't have any skin in the game, you have been far more supportive than could rightly be expected - Excelsior!

Table of Contents

| | | |
|----------|--|-----------|
| 1 | Introduction | 1 |
| 1.1 | Introduction | 1 |
| 1.1.1 | Introduction | 1 |
| 1.1.2 | Thesis Objective | 2 |
| 1.1.3 | Thesis Outline | 2 |
| 2 | Full-Scale Testing of the Fatigue Life of Laser Additive Manufacturing Repaired Alloy Steel Components | 3 |
| 2.1 | Introduction | 3 |
| 2.2 | Experimental Procedure | 6 |
| 2.2.1 | Fatigue tester | 6 |
| 2.2.2 | Laser Cladding | 6 |
| 2.2.3 | Materials System | 8 |
| 2.2.4 | Statistical Design | 8 |
| 2.2.5 | Specimen Geometry | 10 |
| 2.2.6 | Rotatamatron Calibration | 11 |
| 2.2.7 | Test Procedure | 11 |
| 2.3 | Results | 14 |
| 2.4 | Statistical Analysis | 15 |
| 2.5 | Discussion | 17 |
| 2.6 | Conclusions | 18 |
| 2.7 | Acknowledgements | 19 |
| 3 | Characterization of the Increased Fatigue Life of Alloy Steel Components Following Laser Additive Manufacturing Refurbishment | 20 |
| 3.1 | Introduction | 20 |
| 3.2 | Experimental Design | 23 |
| 3.3 | Results | 24 |
| 3.3.1 | Material Characterization | 24 |
| 3.3.2 | Fractography | 27 |
| 3.3.3 | Residual Stress | 31 |
| 3.3.4 | Hardness Mapping | 34 |

| | | |
|----------|--|------------|
| 3.4 | Discussion | 35 |
| 3.5 | Conclusions | 37 |
| 3.6 | Acknowledgements | 38 |
| 4 | Conclusions and Future Work | 40 |
| 4.1 | Conclusion and Summary of Findings | 40 |
| 4.2 | Recommended Future Work | 42 |
| | Bibliography | 43 |
| | Appendix A – Full Scale Monotonic Tensile Testing | 48 |
| 6.1 | Introduction | 48 |
| 6.2 | Tensile Test Results | 49 |
| 6.3 | 4140H Material Test Report (MTR) | 51 |
| | Appendix B – Surface Finish Characterization | 53 |
| 7.1 | Introduction | 53 |
| 7.2 | Experimental Methodology | 56 |
| 7.3 | Profilometry Results | 57 |
| 7.3.1 | Laser Clad Surface Roughness Data | 59 |
| 7.4 | Statistical Analysis: Mann-Whitney Test | 69 |
| 7.5 | Conclusion | 70 |
| | Appendix C – Fractography | 71 |
| 8.1 | Introduction | 71 |
| 8.2 | Optical Fractography | 72 |
| 8.2.1 | Block A | 72 |
| 8.2.2 | Block B | 75 |
| 8.2.3 | Block C | 77 |
| 8.2.4 | Block D | 80 |
| 8.2.5 | Block E | 82 |
| 8.2.6 | Block F | 84 |
| 8.3 | SEM Fractography | 89 |
| | Appendix D – Residual Stress Data | 107 |
| 9.1 | Introduction | 107 |
| 9.2 | Residual Stress Data | 108 |
| | Appendix E – Hardness Survey Data | 129 |
| 10.1 | Introduction | 129 |
| 10.2 | Hardness Data | 130 |

| | |
|------------------------------------|------------|
| Appendix F – MatLab Scripts | 135 |
| 11.1 Introduction | 135 |
| 11.2 Main MatLab Program | 135 |
| 11.3 Functions | 141 |

List of Tables

| | | |
|-----|--|----|
| 2.1 | Typical Laser Parameters | 8 |
| 2.2 | Material chemistry of the 4140 steel used in experiments (wt%) | 8 |
| 2.3 | Mechanical properties of the 4140 steel used in experiments as reported on the materials test report (MTR) | 8 |
| 2.4 | 13Cr overlay chemistry (wt. %) | 9 |
| 2.5 | Actual stress initially applied during testing. Target stress was 55 ksi (379MPa) | 15 |
| 2.6 | Fatigue life of samples tested | 16 |
| 3.1 | Composition of the 4140 steel used in experiments (wt%) | 23 |
| 3.2 | Mechanical properties of the 4140 steel used in experiments as reported on the materials test report (MTR) | 23 |
| 3.3 | 13Cr overlay chemistry (wt. %) | 23 |
| 6.1 | Full scale monotonic tensile test data for each sample condition | 49 |
| 7.2 | Summary of measured surface roughness parameters | 57 |
| 7.3 | Notch radii measured on both the control and clad surface finish specimens | 58 |
| 8.4 | Running stress, cycles to failure, and failure initiation location for the Block A samples | 72 |
| 8.5 | Running stress, cycles to failure, and failure initiation location for the Block B samples | 75 |
| 8.6 | Running stress, cycles to failure, and failure initiation location for the Block C samples | 77 |
| 8.7 | Running stress, cycles to failure, and failure initiation location for the Block D samples | 80 |
| 8.8 | Running stress, cycles to failure, and failure initiation location for the Block E samples | 82 |
| 8.9 | Running stress, cycles to failure, and failure initiation location for the Block F samples | 84 |

List of Figures

| | | |
|-----|---|----|
| 2.1 | The Rotatamatron 3000 Fatigue Testing Apparatus. | 7 |
| 2.2 | Rotatamatron 3000 Load Application Schematic. | 7 |
| 2.3 | Process Schematic for the treatment conditions within each block | 10 |
| 2.4 | Geometry of the finished machined test specimen (left of center) and the specimen geometry before cladding (right of center) | 11 |
| 2.5 | Strain gauged blank sample used for the calibration trials | 12 |
| 2.6 | Load calibration curve for the Rotatamatron 3000. The dashed lines correspond to 95% probability | 12 |
| 2.7 | Residuals for the calibration data regression analysis showing no clear bias in the coefficient of determination (R^2) | 13 |
| 2.8 | Measured central load (lb) plotted versus time for the entire F block control specimen test run at 5 Hz | 14 |
| 2.9 | Kaplan-Meier Survival plot for the four treatment conditions. Comparison of cumulative incidence of fracture between groups using the log rank test yielded $p=0.045$ | 17 |
| 3.1 | 300°F preheat specimen (RS-30) Overview of the overlay layer including the interpass and 4140H substrate fusion lines. Etched with ASTM E407 Etchant No. 220. | 25 |
| 3.2 | 600°F preheat specimen (RS-60) Overview of the overlay layer including the interpass and 4140H substrate fusion lines. Etched with ASTM E407 Etchant No. 220. | 26 |
| 3.3 | No preheat specimen (RS-NO) Overview of the overlay layer including the interpass and 4140H substrate fusion lines. Etched with ASTM E407 Etchant No. 220. | 27 |
| 3.4 | Block F control specimen (F-CO) fatigue initiation at a non-metallic inclusion | 29 |
| 3.5 | Block B control specimen (B-CO) fatigue initiation at the surface as indicated by the presence of a radially orientated ratchet mark. | 29 |
| 3.6 | Fatigue failure initiation location on the no preheat specimen of Block A (A-NO) | 30 |
| 3.7 | 300°F preheat specimen of Block B (B-30) subsurface fatigue fracture initiation in the substrate material HAZ | 30 |

| | | |
|------|--|----|
| 3.8 | 300°F preheat specimen of Block B (B-30) failure initiated at a non-metallic inclusion typical of steel making. | 31 |
| 3.9 | 300°F (149°C) Preheat (RS-30) sample residual stress profile | 32 |
| 3.10 | 600°F (316°C) Preheat (RS-60) sample residual stress profile | 33 |
| 3.11 | No Preheat (RS-NO) sample residual stress profile | 33 |
| 3.12 | 600°F (316°C) Preheat (RS-60) sample residual stress profile | 34 |
| 3.13 | Average specimen hardness as a function of depth. For each of the laser processed samples, the fusion line was located ≈ 1 mm (0.040 inch) below the surface | 35 |
| 6.1 | Finished machined monotonic tensile coupon geometry | 49 |
| 6.2 | Full scale monotonic tensile curves for each sample condition | 50 |
| 7.3 | Schematic representation of surface roughness as a series of adjacent notches with a lower degree of stress concentration. From Ref. [37] | 55 |
| 7.4 | Pre-cladding Surface finish specimen dimensions. Following laser processing the sample was machined flush to the 2.830 inch diameter | 56 |
| 7.5 | Clad sample specimen 1 roughness profile | 59 |
| 7.6 | Notch radii measurements at location 1, which was randomly selected from the profile shown in Figure 7.5 | 60 |
| 7.7 | Notch radii measurements at location 2, which was randomly selected from the profile shown in Figure 7.5 | 60 |
| 7.8 | Notch radii measurements at location 3, which was randomly selected from the profile shown in Figure 7.5 | 61 |
| 7.9 | Notch radii measurements at location 4, which was randomly selected from the profile shown in Figure 7.5 | 61 |
| 7.10 | Clad sample specimen 2 roughness profile | 62 |
| 7.11 | Notch radii measurements at location 1, which was randomly selected from the profile shown in Figure 7.10 | 62 |
| 7.12 | Notch radii measurements at location 2, which was randomly selected from the profile shown in Figure 7.10 | 63 |
| 7.13 | Notch radii measurements at location 3, which was randomly selected from the profile shown in Figure 7.10 | 63 |
| 7.14 | Notch radii measurements at location 4, which was randomly selected from the profile shown in Figure 7.10 | 64 |
| 7.15 | Control sample specimen 1 roughness profile | 64 |
| 7.16 | Notch radii measurements at location 1, which was randomly selected from the profile shown in Figure 7.15 | 65 |
| 7.17 | Notch radii measurements at location 2, which was randomly selected from the profile shown in Figure 7.15 | 65 |
| 7.18 | Notch radii measurements at location 3, which was randomly selected from the profile shown in Figure 7.15 | 66 |

| | | |
|------|--|----|
| 7.19 | Notch radii measurements at location 4, which was randomly selected from the profile shown in Figure 7.15 | 66 |
| 7.20 | Control sample specimen 2 roughness profile | 67 |
| 7.21 | Notch radii measurements at location 1, which was randomly selected from the profile shown in Figure 7.20 | 67 |
| 7.22 | Notch radii measurements at location 2, which was randomly selected from the profile shown in Figure 7.20 | 68 |
| 7.23 | Notch radii measurements at location 3, which was randomly selected from the profile shown in Figure 7.20 | 68 |
| 7.24 | Notch radii measurements at location 4, which was randomly selected from the profile shown in Figure 7.20 | 69 |
| 8.25 | A-CO coupon showing fracture initiation at a "dent" in the surface . . . | 72 |
| 8.26 | A-CO coupon OD view of initiating dent | 73 |
| 8.27 | A-NO fracture initiation at an entrapped oxide located at the fusion line | 73 |
| 8.28 | A-30 fracture initiation at an multiple adjacent entrapped oxides located at the fusion line | 74 |
| 8.29 | A-60 fracture initiation at a circular entrapped oxide in the overlay region | 74 |
| 8.30 | B-CO coupon fracture initiation at the surface | 75 |
| 8.31 | B-NO coupon fracture initiation at a fusion line oxide | 76 |
| 8.32 | B-30 coupon fracture initiation at a non metallic inclusion located in the HAZ | 76 |
| 8.33 | B-60 coupon fracture initiation at a non metallic inclusion located in the HAZ | 77 |
| 8.34 | C-CO coupon fracture initiation at the surface | 78 |
| 8.35 | C-NO coupon fracture initiation at a fusion line oxide inclusion | 78 |
| 8.36 | C-30 coupon fracture initiation at a non metallic inclusion in the HAZ . . | 79 |
| 8.37 | C-60 coupon fracture initiation at a fusion line discontinuity | 79 |
| 8.38 | D-CO coupon fracture initiation at multiple locations on the surface . . . | 80 |
| 8.39 | D-NO coupon fracture initiation at a fusion line discontinuity | 81 |
| 8.40 | D-30 coupon fracture initiation at multiple fusion line oxide inclusions . . | 81 |
| 8.41 | D-60 coupon fracture initiation at the surface | 82 |
| 8.42 | E-CO coupon fracture initiation at the surface | 83 |
| 8.43 | E-30 coupon fracture initiation at a non metallic inclusion located in the HAZ | 83 |
| 8.44 | E-60 coupon fracture initiation at the fusion line | 84 |
| 8.45 | F-CO coupon overview showing initiation and propagation of multiple fractures | 85 |
| 8.46 | F-CO coupon surface initiation of the lower fracture shown in 8.45 | 86 |
| 8.47 | F-CO coupon surface initiation of the upper fracture shown in Figure 8.45. | 86 |
| 8.48 | F-NO coupon showing adjacent initiation at a fusion line discontinuity and a non metallic inclusion located in the HAZ | 87 |

| | | |
|------|--|-----|
| 8.49 | F-30 coupon showing multiple fracture initiation locations. The fracture initiated at location 1 dominated failure | 87 |
| 8.50 | Location 1 of the F-30 fracture shown in Figure 8.49. Initiation occurred at a non metallic inclusion in the HAZ | 88 |
| 8.51 | F-60 coupon fracture initiated at porosity in the overlay layer | 88 |
| 8.52 | B-CO Secondary electron (SE) image showing the presence of a ratchet mark perpendicular to the sample surface. | 89 |
| 8.53 | B-30 SE image showing fracture initiation at a non metallic inclusion located in the substrate HAZ. | 90 |
| 8.54 | B-30 SE image of the non-metallic inclusion | 91 |
| 8.55 | B-60 SE image showing fracture initiation at a non metallic inclusion located in the substrate HAZ. | 95 |
| 8.56 | B-60 SE image of the inclusion shown in Figure 8.55. EDS analysis was conducted at the locations marked 1 and 2. | 96 |
| 8.57 | B-NO SE image showing fracture initiation at a non metallic inclusion located at the fusion line. | 99 |
| 8.58 | B-NO Back Scatter Electron (BSE) image showing fracture initiation at a non metallic inclusion located at the fusion line. | 100 |
| 8.59 | B-NO high magnification SE image of the fusion line inclusion. | 101 |
| 8.60 | B-NO high magnification BSE image of the fusion line inclusion. | 102 |
| 8.61 | F-CO SE image of the initiation location shown in Figure 8.46. Initiation occurred at a near surface non metallic inclusion. | 105 |
| 9.62 | RS-30 strain gauge rosette installation | 107 |
| 9.63 | R-CO measured strain Vs. Depth | 108 |
| 9.64 | RS-CO tabulated strain data | 109 |
| 9.65 | RS-CO combination strain data | 110 |
| 9.66 | RS-CO estimated standard error in the combined strain calculations . . . | 110 |
| 9.67 | RS-CO Cartesian stresses versus depth. The X-direction corresponds to the longitudinal axis of the sample | 111 |
| 9.68 | RS-CO magnitude of the maximum and minimum stresses as a function of depth below the surface | 111 |
| 9.69 | RS-CO direction in which the maximum stresses act relative to the longitudinal axis of the sample (reference direction) | 112 |
| 9.70 | RS-CO direction in which the minimum stresses act relative to the longitudinal axis of the sample (reference direction) | 113 |
| 9.71 | R-NO measured strain Vs. Depth | 114 |
| 9.72 | RS-NO tabulated strain data | 114 |
| 9.73 | RS-NO combination strain data | 115 |
| 9.74 | RS-NO estimated standard error in the combined strain calculations . . . | 115 |
| 9.75 | RS-NO Cartesian stresses versus depth. The X-direction corresponds to the longitudinal axis of the sample | 116 |

| | | |
|-------|---|-----|
| 9.76 | RS-NO magnitude of the maximum and minimum stresses as a function of depth below the surface | 116 |
| 9.77 | RS-NO direction in which the maximum stresses act relative to the longitudinal axis of the sample (reference direction) | 117 |
| 9.78 | RS-NO direction in which the minimum stresses act relative to the longitudinal axis of the sample (reference direction) | 118 |
| 9.79 | R-30 measured strain Vs. Depth | 119 |
| 9.80 | RS-30 tabulated strain data | 119 |
| 9.81 | RS-30 combination strain data | 120 |
| 9.82 | RS-30 estimated standard error in the combined strain calculations . . . | 120 |
| 9.83 | RS-30 Cartesian stresses versus depth. The X-direction corresponds to the longitudinal axis of the sample | 121 |
| 9.84 | RS-30 magnitude of the maximum and minimum stresses as a function of depth below the surface | 121 |
| 9.85 | RS-30 direction in which the maximum stresses act relative to the longitudinal axis of the sample (reference direction) | 122 |
| 9.86 | RS-30 direction in which the minimum stresses act relative to the longitudinal axis of the sample (reference direction) | 123 |
| 9.87 | R-60 measured strain Vs. Depth | 124 |
| 9.88 | RS-60 tabulated strain data | 124 |
| 9.89 | RS-60 combination strain data | 125 |
| 9.90 | RS-60 estimated standard error in the combined strain calculations . . . | 125 |
| 9.91 | RS-60 Cartesian stresses versus depth. The X-direction corresponds to the longitudinal axis of the sample | 126 |
| 9.92 | RS-60 magnitude of the maximum and minimum stresses as a function of depth below the surface | 126 |
| 9.93 | RS-60 direction in which the maximum stresses act relative to the longitudinal axis of the sample (reference direction) | 127 |
| 9.94 | RS-60 direction in which the minimum stresses act relative to the longitudinal axis of the sample (reference direction) | 128 |
| 10.95 | RS-CO microhardness survey matrix overview | 130 |
| 10.96 | RS-CO microhardness map | 131 |
| 10.97 | RS-NO hardness survey matrix overview | 131 |
| 10.98 | RS-NO microhardness map | 132 |
| 10.99 | RS-30 microhardness survey matrix overview | 132 |
| 10.10 | RS-30 microhardness map | 133 |
| 10.10 | RS-60 microhardness survey matrix overview | 133 |
| 10.10 | RS-60 microhardness hardness map | 134 |

Chapter 1

Introduction

1.1 Introduction

1.1.1 Introduction

The use of laser additive manufacturing to repair and refurbish industrial components is rapidly growing worldwide. When applied as layers on pre-shaped large components, the laser additive manufacturing process is typically referred to as laser cladding. Laser Cladding is a fusion weld overlay technique in which a consumable, usually blown powder, is deposited upon a substrate using a laser as a heat source. The process is typified by low heat input, minimal dilution or intermixing with the substrate, a small heat affected zone (HAZ), and fine grained overlay microstructure. These characteristics make it ideal for hardfacing, dimensional repair, and dissimilar welding applications in the oil and gas and mining sectors [1].

The application of laser cladding as a method for the repair of components subject to fatigue is currently hampered by the lack of understanding and reliable data on the fatigue behaviour of repaired components. As a result, many industrial components that are repaired through laser cladding do not include the refurbished layer in the remaining life calculations. Overly conservative fatigue life calculations can lead to increased scrap

rates and increased process downtime. This work is the first published assessment of the effect of laser cladding on the rotating bending fatigue of full-scale components.

1.1.2 Thesis Objective

This project is designed to determine the effect of laser cladding on the four point rotating bending fatigue performance of full scale AISI-SAE 4140H alloy steel components.

1.1.3 Thesis Outline

This is a paper-based thesis with each chapter comprising its own set of objectives and conclusions. Chapter 2 focuses on the fatigue testing, and details the equipment design, calibration, experimental methodology, fatigue test data, and the statistical analysis performed. In Chapter 3, the effect of laser cladding on the fatigue performance of alloy steel is characterized through fractography, residual stress measurements by the hole drilling method, and hardness mapping. Chapter 4 provides a summation of major findings and suggests future work.

Detailed appendices are provided in order to present ancillary testing and data that could not be included in the concise framework required for publication.

Chapter 2

Full-Scale Testing of the Fatigue Life of Laser Additive Manufacturing Repaired Alloy Steel Components

2.1 Introduction

The use of laser additive manufacturing to repair and refurbish industrial components is rapidly growing worldwide. When applied as layers on pre-shaped large components, the laser additive manufacturing process is typically referred to as laser cladding, and has been used industrially since Weerasinghe and Steen described the principles, method, and characteristics of laser cladding a mild steel substrate [2]. Laser Cladding is a fusion weld overlay technique in which a consumable, usually blown powder, is deposited upon a substrate using a laser as a heat source. The process is typified by low heat input, minimal dilution or intermixing with the substrate, a small heat affected zone (HAZ), and fine grained overlay microstructure. These characteristics make it ideal for hardfacing, dimensional repair, and dissimilar welding applications in the oil and gas and mining sectors [1].

The application of laser cladding as a method for the repair of components subject to fatigue is currently hampered by the lack of understanding and reliable data on the

fatigue behaviour of repaired components. As a result, many industrial components that are repaired through laser cladding do not include the refurbished layer in the remaining life calculations. Overly conservative fatigue life calculations can lead to increased scrap rates and increased process downtime. This work is the first published assessment of the effect of laser cladding on the rotating bending fatigue of full-scale components.

Full scale rotating bending fatigue testing is important because the microstructure and residual stresses resulting from laser cladding play a dominant role in fatigue life, and they are determined by the actual size of the clad layer and the component being repaired [3]. Full scale testing has not yet been assessed because available rotating bending fatigue testing machines are typically limited to standard samples sizes that range between 6.0 mm – 9.5mm (0.236 inch – 0.374 inch) in diameter [4]. Dieter suggests that for fatigue considerations in bending, the outer 5% of the component dominates fatigue life [3]. For the 1 mm of intended thickness of laser cladding in this project, a sample of at least 40 mm in diameter is needed to include the entire overlay layer in the critical region. While existing rotating bending testing machines are able to test near surface treatments such as shot-peening, chroming, nitriding, etc., no available machine is able to test the sample size needed. Work conducted by Alam has shown that fatigue cracking of laser clad components depends on both the macro load conditions and on the type, location, and orientation of defects or discontinuities [5]. The use of standard sized samples would over emphasize the effect of near surface features relative to the potential effects of the fusion line, HAZ, or subsurface defects or discontinuities. The use of small diameter samples for alloy steel material systems is further complicated by the development of thermal cycles during laser processing that are neither feasible for, nor representative of, large scale industrial components. The challenge of standard/small-scale samples is evident in the work of Kohler, where laser cladding of 10.3 mm diameter AISI 4140 steel samples resulted in a HAZ that spanned the specimen diameter [6]. Similar issues were

encountered in the work of Shi Da Sun et al., where laser cladding of 7 mm thick AISI 4340 specimens was found to degrade the bulk mechanical properties of the sample which are typically unaffected in laser cladding of large industrial components [7].

Attempts to address the size effect through large scale non-rotating bending studies have been undertaken by numerous researchers such as Koehler, Whitney, and Tuominen [8–10]. Non-rotating bending allows for the use of available machines and an appropriate sample size; however, it is limited by the fact that the maximum load is always applied at the same points in the sample, and is not distributed over the entire periphery as in real applications. By exposing the entire periphery to the maximum stress a larger volume of material is exposed to the critical stress range which increases the likelihood of encountering a critical flaw [11]. A further limitation of the tests of Koehler, Whitney, and Tuominen, is that the stress ratio was always $R \geq 0$ (non-reversed bending), while in rotating bending $R = -1$.

Similar to non-rotating bending fatigue tests, the use of large scale rotating cantilever bending testing is problematic for evaluating welds as the method of load application often produces a local stress maximum at the attachment of the cantilever that is not distributed over the length of the sample. Various methods to overcome the deficiencies of cantilever testing, such as the method of machining notches at set locations used by Hutasoit [12] have been employed; however, these methods cannot capture the heterogeneity of welded (or laser clad) components [13].

For this research, a full-scale four-point rotating bending fatigue testing machine was designed and built, and the effect of laser cladding 13Cr stainless steel overlays on the fatigue performance of AISI-SAE 4140 specimens 2.750 inch (69.85 mm) in diameter was evaluated. The fatigue life of laser-clad components was found to be superior to the unclad alloy steel. Improved fatigue performance is in stark contrast to the decrease in fatigue life found in previous research using other fatigue testing techniques less repre-

sentative of the actual applications [7–10, 12].

2.2 Experimental Procedure

2.2.1 Fatigue tester

To facilitate four-point rotating bending fatigue testing of full scale samples it was necessary to design and build a custom apparatus. The fatigue test frame, dubbed the Rotatamatron 3000, is shown in Figure 2.1. It is designed to operate at a maximum speed of 500 rpm under a maximum applied load of 30,000 lbf (133kN). A load of this magnitude produces a uniform stress of approximately 100 ksi (690 MPa) for a steel specimen with the geometry shown in Figure 2.4. The machine is displacement controlled and operates at a constant deflection set at the start of the test with a stress ratio, R , equal to -1. The machine is instrumented with three load cells, one at the head of the hydraulic ram used to apply the load, and one beneath each bearing assembly; all data is logged with an integrated PLC. A schematic diagram of the load application assembly is shown in Figure 2.2.

2.2.2 Laser Cladding

Laser cladding of the specimens was carried out at Apollo-Clad, a Division of Apollo Machine and Welding. A 6 kW CO₂ laser with coaxial powder delivery was utilized with the specimens manipulated relative to the laser using a 5-axis CNC positioning system. Specimens were preheated to the assigned temperatures of 300°F (149°C) and 600°F (316°C) with the use of a propane torch. Temperatures were monitored with the use of a contact thermocouple; no preheat maintenance was conducted once cladding was begun. Nominal laser parameters utilized are listed in Table 2.1.

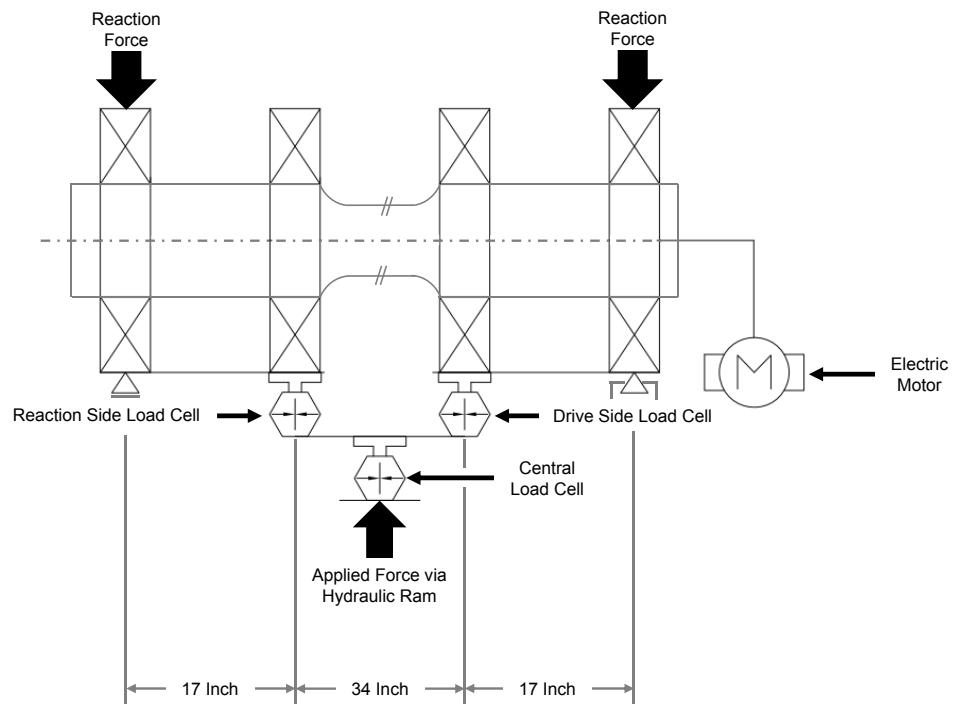


Figure 2.2: Rotatamatron 3000 Load Application Schematic.

Table 2.1: Typical Laser Parameters

| Laser Power | Travel Speed | Powder Flow Rate |
|-------------|------------------------|------------------|
| 3 kW – 4 kW | 1.52 m/min (60 in/min) | 17.5 g/min |

2.2.3 Materials System

The fatigue specimens were AISI-SAE 4140H wrought alloy steel in the quenched and tempered condition. All specimens were fabricated from the same heat of steel that was austenitized at 1475°F (802°C), quenched in water, and tempered at 1125°F (607°C) by the manufacturer. The chemistry of the steel is given in Table 3.1, and the properties as reported on the materials test report (MTR) are given in Table 3.2. The steel was clad with Apollo-Clad 1407 powder (13Cr steel) with the chemical composition listed in Table 3.3.

Table 2.2: Material chemistry of the 4140 steel used in experiments (wt%)

| C | Mn | P | S | Si | Cr | Ni | Mo | Cu | Al | V |
|------|------|------|-------|-------|------|------|-----|------|-------|-------|
| 0.42 | 0.98 | 0.01 | 0.022 | 0.026 | 0.98 | 0.14 | 0.2 | 0.19 | 0.028 | 0.006 |

Table 2.3: Mechanical properties of the 4140 steel used in experiments as reported on the materials test report (MTR)

| σ_Y MPa (ksi) | UTS MPa (ksi) | % Elong | % RA | Hardness(BHN) |
|----------------------|---------------|---------|------|---------------|
| 899 (130.4) | 1,030 (149.4) | 15.4 | 49.6 | 328 |

2.2.4 Statistical Design

It has been well established that the fatigue performance of a given material can be affected by variables such as fabrication techniques, surface finish, and environmental factors. In the context of fatigue experiments, the variables that affect fatigue strength

Table 2.4: 13Cr overlay chemistry (wt. %)

| C | Si | Cr | Fe |
|-----|------|----|-----|
| 0.1 | 0.75 | 12 | Bal |

can be divided into two categories: treatment conditions and nuisance variables. A treatment condition connotes an intentional action, such as shot-peening, heat treatment, laser cladding etc., whose effect on the fatigue performance is to be measured either absolutely, or relative to another treatment condition [14]. A nuisance variable is a test factor whose effect on the specimen is unintended and undesirable. To accurately measure the effect of the intended treatment conditions, fatigue test programs must be designed so that the influences of nuisance variables can be isolated from the measured treatment condition effects [14]. In this study, a randomized complete block (RCB) experimental format was utilized for this purpose.

The RCB consisted of a total of 24 samples that were arranged into six blocks of four distinct treatment conditions. The first treatment condition corresponded to control specimens with neither cladding nor preheat. The other three conditions corresponded to the application of cladding with no preheat, a 300°F (149°C) preheat, and a 600°F (316°C) preheat. Each block consisted of a sample of each of the four treatment conditions plus a spare sample. All samples were tested at the same initial operating stress of 55 ksi (379 MPa).

The blocks, labeled A – F, were randomly assigned to six bars of the same heat of AISI-SAE 4140H steel. Each treatment condition, control (-CO) no preheat (-NO), 300°F preheat (-30), 600°F preheat (-60), and a spare sample (-SP) were randomly assigned to a length of material within each bar. Each bar was subsequently processed in random order according to the process schematic shown in Figure 2.3. At each process level, the order in which the samples were processed was mechanically randomized and the same

opera

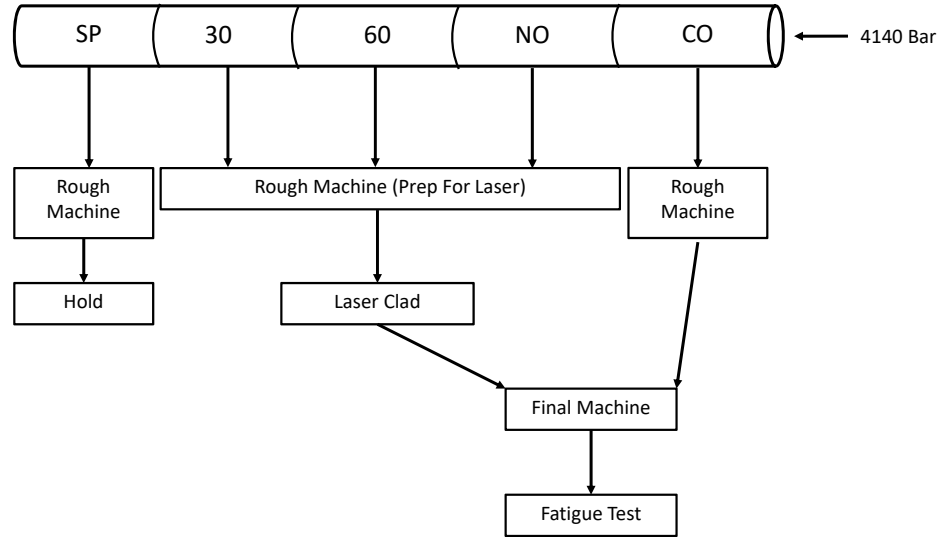


Figure 2.3: Process Schematic for the treatment conditions within each block

2.2.5 Specimen Geometry

The laser clad specimens were undercut as shown in Figure 2.4. They were subsequently clad with three layers of overlay to give an average deposited weld metal thickness of 0.110 inch (2.79 mm). The samples were machined back to the finished diameter of 2.750 inch \pm 0.002 inch (69.85mm \pm 0.05mm) as shown in Figure 2.4. The control and spare specimens were rough machined to the oversized "as clad dimension" (\approx 2.900 inch / 73.66 mm), and all samples were final machined under the same parameters. This way, it was ensured that all samples would have similar roughness and lathe-induced residual stresses after final machining. The spare specimens were held at the rough machine stage and were utilized to replace other specimens that were scrapped during cladding or machining operations. In the final machining step the samples were polished with 240-grit emery paper to a 16 μ -in Ra surface finish with the induced scratches orientated circumferentially.

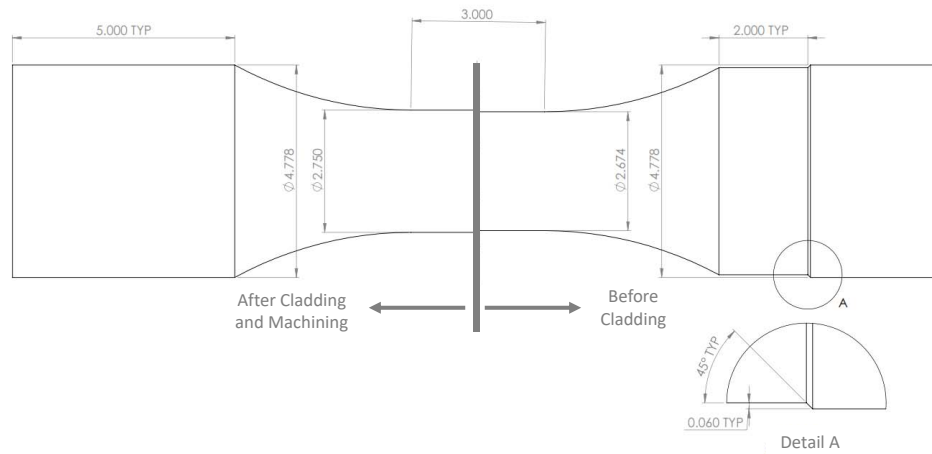


Figure 2.4: Geometry of the finished machined test specimen (left of center) and the specimen geometry before cladding (right of center)

2.2.6 Rotatamatron Calibration

The Rotatamatron was calibrated by instrumenting a blank sample of 4140 alloy steel of the same finished machined geometry shown in Figure 2.4 with strain gauges as shown in Figure 2.5. The blank sample was subject to displacements that produced loads ranging from 5000 lb to 28,000 lb, just below the level to yield the sample. Multiple, independent, calibration runs were performed to correlate the applied load to the induced stress using a modulus value of 30×10^6 psi (210 GPa) [15]. Regression analysis of the applied load and calculated stress values produced a coefficient of determination (R^2) value of 99.6%. The regression analysis and the residuals plot of the calibration data are given in Figures 2.6 and 2.7 respectively.

2.2.7 Test Procedure

The load profile during a typical test run is shown in Figure 2.8. After the sample is installed in the testing machine, it is run at a reduced load of approximately 3,500 lb, as measured on the central load cell, for approximately 20,000 cycles. Loads of this

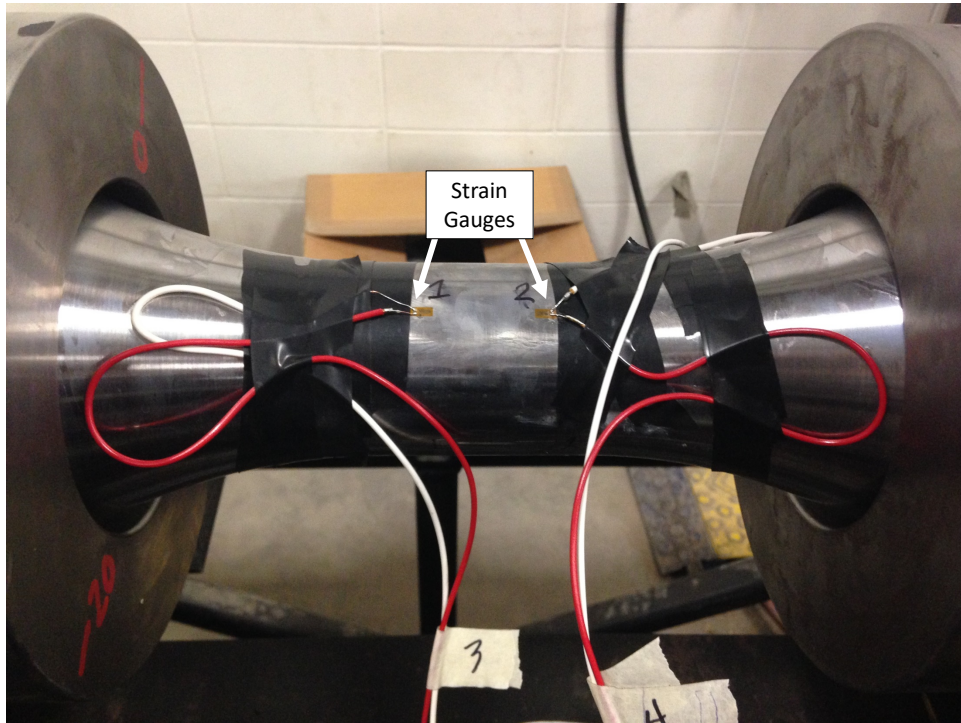


Figure 2.5: Strain gauged blank sample used for the calibration trials

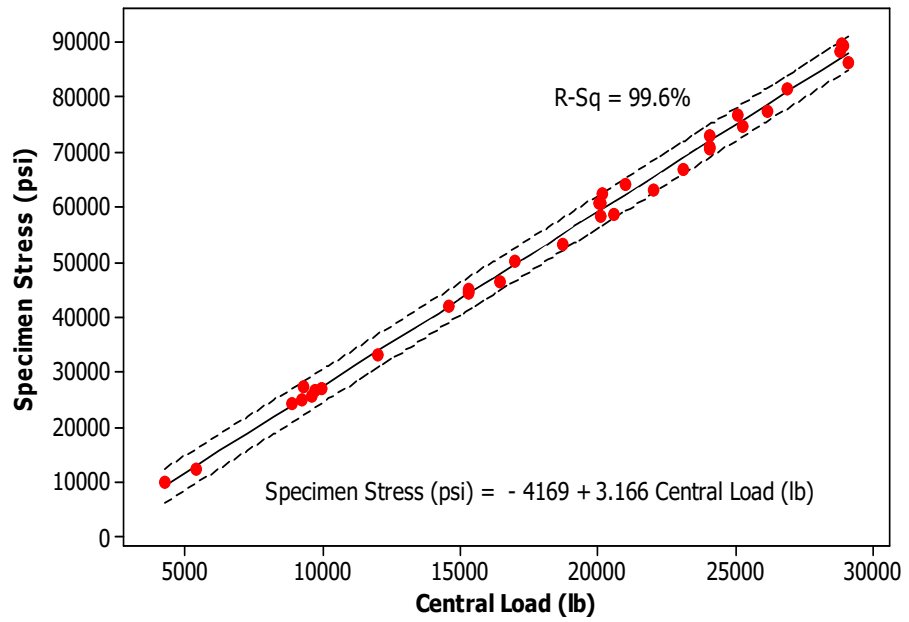


Figure 2.6: Load calibration curve for the Rotatamatron 3000. The dashed lines correspond to 95% probability

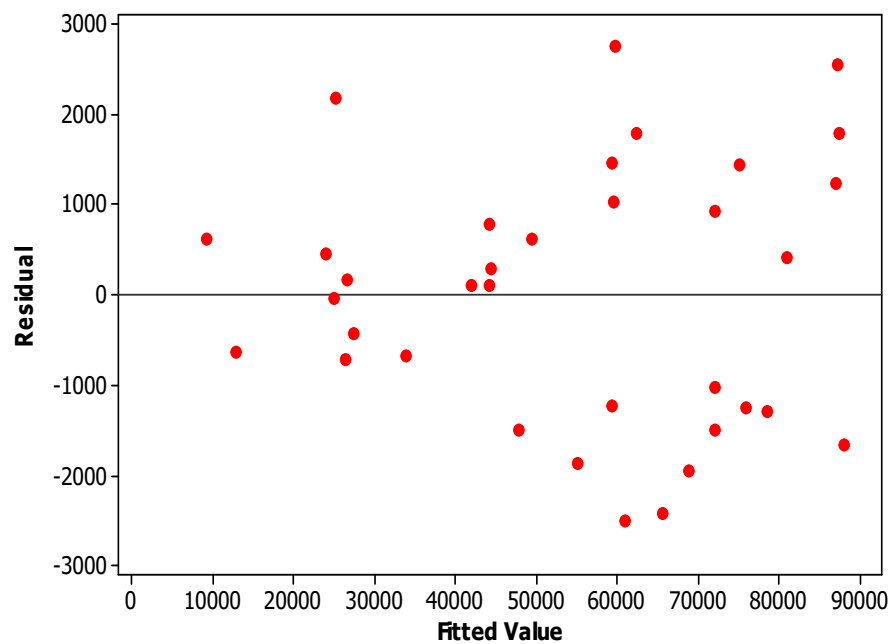


Figure 2.7: Residuals for the calibration data regression analysis showing no clear bias in the coefficient of determination (R^2)

magnitude produce a sample stress of approximately 6.9 ksi (48 MPa) and allow the bearings and other rotating components to warm-up and reach a steady state operating temperature. The load is then applied with the use of a hydraulic ram, and the deflection is locked in place with lock-nut assemblies. Once the deflection is set, the revolution counter is reset. During the initial 5,000 – 20,000 cycles at load there was a run-in period where the sample seated itself, and the machine was periodically stopped to re-tighten the grip assemblies.

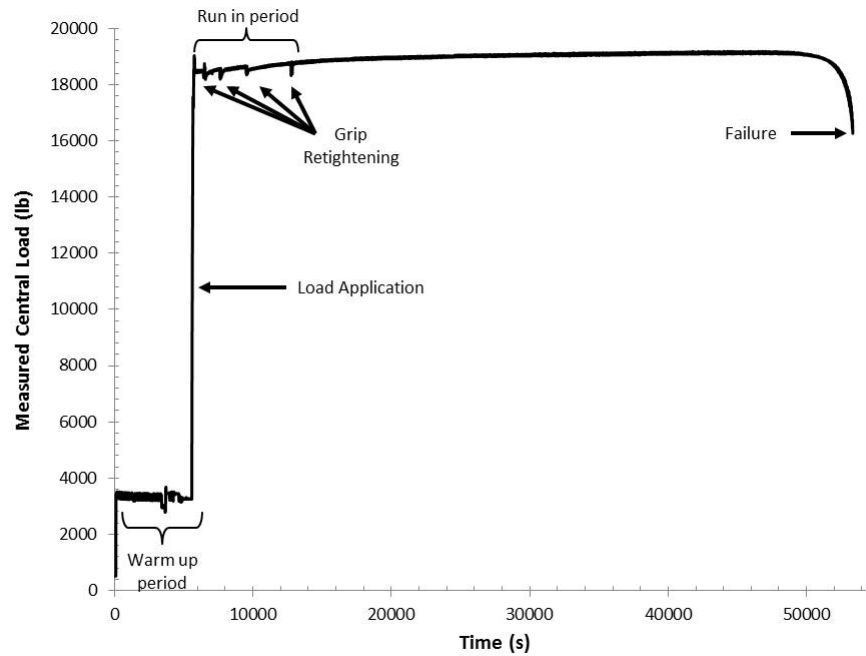


Figure 2.8: Measured central load (lb) plotted versus time for the entire F block control specimen test run at 5 Hz

2.3 Results

Failure of the samples was defined to be the point at which the measured live load decreased to 80% of the initial applied load. This definition captured initiation and

propagation of cracks and prevented total failure, which would mask the features of crack initiation and propagation. The load decrease is associated with crack growth due to the test apparatus operating at a set deflection; as a crack propagates the section thickness is reduced and less load is required to maintain the deflection. The initial running stress for each specimen is given in Table 2.5; the number of cycles to failure for all samples is listed in Table 2.6. The target running stress was 55 ksi (379 MPa). This produces an alternating stress (σ_a) of 55 ksi (379 MPa), a mean stress (σ_m) of 0 ksi (0 MPa), and a stress range (σ_r) of 110 ksi (758 MPa). No data is reported for E-NO due to installation issues during testing that led to an unstable running load and variable stresses.

Table 2.5: Actual stress initially applied during testing. Target stress was 55 ksi (379MPa)

| Block | CO | | NO | | 30 | | 60 | |
|----------|--------------|--------------|--------------|--------------|--------------|--------------|--------------|--------------|
| | Stress (ksi) | Stress (MPa) |
| A | 55.92 | 386 | 54.79 | 378 | 55.89 | 385 | 56.67 | 391 |
| B | 54.92 | 379 | 57.96 | 400 | 56.41 | 389 | 54.59 | 376 |
| C | 55.26 | 381 | 54.30 | 374 | 55.30 | 381 | 55.08 | 380 |
| D | 53.90 | 372 | 56.44 | 389 | 51.90 | 358 | 56.31 | 388 |
| E | 55.39 | 382 | - | - | 54.85 | 378 | 54.44 | 375 |
| F | 56.11 | 387 | 57.20 | 394 | 57.87 | 399 | 56.14 | 387 |
| Average | 55.25 | 381 | 56.14 | 387 | 55.37 | 382 | 55.54 | 383 |
| Std. Dev | 0.8 | 5 | 1.6 | 11 | 2 | 14 | 1 | 7 |

2.4 Statistical Analysis

The fatigue results were analyzed using Kaplan-Meier survival analysis. Kaplan-Meier analysis is a non-parametric statistical technique that is used estimate the probability of time-to-event occurrences of a population based upon a sample population [16]. In this case, the effect of each treatment on the fatigue life, or time to fatigue failure of 4140, is estimated from the samples analyzed in this investigation. The cumulative incidence

Table 2.6: Fatigue life of samples tested

| Block | Treatment Condition | | | |
|---------|--------------------------------|--------------------------------|--------------------------------|--------------------------------|
| | CO (10 ⁴ Cycles) | NO (10 ⁴ Cycles) | 30 (10 ⁴ Cycles) | 60 (10 ⁴ Cycles) |
| A | 25.92 | 20.57 | 15.75 | 22.21 |
| B | 14.07 | 20.86 | 52.29 | 49.80 |
| C | 42.88 | 10.36 | 61.47 | 19.55 |
| D | 28.00 | 30.66 | 25.28 | 50.33 |
| E | 18.38 | - | 72.58 | 15.45 |
| F | 23.56 | 14.05 | 27.45 | 50.10 |
| Average | 25.47 | 19.30 | 42.47 | 34.57 |

of fracture between treatment groups was compared through the log-rank test. Both the Kaplan-Meier survival analysis and the log rank testing were performed using IBM SPSS software.

The Kaplan-Meier survival plots for each treatment condition and the log-rank test result (p value) are given in Figure 2.9. For each treatment condition plot shown, the length of the horizontal portions of the curve represents the survival duration for that interval [16], which in this case is the number of cycles between failures. The vertical distance between the horizontal portions represents the cumulative probability of the event, which in this case represents the probability that failure has not occurred. The discrete points represent occurrences of the monitored event, i.e. failures of the fatigue specimens used in the investigation.

Survival analysis of the test data indicates that in the context of fatigue performance, laser cladding with a preheat is better than the control condition with 95% certainty. At 400,000 cycles there is a 50% probability that 4140 laser clad with the use of a 300°F or 600°F preheat has not failed. In comparison, the probability unclad 4140 has not failed at 400,000 cycles is approximately 18%. There is 0% probability that 4140 clad with no preheat has not failed by 400,000 cycles. Similarly, the number of cycles required to

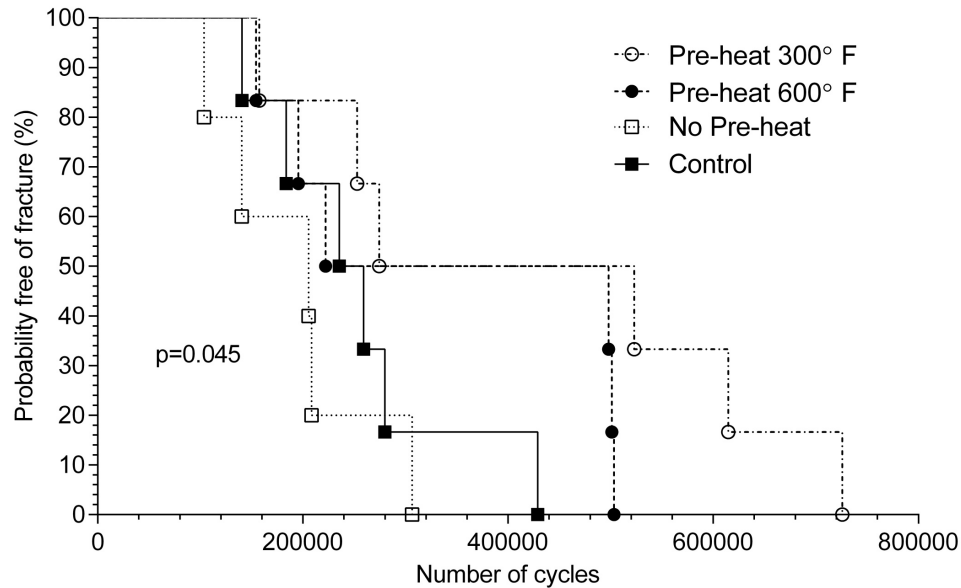


Figure 2.9: Kaplan-Meier Survival plot for the four treatment conditions. Comparison of cumulative incidence of fracture between groups using the log rank test yielded $p=0.045$

produce 100% probability of failure is approximately 720,000 cycles and 505,000 cycles for the 300°F preheat and 600°F preheat treatment conditions respectively, but only 430,000 cycles and 310,000 cycles for the control and no preheat treatment conditions respectively. Comparison of the survival curves using the log-rank test produced a p value of 0.045, showing that the observed differences in the survival curves of the various treatments are statistically significant at the 95.5% confidence interval.

2.5 Discussion

Comparative fatigue test data is generally analyzed through analysis of variance (ANOVA) [14]. ANOVA is a statistical technique through which the variance of the mean between groups is compared to the variation within each group. In essence, ANOVA is a statistical test of whether or not the means of several groups are equal, and relies on the principle assumption that the data is independent and normally distributed. Given the size of the

specimens utilized in this experiment, it was not feasible to have a large enough sample size to ensure that the conditions of ANOVA, i.e. normality of the data, were met. Additionally, the loss of the E-NO sample data resulted in an incomplete data set and necessitated a non-parametric statistical test [17].

Potential sources of error in this study include uncertainties in the running stress for each sample, and potential inhomogeneities between the samples that may have been introduced during the fabrication and testing process. Regression analysis of the calibration data produced a coefficient of determination (R^2) value of 99.6%; indicating that the differences between the measured sample stress (via strain) and the model's predicted stress values are very small. Further analysis of the regression residual plots shows that the data is unbiased. Given the strength of the calibration data, the minor deviations observed in the running stresses of 0.8 ksi – 1.6 ksi (5 MPa – 14 MPa) are not indicative of substantial machine drift or bias in the running loads/stresses.

The potential for error due to inhomogeneities between samples was addressed through the randomization and blocking techniques used as part of the RCB experimental format. Blocking was used to account for both potential and proven nuisance variables by separating experimental units and test conditions into subsets that were more homogeneous than the aggregate, thereby allowing for statistical separation of the nuisance effects from the treatment effects [14]. The use mechanical randomization techniques throughout the experiment ensured the validity of the statistical analysis by providing a random sample.

2.6 Conclusions

Full scale rotating bending fatigue testing was performed on samples of 2.750 inch (69.85 mm) diameter. The material system tested was laser applied 13Cr overlays on a wrought AISI-SAE 4140H substrate. the process and materials tested are representative of refur-

bished industrial components commonly used in the mining and upstream oil and gas sectors. Three levels of preheat were considered in comparison to a control condition: no preheat, 300°F (149°C), and 600°F (316°C) preheats. An innovative application of Kaplan-Meier survival analysis was used to process the fatigue test data. It was found that with 300°F (149°C), and 600°F (316°C) preheats the fatigue life of refurbished components was increased. 100% probability of failure occurred with the 300°F and 600°F preheat treatments at approximately 720,000 and 505,000 cycles respectively. In contrast, 100% probability of failure of the no preheat and control treatment conditions occurred at 310,000 and 430,000 cycles respectively. Comparison of the survival curves of the various treatment conditions using the log-rank test showed that the observed differences in fatigue lives were statistically significant at the 95.5% confidence interval.

2.7 Acknowledgements

The authors would like to acknowledge Apollo-Clad, a Division of Apollo Machine & Welding for their generous support of this project, and to thank Andre Lahote and John Liddiard, for their expertise and logistical support during fabrication and testing.

Chapter 3

Characterization of the Increased Fatigue Life of Alloy Steel Components Following Laser Additive Manufacturing Refurbishment

3.1 Introduction

Laser additive manufacturing, whether for fabrication or repair of industrial components, is a rapidly growing industry world wide. The growth of laser additive manufacturing, often referred to in industry as laser cladding, is driven by its process characteristics. Laser cladding is typified by low heat input, minimal dilution or intermixing with the substrate, a small heat affected zone (HAZ), and fine grained overlay microstructure [1]. However, the widespread application of laser additive manufacturing in industry is hampered by a lack of understanding and reliable data on the fatigue behaviour of repaired components. As a result, many industrial components that are repaired through laser cladding do not include the refurbished layer in the remaining life calculations. This overly conservative approach can lead to increased scrap rate and increased process downtime.

In previous work carried out by Bell et al. [18], full-scale four-point rotating bending fatigue testing was carried out on specimens 2.75 inch (69.85 mm) in diameter. The samples comprise AISI-SAE 4140H steel that had been laser overlaid with 13Cr steel using three different levels of preheat: no preheat, 300°F (149°C), and 600°F (316°C) preheats. The effect of laser processing was evaluated relative to a control condition of unprocessed 4140H material. It was demonstrated that laser processing with a 300°F preheat or a 600°F preheat produces a statistically significant increase in fatigue life relative to unprocessed 4140H samples or samples that had been processed without the use of a preheat. In this paper, the fatigue results of Ref. [18] will be characterized through fractography, residual stress measurements by the hole drilling method, and through microhardness surveys. Before the work of Ref. [18], no studies had been conducted on the effect of laser additive manufacturing on the fatigue performance of full scale components in a four point rotating bending mode [18]. Previous studies had been conducted using smaller scale samples in various fatigue modes. The alternate studies, in combination with generalized fatigue experimentation, demonstrate strong correlations between fatigue performance and two principal factors: the residual stress state induced during laser processing [6, 7, 10, 12, 19–21], and the strength of the material system. [5, 22–24].

Fatigue life is increased in the presence of compressive residual stresses. The magnitude and nature of the residual stresses that are produced during laser processing are governed by the laser parameters and by the temperature dependant responses of the materials themselves. [19]. Tensile residual stresses are developed by the bulk substrate restricting the thermal contraction of the overlay during solidification and cooling. This tensile residual stress can be exacerbated, or mitigated, by volume changes associated with solid-state transformations that occur in the overlay, HAZ, or in both regions. The most commonly encountered solid state transformation is the austenite to martensite

transformation, which is accompanied by a significant volumetric expansion. If this expansion is constrained, large compressive residual stresses can be developed in the transformed region [10,12,19,20,25–28]. In the work completed by Chen et al. [25] the residual stress state produced by cladding several different materials systems was evaluated. In the system with no solid state transformation materials (alloy 625/alloy 625), large tensile residual stresses were produced in the overlay due to differential thermal expansion. In a materials system in which a non-solid state transformable overlay was applied to a transformable substrate (stellite 6/AISI 1075 steel) compressive residual stresses were developed in the HAZ, and large tensile stresses were developed in the overlay. In the work completed by Da Sun [7], overlaying a solid-state transformable steel with another solid state transformable steel (AerMet 100/AISI 4340) produced large compressive residual stresses in both the overlay and HAZ.

The strength of the material affects the mechanism of failure. The fatigue limit for a given material is not the threshold for crack nucleation, but rather the threshold stress for the propagation of microcracks that were developed under cyclic stresses [24]. For lower strength steels below approximately 400 HV, the microcracks are generally developed at microstructural features such as grain boundaries or persistent slip bands [22]. In this case, the fatigue limit is governed primarily by microstructural considerations and it is proportional to the material hardness. [24]. For higher strength materials above approximately 400 HV, the development of microcracks is associated with the presence of inhomogeneities such as precipitates, inclusions and other discontinuities. In this regime, the fatigue limit is dependent on a critical flaw size, and it is no longer proportional to the material hardness. [24]

3.2 Experimental Design

Four spare samples from the investigation of Ref. [18] were used to measure residual stresses, hardness, and to characterize the microstructures. Sample C-SP was used as a control sample, labelled RS-CO in this work. Samples B-SP, A-SP, and F-SP were used for the no preheat condition (RS-NO), 300°F preheat (RS-30), and 600°F preheat (RS-60) conditions respectively.

The chemical composition and mechanical properties of the 4140 substrate as reported on the materials test report (MTR) are given in Tables 3.1 and 3.2. The chemical composition of the overlay material is given in Table 3.3.

Table 3.1: Composition of the 4140 steel used in experiments (wt%)

| C | Mn | P | S | Si | Cr | Ni | Mo | Cu | Al | V |
|------|------|------|-------|-------|------|------|-----|------|-------|-------|
| 0.42 | 0.98 | 0.01 | 0.022 | 0.026 | 0.98 | 0.14 | 0.2 | 0.19 | 0.028 | 0.006 |

Table 3.2: Mechanical properties of the 4140 steel used in experiments as reported on the materials test report (MTR)

| σ_Y Mpa (ksi) | UTS Mpa (ksi) | % Elong | % RA | Hardness(BHN) |
|----------------------|---------------|---------|------|---------------|
| 899 (130.4) | 1,030 (149.4) | 15.4 | 49.6 | 328 |

Table 3.3: 13Cr overlay chemistry (wt. %)

| C | Si | Cr | Fe |
|-----|------|----|-----|
| 0.1 | 0.75 | 12 | Bal |

3.3 Results

3.3.1 Material Characterization

The 4140H control specimen microstructure comprises tempered martensite. The microstructure is heavily banded in the axial, or rolling direction direction. The laser processed samples, shown in Figures 3.1 – 3.3 comprise tempered martensite. All of the laser clad overlay microstructures possessed morphologies consistent with macro-segregation including: beaches, peninsulas, and islands. [29] Delta ferrite was also identified in all overlay microstructures through electrolytic tint etching with ASTM E407 Etchant No. 220 (20% NaOH_{aq} at 20 V-DC for 7 seconds), which reveals martensite and colours delta ferrite yellow. [30] The delta ferrite was present both interdendritically and as large islands. The RS-NO sample was qualitatively observed to have more delta ferrite islands than either the RS-30 or RS-60 samples.

In all of the laser processed metallographic samples, the overlay was metallurgically bonded to the substrate and free from linear defects or discontinuities such lack of fusion, cracking, or oxide stringers. Isolated small scale spherical oxides and/or porosity was observed in all overlays.

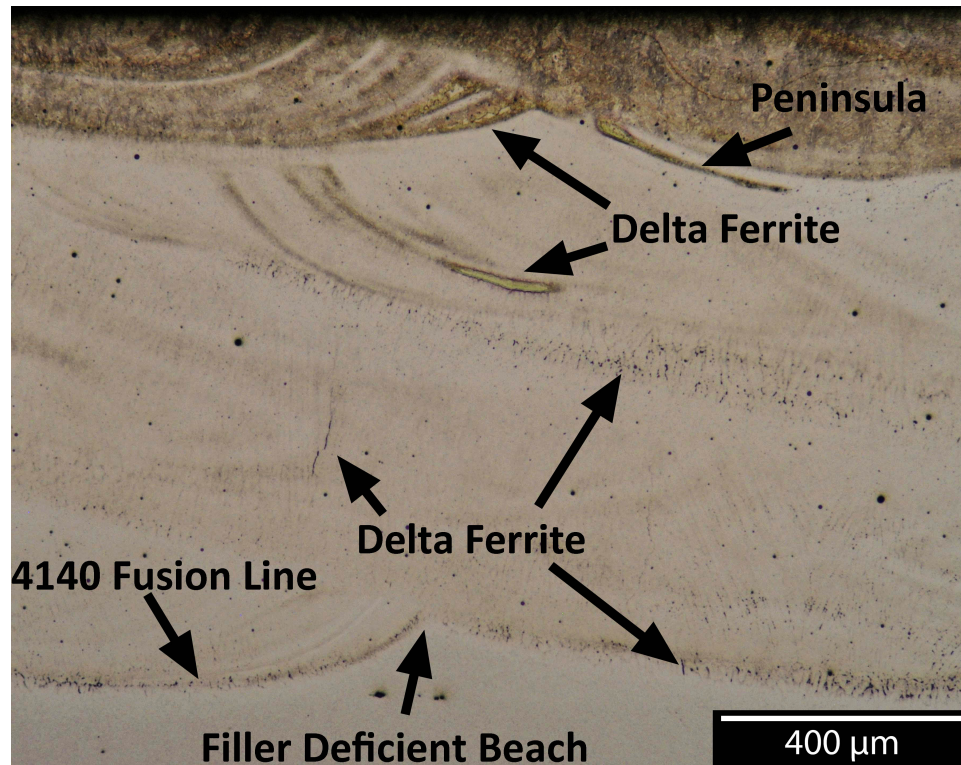


Figure 3.1: 300°F preheat specimen (RS-30) Overview of the overlay layer including the interpass and 4140H substrate fusion lines. Etched with ASTM E407 Etchant No. 220.

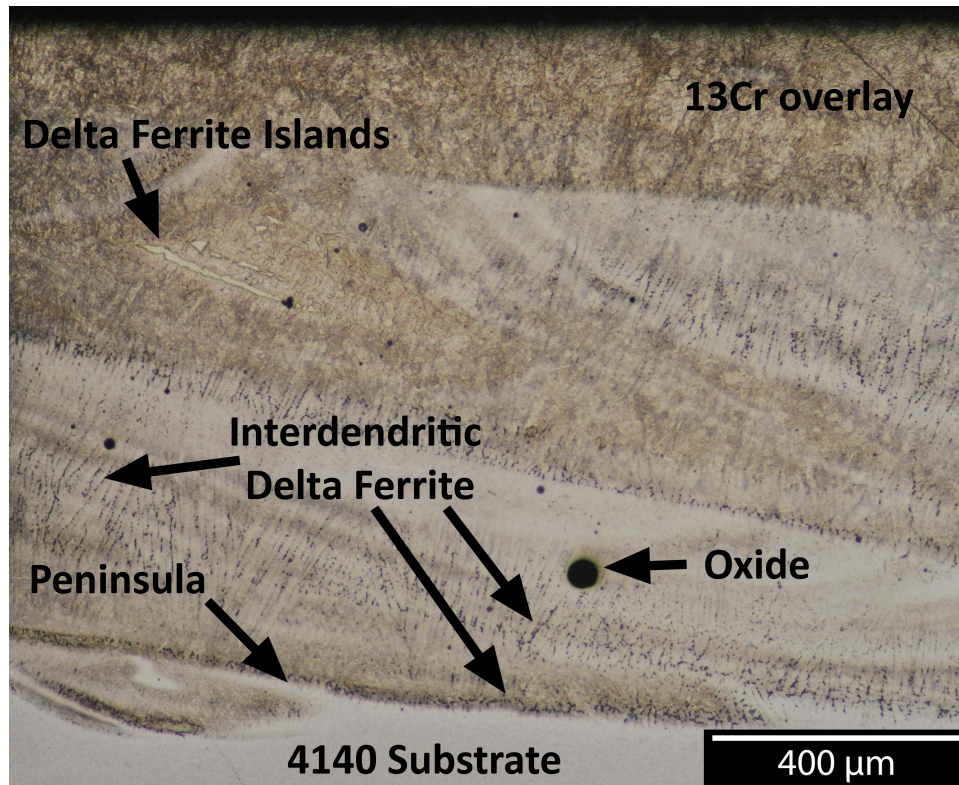


Figure 3.2: 600°F preheat specimen (RS-60) Overview of the overlay layer including the interpass and 4140H substrate fusion lines. Etched with ASTM E407 Etchant No. 220.

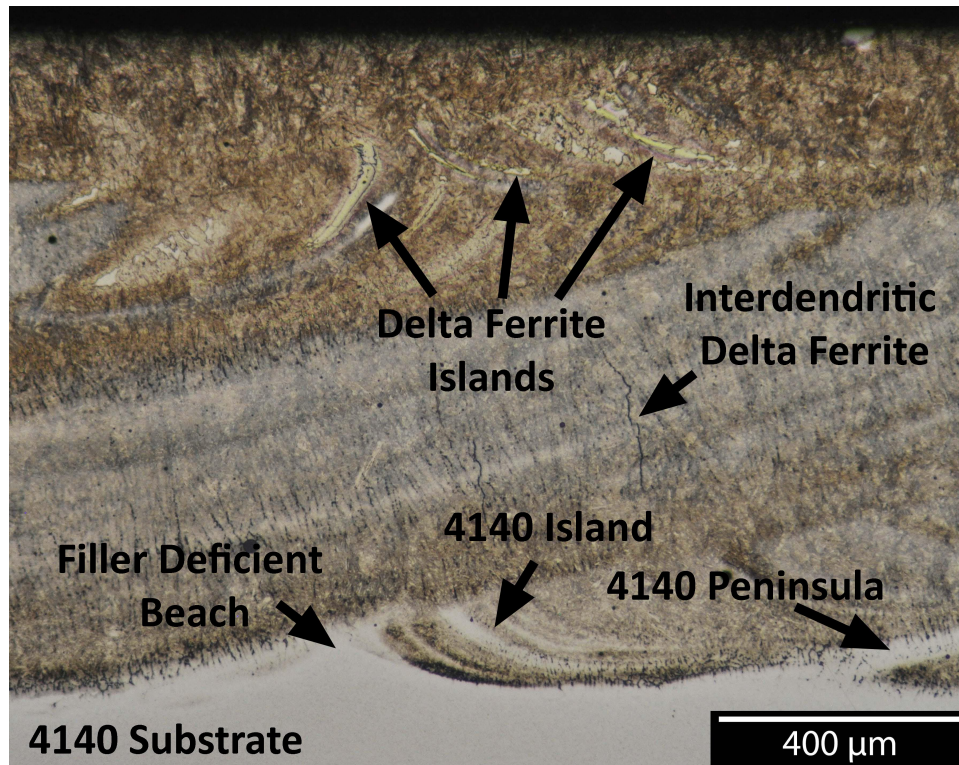


Figure 3.3: No preheat specimen (RS-NO) Overview of the overlay layer including the inter-pass and 4140H substrate fusion lines. Etched with ASTM E407 Etchant No. 220.

3.3.2 Fractography

In the work completed by Ref. [18], failure of the 23 fatigue samples tested was defined to be the point at which the measured live load decreased to 80% of the initial applied load. This definition captured initiation and propagation of cracks and prevented total failure, which would mask the fracture features associated with initiation and propagation. The partial fatigue fractures were opened for analysis by cooling the specimens to liquid nitrogen temperatures and subjecting them to overload in a 3-pt bending mode. The fracture surfaces were subsequently characterized through optical and scanning electron fractography.

Analysis of the specimen fracture surfaces showed that fatigue failure preferentially

initiated at different locations depending on the sample condition. Control specimens were found to exclusively initiate failure at the sample surface. In some cases failure was initiated by a non metallic inclusion in the near surface region (Figure 3.4), in other instances there was no obvious stress raiser associated with initiation (Figure 3.5). Four of five specimens that had been laser processed without the use of a preheat were found to preferentially initiate failure at fusion line discontinuities as shown in Figure 3.6. Scanning electron microscopy (SEM) and electron dispersive spectroscopic (EDS) analysis of the discontinuities determined that they were entrapped silicon oxides associated with the overlay process. The one specimen that did not initiate failure at a fusion line discontinuity had fracture initiate at a HAZ inclusion.

The 300°F preheat specimens were found to preferentially initiate failure at non-metallic inclusions located in the substrate HAZ. Four of the six 300°F preheat specimens failed at HAZ inclusions, the remaining specimens failed at a fusion line inclusions.

The 600°F preheat specimens did not show a clear preference in the location of failure initiation. Two of the six 600°F preheat specimens tested failed at fusion line discontinuities; other locations of failure included: non-metallic inclusion in the HAZ (1 sample), entrapped oxide in the overlay layer (1 sample), surface initiation (1 sample), and gas porosity in the overlay (1 sample).

A representative optical view of a subsurface inclusion initiated fracture is shown in Figure 3.7 for the Block B 300°F preheat specimen. EDS analysis of the inclusion in Figure 3.8 showed that it was a mixed calcium and aluminium oxide with a calcium sulphide/Manganese sulphide shell. Inclusions of this type are commonly produced during steel making and processing operations. [22].

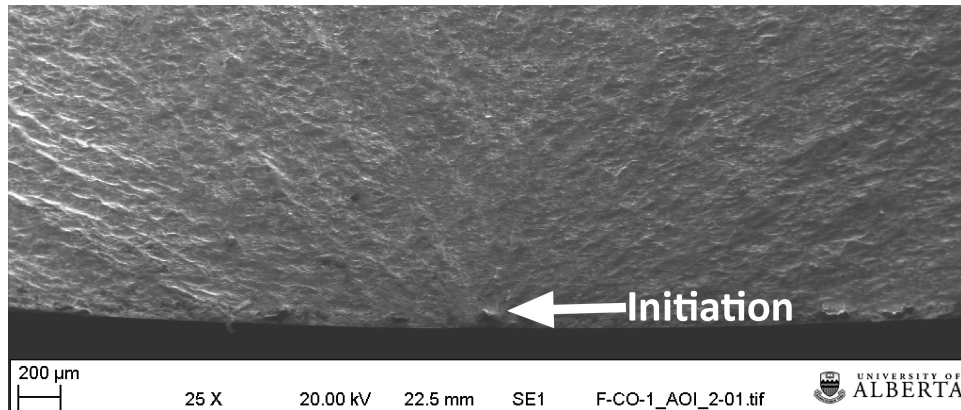


Figure 3.4: Block F control specimen (F-CO) fatigue initiation at a non-metallic inclusion

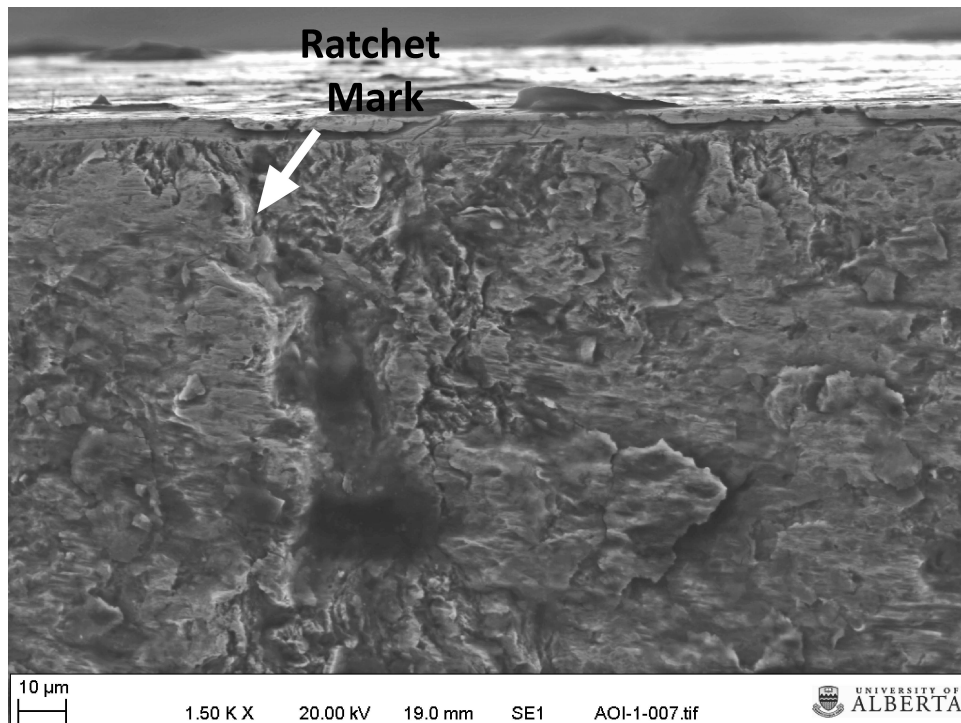


Figure 3.5: Block B control specimen (B-CO) fatigue initiation at the surface as indicated by the presence of a radially orientated ratchet mark.

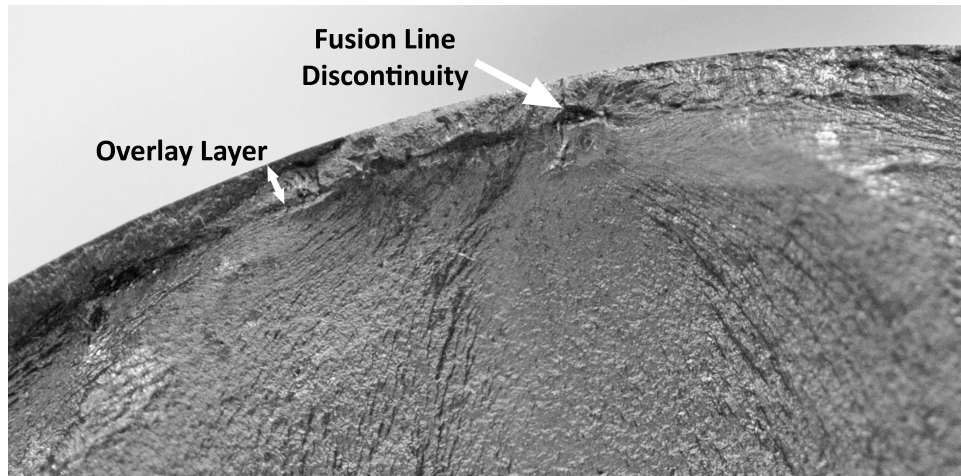


Figure 3.6: Fatigue failure initiation location on the no preheat specimen of Block A (A-NO)

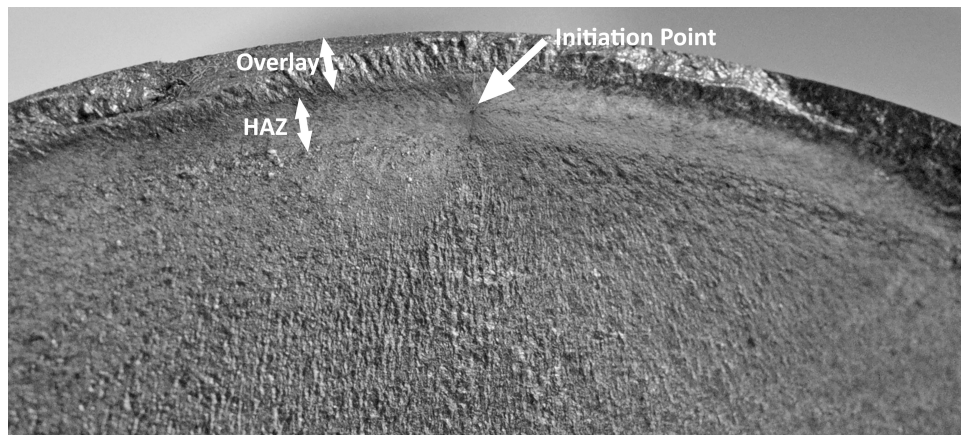


Figure 3.7: 300°F preheat specimen of Block B (B-30) subsurface fatigue fracture initiation in the substrate material HAZ

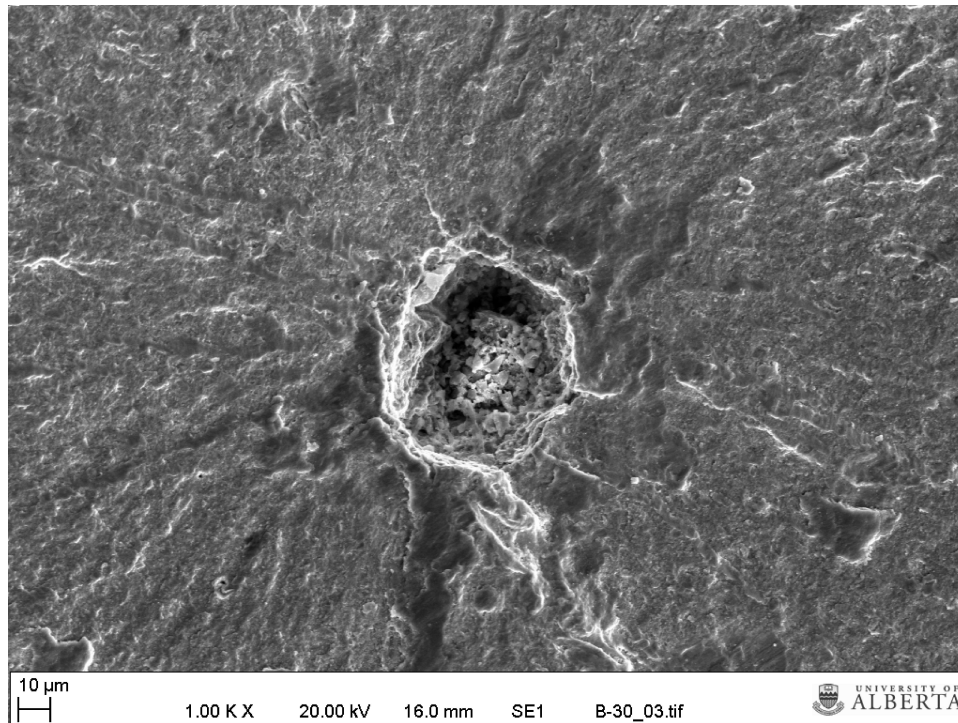


Figure 3.8: 300°F preheat specimen of Block B (B-30) failure initiated at a non-metallic inclusion typical of steel making.

3.3.3 Residual Stress

Residual stress measurements were carried out on each sample condition using the hole drilling method outlined in ASTM E837-08 [31]. Type A strain gauge rosettes of 1/16 inch size were installed on the specimen reduced sections. The residual stresses were calculated from the resulting strain data using the non-uniform stress computational method for a “thick” work piece and a modulus of 30×10^6 psi (210 GPa) [15]. The computed Cartesian stresses are plotted relative to the depth below the sample surface in Figures 3.9 – 3.12. One of the Cartesian components is in the axial direction of the specimen, and the orthogonal component is in the circumferential direction of the specimen. The axial stress is orientated in the longitudinal direction (the direction of bending stress), and the circumferential stress acts in the hoop stress direction (perpendicular to the axial

stress). For all laser clad samples, the substrate fusion line was located approximately 0.040 inch (1 mm) below the sample surface.

For each preheat level, the laser processed samples had measured compressive residual stresses that significantly exceeded 60% of the 4140 substrate material yield stress (90 ksi/539 MPa). At measured stresses greater than 60%; it is likely that localized yielding of the material has occurred in the vicinity of the drilled hole. [31, 32]; in this case, the measured stresses can only be reported as indicative of large compressive residual stresses [31].

The control specimen was found to have maximum calculated compressive residual stress of approximately 32 ksi (221 MPa). The location of maximum stress coincided with the surface of the sample, and the stress decayed to near zero over a depth of 0.004 inch – 0.006 inch (0.10 mm – 0.15 mm). Near surface residual stress profiles of this type and magnitude are consistent with stresses induced through machining operations. [10, 33, 34]

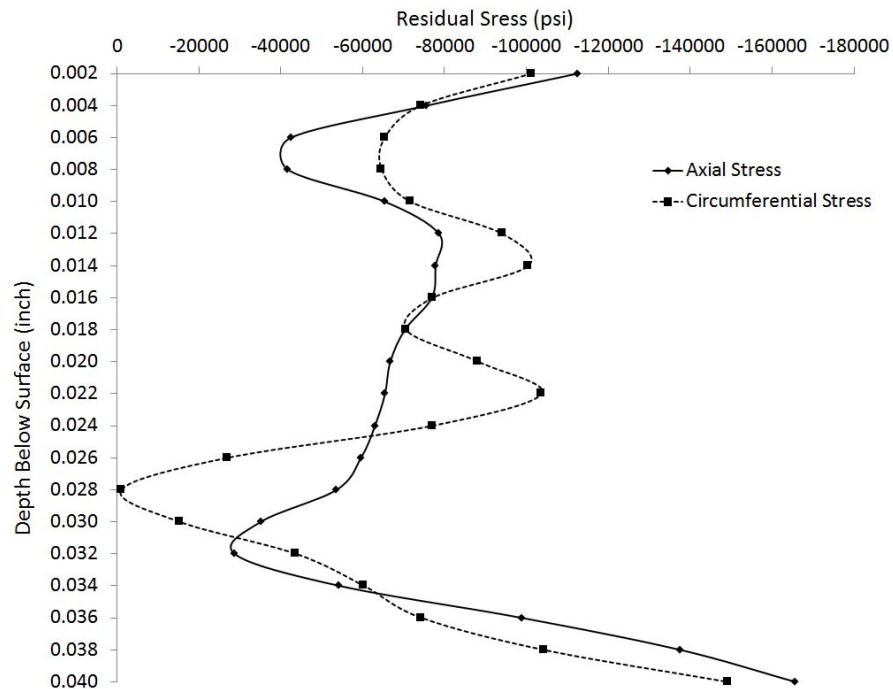


Figure 3.9: 300°F (149°C) Preheat (RS-30) sample residual stress profile

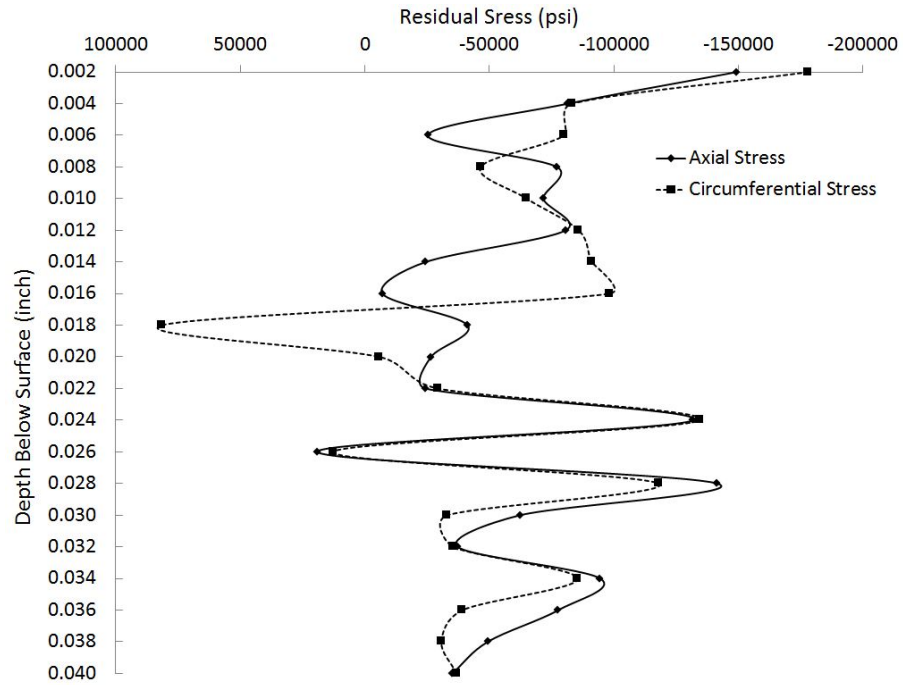


Figure 3.10: 600°F (316°C) Preheat (RS-60) sample residual stress profile

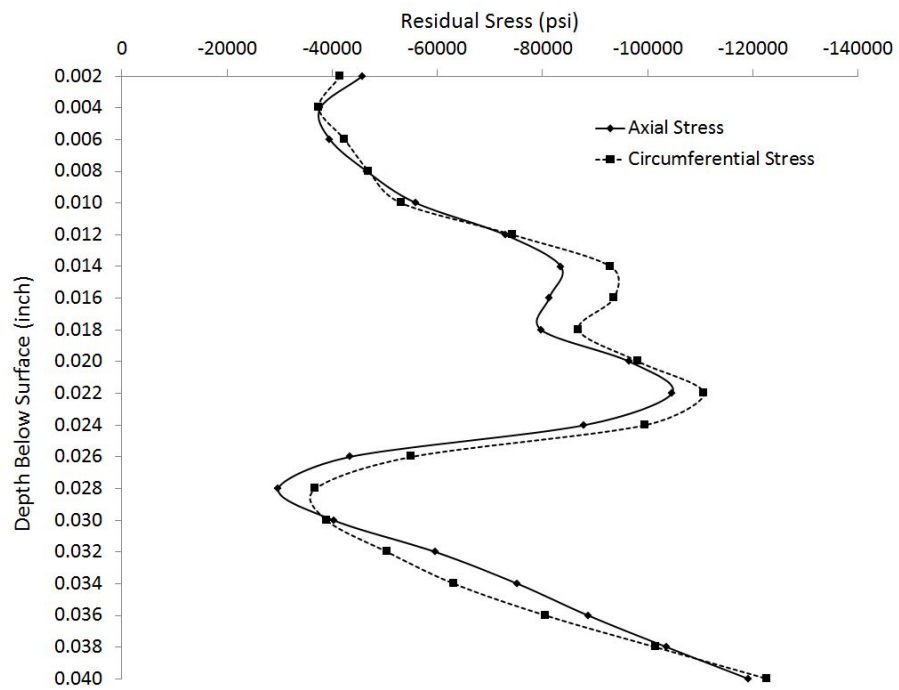


Figure 3.11: No Preheat (RS-NO) sample residual stress profile

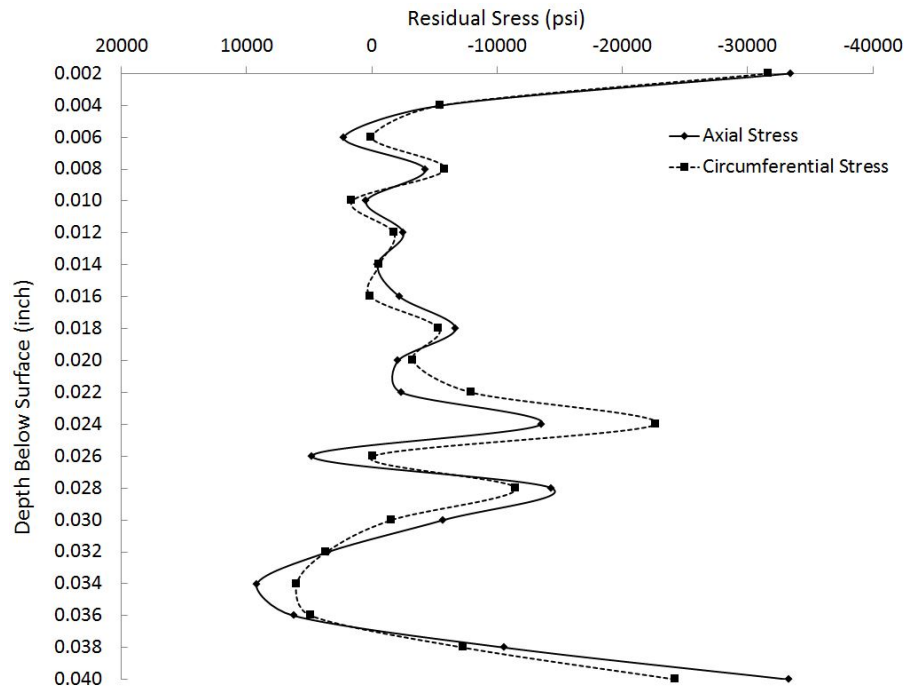


Figure 3.12: 600°F (316°C) Preheat (RS-60) sample residual stress profile

3.3.4 Hardness Mapping

For the laser processed coupons, RS-NO, RS-30, and RS-60, a hardness survey was performed using a 10×15 matrix with 0.2 mm (0.005 inch) indent spacing. For the control specimen hardness survey, a 10×5 matrix with 0.2 mm (0.005 inch) spacing was used. For all laser clad specimens, the fusion line was located approximately 0.040 inch (1 mm) below the sample surface. The average hardness for each sample condition is given as a function of depth in Figure 3.13.

The average hardness of each overlay to a depth of 0.040 inch (1 mm) was determined to be 418 HV, 399 HV, and 430 HV for the no preheat, 300°F (149°C) preheat, and 600°F (316°C) preheat conditions respectively. The average hardness of the substrate adjacent to the no preheat, 300°F preheat, and 600°F preheat overlays was found to be 304 HV, 320 HV, 321 HV respectively. The unclad control specimen had an average hardness of

294 HV.

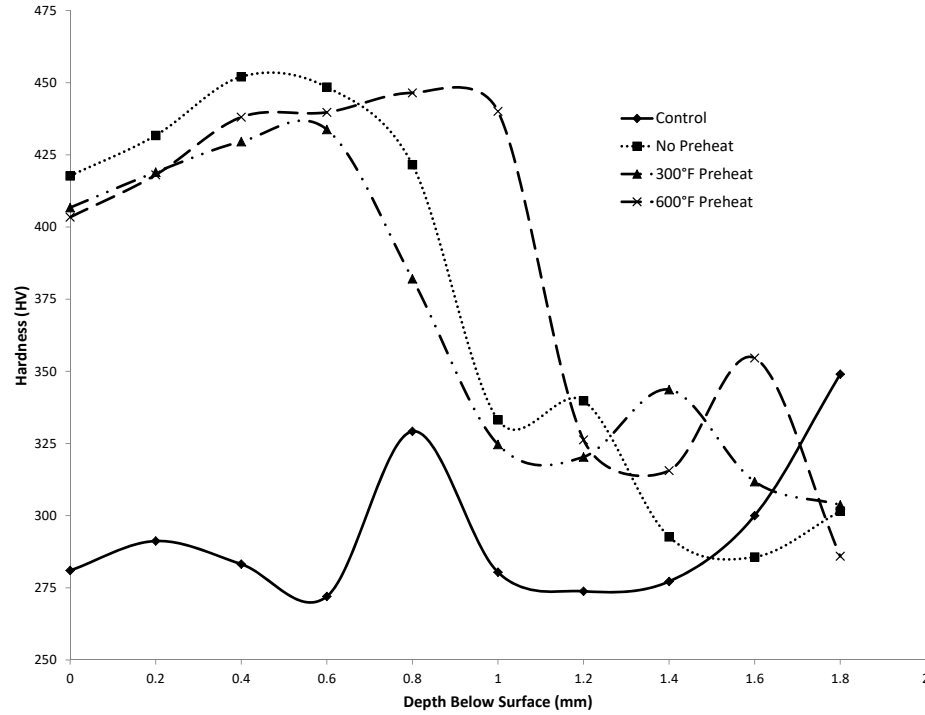


Figure 3.13: Average specimen hardness as a function of depth. For each of the laser processed samples, the fusion line was located ≈ 1 mm (0.040 inch) below the surface

3.4 Discussion

Fractographic analysis showed that all laser clad coupons fell under the flaw dominated fatigue regime. In this regime the fatigue strength is dependant on a critical flaw size, which in turn is governed in part by the hardness of material [24]. In this regime the higher hardness overlay is more tolerate than the substrate material to similarly sized defects. Experimentally, this effect was observed by the location of fatigue initiation. The unprocessed 4140 material preferentially initiated failure at the surface. In contrast, samples that had been laser processed with 300°F preheats preferentially initiated failure at non-metallic inclusions located in the substrate HAZ, despite the presence of simi-

larly sized oxides in the overlay layer. The poor fatigue life of samples that had been laser processed without a preheat is attributable to the higher probability of cladding discontinuities; four of five samples were observed to nucleate failure at large fusion line inclusions. It is likely that the higher occurrence of fusion line discontinuities is related to the bead geometry produced by laser processing without a preheat. Laser cladding onto a cooler substrate would produce a tall, narrow, clad bead [35]. In subsequent, overlapping, laser tracks, bead geometries of this type would increase the probability of fusion line defects such as entrapped oxides and porosity.

Residual stress measurements showed that the laser processed coupons had large compressive residual stresses. Based upon the material system it is expected that large compressive residual stresses would be developed in the overlay and portions of the heat affected zone (HAZ) as both the overlay and substrate material are capable of undergoing solid-state transformations from austenite to martensite during rapid cooling from cladding temperatures to ambient temperature. The variability in the residual stress over the measured depth of the laser processed samples is consistent with localized yielding of the material [31, 32], and back-tempering between successive laser passes and overlay layers. The generation of the compressive residual stress is a function of the constrained volumetric expansion that accompanies martensite transformation. Tempering the constrained martensite results in precipitation of carbides and a reduction in total volume, which serves to reduce the local stress state in the transformed and tempered regions [19].

Hardness surveys of the laser processed samples showed that they had similar average hardness values in the overlay region. In all cases, it was observed that the hardness of the overlay increased from the specimen surface towards the fusion line, located approximately 1 mm (0.040 inch) below the surface. The increase in hardness is indicative of back-tempering between the first and second overlay layers. The large amount of variability in the hardness of both the control specimen and the substrate regions of the laser

clad samples is consistent with the banded microstructure of the 4140 material.

3.5 Conclusions

Full scale rotating bending fatigue testing was performed on wrought AISI-SAE 4140H samples with laser applied martensitic stainless steel overlays with three different preheat levels. The samples, which were 2.750 inch (69.85 mm) diameter, were tested in a 4-pt rotating bending fatigue mode on a custom built apparatus. The impact of laser cladding operations on the fatigue life of the samples was characterized through fractography, hardness surveys, and residual stress measurements by the hole drilling method.

All sample microstructures comprise tempered martensite. The pre-clad 4140 substrate comprises tempered martensite heavily banded in the axial (rolling) direction. The overlay microstructure of at all preheat levels showed morphologies consistent with macro-segregation.

Fractographic analysis indicated that the location of fatigue initiation was strongly influenced by the processing conditions. 100% of the control specimens initiated the fracture at the sample surface. 80% of the specimens clad without preheat were found to initiate failure at fusion line discontinuities between the overlay and 4140 substrate. 67% of the 300°F preheat samples initiated failure at non-metallic inclusions located in the substrate heat affected zone (HAZ). No clear preference was observed in the failure initiation location of the 600°F preheat samples.

Residual stress analysis indicated that laser processing produced large compressive residual stress states, regardless of the level of preheat used. The measured stresses exceeded 60% of the substrate material yield stress. At these high measured stresses the applicable standard [31] indicates that the measures are "indicative only" because of the likelihood of plastic deformation during the hole drilling operation. The control

condition, which saw no thermal cycling, showed a maximum compressive residual stress of ≈ 32 ksi (221 MPa) at the sample surface. The stress was observed to decay to near zero over a depth of 0.004 – 0.006 inch (0.10 mm – 0.15 mm). Residual stresses of this magnitude are consistent with residual stresses induced during machining operations.

The laser processed samples had similar average hardness values in the overlay region. For all preheat levels, the hardness of the overlay was found to be significantly higher than that of the 4140 substrate. The average hardness of the laser processed samples in the overlay region was 418 HV, 399 HV, and 430 HV for the no preheat, 300°F (149°C) preheat, and 600°F (316°C) preheat conditions respectively. The average hardness of the substrate adjacent to the no preheat, 300°F preheat, and 600°F preheat overlays was found to be 304 HV, 320 HV, 321 HV respectively. The unclad control specimen had an average measured hardness of 294 HV.

The large compressive residual stress state produced in this materials system, in conjunction with higher measured hardness of the overlay, accounts for the increase in fatigue life following laser processing with an appropriate preheat. The induced compressive residual stresses offset the tensile stress applied during testing and creates a lower effective stress in the near surface region. Similarly, the higher measured hardness of the overlay relative to the 4140 substrate indicates a microstructure that has both a higher fatigue strength, and that is more resistant to the presence of discontinuities than the base material. These effects were observed experimentally in the location of fatigue failure initiation.

3.6 Acknowledgements

The authors would like to acknowledge Apollo-Clad, a Division of Apollo Machine & Welding for their generous support, and to thank the members of the Canadian Center

for Welding and Joining for their support and help throughout the project.

Chapter 4

Conclusions and Future Work

4.1 Conclusion and Summary of Findings

Full scale rotating bending fatigue testing was performed on samples of 2.750 inch (69.85 mm) diameter. The material system tested was laser applied 13Cr overlays on a wrought AISI-SAE 4140H substrate. The process and materials tested are representative of refurbished industrial components commonly used in the mining and upstream oil and gas sectors. Three levels of preheat were considered in comparison to a control condition: no preheat, 300°F (149°C), and 600°F (316°C) preheats. An innovative application of Kaplan-Meier survival analysis was used to process the fatigue test data. It was found that with 300°F (149°C), and 600°F (316°C) preheats the fatigue life of refurbished components was increased. 100% probability of failure occurred with the 300°F and 600°F preheat treatments at approximately 720,000 and 505,000 cycles respectively. In contrast, 100% probability of failure of the no preheat and control treatment conditions occurred at 310,000 and 430,000 cycles respectively. Comparison of the survival curves of the various treatment conditions using the log-rank test showed that the observed differences in fatigue lives were statistically significant at the 95.5% confidence interval.

Fractographic analysis indicated that the location of fatigue initiation was strongly influenced by the processing conditions. 100% of the control specimens initiated the

fracture at the sample surface. 80% of the specimens clad without preheat were found to initiate failure at fusion line discontinuities between the overlay and 4140 substrate. 67% of the 300°F preheat samples initiated failure at non-metallic inclusions located in the substrate heat affected zone (HAZ). No clear preference was observed in the failure initiation location of the 600°F preheat samples.

Residual stress analysis indicated that laser processing produced large compressive residual stress states, regardless of the level of preheat used. The measured stresses exceeded 60% of the substrate material yield stress. At these high measured stresses the applicable standard [31] indicates that the measures are "indicative only" because of the likelihood of plastic deformation during the hole drilling operation. The control condition, which saw no thermal cycling, showed a maximum compressive residual stress of ≈ 32 ksi (221 MPa) at the sample surface. The stress was observed to decay to near zero over a depth of 0.004 – 0.006 inch (0.10 mm – 0.15 mm). Residual stresses of this magnitude are consistent with residual stresses induced during machining operations.

The laser processed samples had similar average hardness values in the overlay region. For all preheat levels, the hardness of the overlay was found to be significantly higher than that of the 4140 substrate. The average hardness of the laser processed samples in the overlay region was 418 HV, 399 HV, and 430 HV for the no preheat, 300°F (149°C) preheat, and 600°F (316°C) preheat conditions respectively. The average hardness of the substrate adjacent to the no preheat, 300°F preheat, and 600°F preheat overlays was found to be 304 HV, 320 HV, 321 HV respectively. The unclad control specimen had an average measured hardness of 294 HV.

The large compressive residual stress state produced in this materials system, in conjunction with higher measured hardness of the overlay, accounts for the increase in fatigue life following laser processing with an appropriate preheat. The induced compressive residual stresses offset the tensile stress applied during testing and creates a

lower effective stress in the near surface region. Similarly, the higher measured hardness of the overlay relative to the 4140 substrate indicates a microstructure that has both a higher fatigue strength, and that is more resistant to the presence of discontinuities than the base material. These effects were observed experimentally in the location of fatigue failure initiation.

4.2 Recommended Future Work

This study represents the first investigation into the effects of laser cladding on the fatigue performance of full scale components. This is also the first instance in which laser cladding was measured to produce increased fatigue performance. It is recommended that future studies be undertaken to model the cladding process. Potential objectives of the model could include:

- Determination of the effect of overlay geometry and thickness on the residual stress state.
- Determination of the effect of changing substrate geometries and thickness on the development of residual stresses.
- Determination of the microstructural evolution and potential mechanisms for the observed macro-segregation.

Bibliography

- [1] Patricio F. Mendez, Nairn Barnes, Kurtis Bell, Steven D. Borle, Satya S. Gajapathi, Stuart D. Guest, Hossein Izadi, Ata Kamyabi Gol, and Gentry Wood. Welding processes for wear resistant overlays. *Journal of Manufacturing Processes*, 16(1):4–25, 2014.
- [2] V.M. Weerasinghe and W.M. Steen. Laser Cladding with Blown Powder. *Metal Construction*, pages 581–585, 1987.
- [3] George E. Dieter. *Mechanical Metallurgy*. McGraw-Hill, Boston, 3rd edition, 1986.
- [4] ISO-1143:2010(E). Metallic materials - Rotating bar bending fatigue testing. 2010.
- [5] M. M. Alam, A. F H Kaplan, J. Tuominen, P. Vuoristo, J. Miettinen, J. Poutala, J. Näkki, J. Junkala, T. Peltola, and Z. Barsoum. Analysis of the stress raising action of flaws in laser clad deposits. *Materials and Design*, 46:328–337, 2013.
- [6] H. Köhler, R. Rajput, P. Khazan, and J. Rebelo Kornmeier. On the influence of laser cladding and post-processing strategies on residual stresses in steel specimens. *Physics Procedia*, 56(C):250–261, 2014.
- [7] Shi Da Sun, Qianchu Liu, Milan Brandt, Vladimir Luzin, Ryan Cottam, Madabhushi Janardhana, and Graham Clark. Effect of laser clad repair on the fatigue behaviour

of ultra-high strength AISI 4340 steel. *Materials Science and Engineering A*, 606:46–57, 2014.

- [8] Henry Koehler, Knut Partes, Thomas Seefeld, and Frank Vollertsen. Influence of laser reconditioning on fatigue properties of crankshafts. *Physics Procedia*, 12(PART 1):512–518, 2011.
- [9] Eric Whitney, Keith Egland, and Kenneth Jr. Meinert. Fatigue Response of AISI 4140 Laser Clad with 410SS, 420SS, and Nickel-Aluminum Bronze. In *Section D-ICALEO*, pages 85–94, 2000.
- [10] J. Tuominen, J. Näkki, J. Poutala, J. Miettinen, T. Peltola, P. Vuoristo, I. Rasehorn, M. M. Alam, and a. F. H. Kaplan. Fatigue behavior of laser clad round steel bars. *Journal of Laser Applications*, 27(1):012006, 2015.
- [11] S.S. Manson and G.R. Halford. *Fatigue and Durability of Structural Materials*. ASM International, Metals Park, 2006.
- [12] Novana Hutasoit, Vladimir Luzin, Aaron Blicblau, Wenyi Yan, Milan Brandt, and Ryan Cottam. Fatigue life of laser clad hardfacing alloys on AISI 4130 steel under rotary bending fatigue test. *International Journal of Fatigue*, 72:42–52, 2015.
- [13] A.A Wells. British Welding Research Association: New Fatigue Testing Laboratory at Abington, Cambridge. *Nature*, 4316, 1952.
- [14] R.E. Little and E.H. Jebe. *Statistical Design of Fatigue Experiments*. Applied Science Publishers Ltd., London, 1st edition, 1975.
- [15] Michael F. Ashby. *Materials Selection in Mechanical Design*. Elsevier, 3rd edition, 2005.

- [16] Courtney J. Voelker, Phil D. Oxon, Brian Nussenbaum, and Eric W Wang. *Otolaryngol Head Neck Surg.*
- [17] Carles Serrat and Vicenc Gilbert. Survival Analysis Methodology for Service Life Prediction and Building Maintenance. *International Conference on Durability of Building Materials and Components*, pages 1–8, 2011.
- [18] Kurtis P. Bell, Carlos Cervera, Douglas Hamre, Kip O. Findley, and Patricio F. Mendez. Full-Scale Testing of the Fatigue Life of Laser Additive Manufacturing Repaired Alloy Steel Components. Submitted 2017. Unpublished.
- [19] J. Y. Chen, K. Conlon, L. Xue, and R. Rogge. Experimental study of residual stresses in laser clad AISI P20 tool steel on pre-hardened wrought P20 substrate. *Materials Science and Engineering A*, 527(27-28):7265–7273, 2010.
- [20] M. de Freitas, M.S. Pereira, H. Michaud, and D. Pantelis. Analysis of residual stresses induced by laser processing. *Materials Science and Engineering: A*, 167:115–122, 1993.
- [21] L. P. Borrego, J. T B Pires, J. M. Costa, and J. M. Ferreira. Fatigue behaviour of laser repairing welded joints. *Engineering Failure Analysis*, 14(8 SPEC. ISS.):1586–1593, 2007.
- [22] K.O Findley, R.L Cryderman, A.B. Nissan, and D.K. Matlock. *The Effects of Inclusions on Fatigue Performance of Steel Alloys*, 2013.
- [23] M. L. Hayne, P. I. Anderson, K. O. Findley, and C. J. Van Tyne. Effect of microstructural banding on the fatigue behavior of induction-hardened 4140 steel. *Metallurgical and Materials Transactions A: Physical Metallurgy and Materials Science*, 44(8):3428–3433, 2013.

- [24] Yukitaka Murakami. Material defects as the basis of fatigue design. *International Journal of Fatigue*, 41:2–10, 2012.
- [25] Jianyin Chen, Sheng Hui Wang, and Lijue Xue. On the development of microstructures and residual stresses during laser cladding and post-heat treatments. *Journal of Materials Science*, 47(2):779–792, 2012.
- [26] Henry Köhler, Knut Partes, Joana Rebelo Kornmeier, and Frank Vollertsen. Residual Stresses in Steel Specimens Induced by Laser Cladding and their Effect on Fatigue Strength. *Physics Procedia*, 39:354–361, 2012.
- [27] E. Pluyette, J.M. Sprauel, and D. Buisine. Evaluation of residual stresses in pvd-coatings. In *Experimental Mechanics*, pages 205–211, Baltimore, 1994.
- [28] Youxiang Chew, John Hock Lye Pang, Guijun Bi, and Bin Song. Effects of laser cladding on fatigue performance of AISI 4340 steel in the as-clad and machine treated conditions. *Journal of Materials Processing Technology*, 243:246–257, 2017.
- [29] S Kou and Y K Yang. Fusion-boundary Macrosegregation in Dissimilar-Filler Metal Welds. *Welding Journal*, 86(10):303, 2007.
- [30] ASTM E 407:2015. Standard Practice for Microetching Metals and Alloys. pages 1–22, 2015.
- [31] ASTM E 837:2008. Standard Test Method for Determining Residual Stresses by the Hole-Drilling Strain-Gages. 1:1–17, 2008.
- [32] Rahman Seifi and Davood Salimi-Majd. Effects of plasticity on residual stresses measurement by hole drilling method. *Mechanics of Materials*, 53:72–79, 2012.

- [33] Ataollah Javidi, Ulfried Rieger, and Wilfried Eichlseder. The effect of machining on the surface integrity and fatigue life. *International Journal of Fatigue*, 30(10-11):2050–2055, 2008.
- [34] Hiroyuki Sasahara. The effect on fatigue life of residual stress and surface hardness resulting from different cutting conditions of 0.45%C steel. *International Journal of Machine Tools and Manufacture*, 45(2):131–136, 2005.
- [35] G. Wood, S. Islam, and P.F. Mendez. Calibrated expressions for welding and their application to isotherm width in a thick plate. *Soldagem & Inspeção*, 19:212–220, 2014.
- [36] Howard E. Boyer, editor. *Atlas of Fatigue Curves*. Metals Park, 1986.
- [37] D. Arola and C. L. Williams. Estimating the fatigue stress concentration factor of machined surfaces. *International Journal of Fatigue*, 24(9):923–930, 2002.
- [38] H Neuber. Theorie der Entlastungskerven. In *Kerbspannungslehre*, pages 157–163. Springer-Verlag, Berlin, 2nd. edition, 1958.
- [39] Walter D. Pilkey and Deborah F. Pilkey. *Peterson's Stress Concentration Factors*. Wiley, 3rd. edition, 2008.

Appendix A – Full Scale Monotonic Tensile Testing

5.1 Introduction

Full-scale monotonic tensile testing was conducted at the Morrison Structural Engineering Laboratory using a 1 M-lb test frame. Samples corresponding to each condition (control, no preheat, 300°F preheat, 600°F preheat) were tested using the finished machined specimen geometry shown in Figure 6.1. The measured tensile properties and the 4140 substrate material test report (MTR) are provided in the subsequent sections. The tensile testing was stopped once the UTS had been exceeded, but before completed fracture had occurred, as such, no data is reported for % Elongation

Full scale monotonic tensile testing showed that laser cladding had a negligible effect on the bulk properties of the substrate. All tensile specimens, including the unprocessed control specimen, were found to have lower yield and ultimate stresses than was reported on the MTR. The difference in measured versus reported values can be attributed to the location and size of the MTR test specimen relative to the full scale coupons. The MTR reports the use of specimens of 0.505 inch diameter sectioned from the mid-radius of a 5 inch bar; the finished machined diameter of the full scale coupon is 1 inch below the mid-radius location. It has been well established that the tensile properties and hardness of low alloy steels in the heat treated and stress relieved condition decreases towards the

centre of large components.

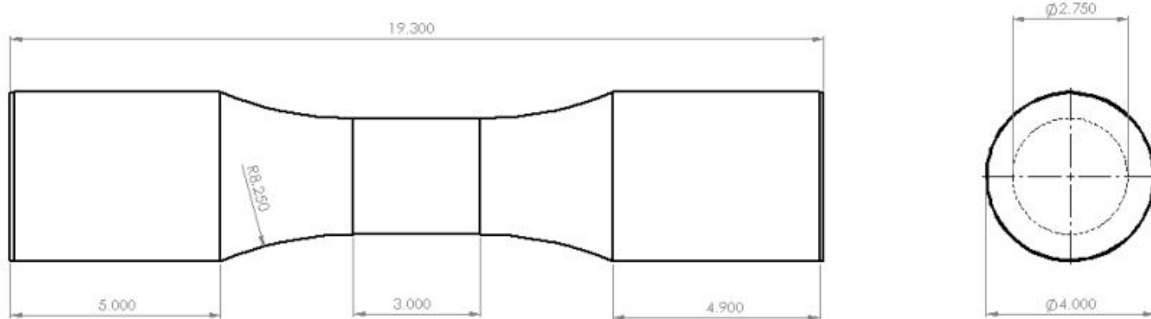


Figure 5.1: Finished machined monotonic tensile coupon geometry

5.2 Tensile Test Results

Table 5.1: Full scale monotonic tensile test data for each sample condition

| Specimen | $\sigma_{0.2\%}$ (MPa) | $\sigma_{0.2\%}$ (ksi) | σ_{UTS} (MPa) | σ_{UTS} (ksi) |
|----------|------------------------|------------------------|----------------------|----------------------|
| T-CO | 805.1 | 116.8 | 948.5 | 137.6 |
| T-NO | 783.7 | 113.7 | 959.9 | 139.2 |
| T-30 | 784.6 | 113.8 | 968.2 | 140.4 |
| T-60 | 784.4 | 113.8 | 975.4 | 141.5 |
| MTR | 891.2 | 129.3 | 1025.7 | 148.8 |

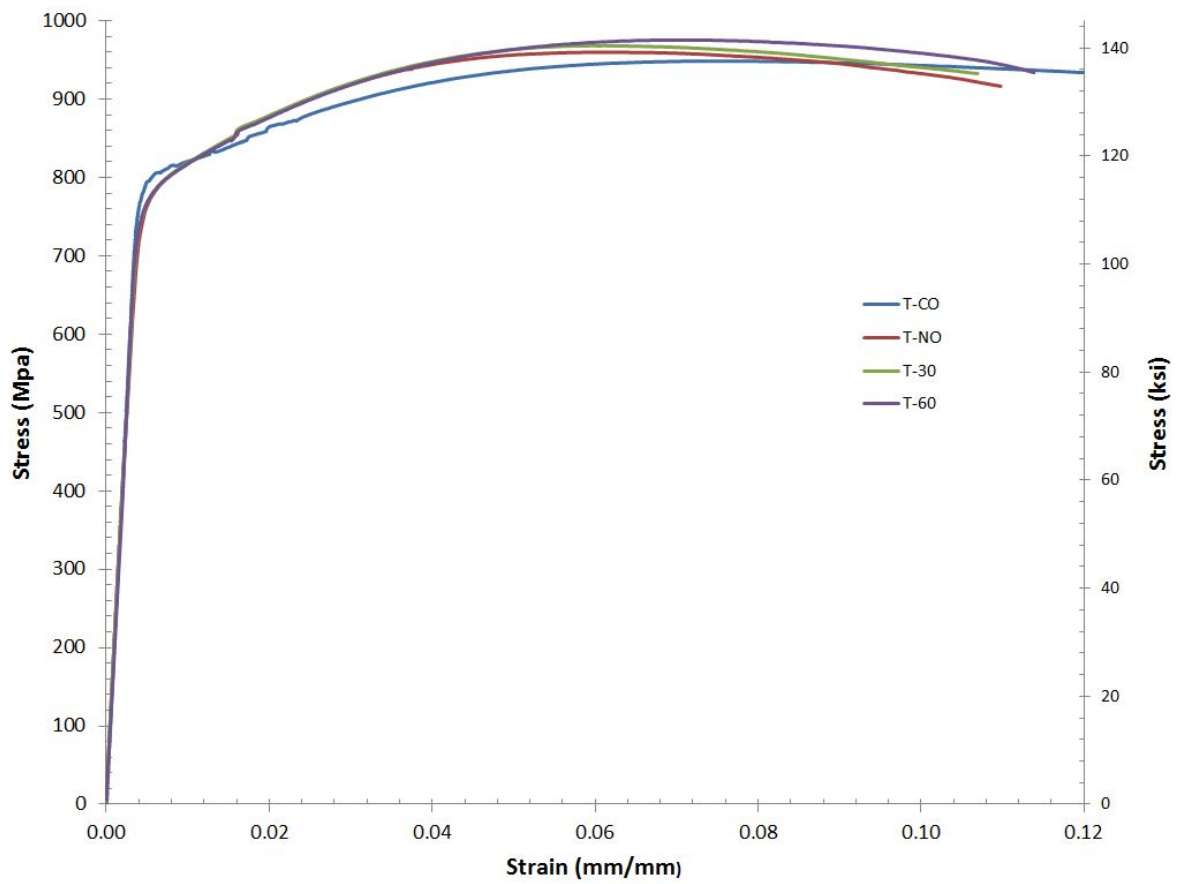


Figure 5.2: Full scale monotonic tensile curves for each sample condition

5.3 4140H Material Test Report (MTR)

Steel Certificate of Test

1835 Dueber Ave. S.W.
Canton, Ohio 44706

ID #0348778-1

Page 1 of 2

TIMKEN
Where You Turn
10/04/2013

1 of 2

S O L D
Encore Metals c/o RMCL
6925 8TH STREET
EDMONTON, AB T6P 1T9 Canada

S H I P
ENCORE METALS
9810 39th Avenue
Edmonton, AB T6E0A1 Canada

HEAT # N9164
P.O# P108066
R# R121797
ITEM # 506574

Customer Order: P108066-874 506574 Customer Part Number: 506574
Timken Order: 14420-D (1886030) Heat Number(s): N9164

Description of Material
DIAMETER: 5.000 in (127.000 mm)
Shape: RD
Sales Type: 4140
Int Quality: ELECTRIC FURNACE-VACUUM DEGAS-ULTRASONIC
Condition: HOT ROLL - QUENCH - TEMPER - STRESS FREE

Specification
- ASTM A 434 CLASS BD Rev. 06 (Reapproved 2012) EXCEPT AS NOTED
- ASTM A 29 / A 29M Rev. 12
- API 6A Rev. TWENTIETH EDITION 04/01/2011 FOR UT ONLY - EXCEPT AS NOTED
- ASTM A 388 / A 388M Rev. 11 04/01/2011 FOR INTERNAL DEFECTS ONLY-EXCEPT AS NOTED

Chemistry Information

| | %C | %Mn | %P | %S | %Si | %Cr | %Ni | %Mo | %Cu | %Al | %V |
|-----------------|-----|------|------|------|-----|------|-----|-----|-----|------|------|
| SPEC Ladle Min: | .40 | .75 | | .025 | .15 | .80 | | .15 | | | |
| SPEC Ladle Max: | .43 | 1.00 | .025 | .025 | .35 | 1.10 | | .25 | | | |
| N9164 Ladle: | .42 | .98 | .010 | .022 | .26 | .98 | .14 | .20 | .19 | .028 | .006 |

Metallurgy Information
SPEC: Chemistry DI ASTM-A255 5.50 Min
Heat N9164 DI ASTM-A255: 6.25
SPEC: Chemistry Phos + Sulfur 0.040 Max
Heat N9164 Phos + Sulfur: 0.032
SPEC: Chemistry DI CAT (TIMKEN INT) 6 Min
Heat N9164
SPEC: Grain Size SIZE 5/FINER
5/FINER
SPEC: Hardness UOM BRINELL HARDNESS 285 Min 341 Max LOCATION MID
Heat Piece# UOM
N9164 MID HARDNESS 311 / 315 BRINELL
MID LOCATION MID / MID BRINELL

When shipping document is attached it becomes part of this certification.

We certify the above materials have been inspected and tested in accordance with the methods prescribed in the governing specifications and consistent with our Standard Commercial Terms and Conditions for Sale, Manufacture, and Shipping, which are incorporated into and made part of this certification. The results of such inspections and tests conform with the applicable requirements including the purchase order, specification(s) and exception(s). This certificate or report shall not be reproduced except in full, without the written approval of the Timken Corporation.

Notarized: _____ by Cheryl Haas
NOTARY PUBLIC Cheryl Haas, Metallographer

THE TIMKEN CORPORATION

Steel Certificate of Test

1835 Dueber Ave. S.W.
Canton, Ohio 44706

TIMKEN

Where You Turn

10/04/2013

ID #0348778-1

Page 2 of 2

Customer Order: P108066-874 506574 Customer Part Number: 506574
Timken Order: 14420-D (1886030) Heat Number(s): N9164

Metallurgy Information

SPEC: Hardness UOM BRINELL HARDNESS 341 Max LOCATION SURFACE

| Heat | Piece# | UOM | |
|-------|--------|--------------------|-----------------|
| N9164 | SURF | HARDNESS 339 / | 328 BRINELL |
| | SURF | LOCATION SURFACE / | SURFACE BRINELL |

SPEC: Impacts (Info Only) DIRECTION LONGITUDINAL ENERGY UOM FT-LBS LOCATION MID TEMPERATURE ROOM
TYPE CHARPY SPECIMEN SIZE FULL

| Heat | Piece# | Temp | 1 | 2 | 3 | Direction | Location | Type | Specimen Size |
|-------|--------|------|----|----|----|-----------|----------|-------------|---------------|
| N9164 | F001 | RT | 60 | 65 | 57 | LONG. | MID | CHARPY FULL | |

SPEC: Impacts (Info Only) DIRECTION LONGITUDINAL ENERGY UOM FT-LBS LOCATION MID TEMPERATURE +14
TEMPERATURE SCALE F TYPE CHARPY SPECIMEN SIZE FULL

| Heat | Piece# | Temp | 1 | 2 | 3 | Direction | Location | Type | Specimen Size |
|-------|--------|-------|----|----|----|-----------|----------|-------------|---------------|
| N9164 | F001 | +14 F | 37 | 35 | 37 | LONG. | MID | CHARPY FULL | |

SPEC: Tensile TENSILE 135,000 Min STRENGTH UOM PSI YIELD .2 110,000 Min 140,000 Max MIN
ELONGATION 14.0 Min GAUGE LENGTH 2 IN MIN REDUCTION IN AREA 35.0 Min SPECIMEN SIZE .505"
SHAPE ROUND DIRECTION LONGITUDINAL TEMPERATURE ROOM LOCATION MID

| Heat | Piece# | Tensile Strength | UOM | .2% Yld Strength | Elong% | Gauge Length | %Red | Specimen | Direction | Temp | Location |
|-------|--------|------------------|-----|------------------|--------|--------------|------|----------|-----------|------|----------|
| N9164 | B14 | 149,390 | PSI | 130,357 | 15.4 | 2 IN | 49.6 | .505" | RD LONG. | RT | MID |
| | F001 | 148,130 | PSI | 128,169 | 16.0 | 2 IN | 52.5 | .505" | RD LONG. | RT | MID |

SPEC: Ultrasonic Inspection CLASS B

Heat N9164

Heat Treatment

Heat: N9164 Lot: 1
AUSTENITIZED - 1475 F - 0.4 hour(s) - WATER quenched
TEMPERED - 1125 F - 0.6 hour(s)

Heat N9164 Melt Source: USA
Manufacturing: USA
MATERIAL UT INSPECTED TO A 3.2MM FBH IN ACCORDANCE WITH ASTM A388 AND API 6A - RESULTS SATISFACTORY

In reference to Section 1502 ("Conflict Minerals") of the Dodd-Frank Wall Street Reform and Consumer Protection Act, no tantalum, tin, tungsten or gold was intentionally added to this material.

THE TIMKEN CORPORATION

Appendix B – Surface Finish Characterization

6.1 Introduction

The fatigue performance of a given material or component is sensitive to surface roughness or the presence of stress raisers at the surface. [36] In general, decreasing the surface roughness will minimize local stress risers and produce increased fatigue performance. [37] For most experimental fatigue test applications, the effect of surface finish is negated by testing samples with a metallographic surface finish, i.e. a mirror finish, that is free of machining grooves or scratches. [36] In the context of this thesis study, a metallographic surface finish was undesirable as it would not be representative of most industrial components.

The effect of surface roughness on fatigue performance can be expressed through the effective stress concentration factor (K_t) and fatigue stress concentration factor (K_f) determined through the Neuber rule. [38] Neuber's approach involves treating surface roughness as a series of adjacent notches as shown in Figure 7.3. The surface stress

concentration factor can then be expressed as

$$K_t = 1 + n\sqrt{\lambda\frac{R_z}{\rho}} \quad (6.1)$$

where ρ is the notch root radius and R_z is given to be the height of the surface profile (surface roughness peak-to-valley distance). The value of n is a constant that defines the stress state ($n = 1$ for shear, and $n = 2$ for tension), and λ is the ratio of between notch spacing and height. [37] For most applications involving machined surfaces, λ is taken to be 1. [37].

The stress concentration factor obtained from Eq. 7.1 can then be used to calculate the fatigue stress concentration factor as [39]

$$K_f = 1 + q(K_t - 1) \quad (6.2)$$

where q refers to the notch sensitivity and can be expressed in terms of the profile radius ρ as [39]

$$q = \frac{1}{(1 + \gamma/\rho)} \quad (6.3)$$

The γ term in Eq. 7.3 is a material constant that can be expressed in terms of the ultimate tensile strength (σ_{UTS}) [37]

$$\gamma = 0.025\left(\frac{2070MPa}{\sigma_{UTS}}\right)^{1.8}mm \quad (6.4)$$

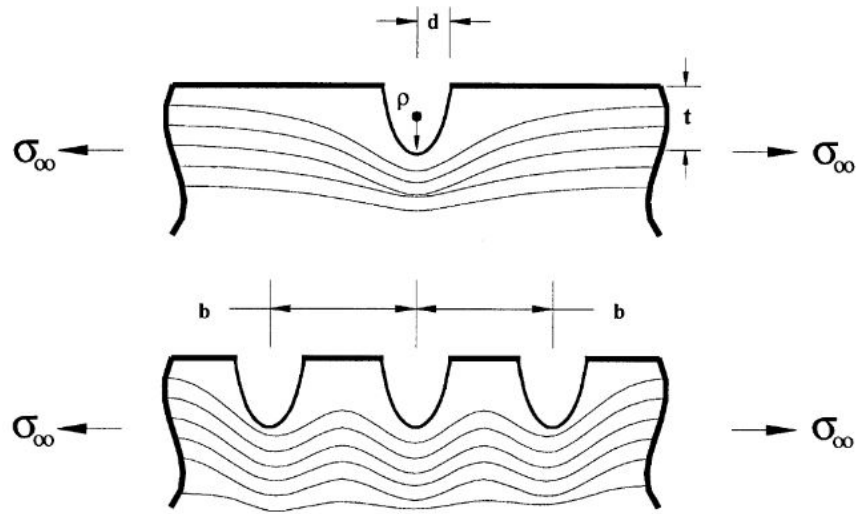


Figure 6.3: Schematic representation of surface roughness as a series of adjacent notches with a lower degree of stress concentration. From Ref. [37]

Because it was not possible to completely eliminate the potential effects of surface finish, it was necessary to classify surface finish as a nuisance variable. As outlined in Chapter 2, a nuisance variable is a test factor whose effect on the specimen is unintended and undesirable and that must be controlled through blocking. However, for blocking to be valid, the blocking variable cannot interact with the treatment variable [14]; i.e., the magnitude of the effect of surface finish on fatigue cannot be dependant on whether or not a sample was laser clad. From Eq. 7.1 – Eq. 7.3 it can be seen that the magnitude of the surface roughness effects are primarily determined by the notch radius, ρ . Thus, in order to ensure that there are no interaction effects between laser cladding and surface finish; it is necessary to show that machining operations that produce equivalent roughness parameters (R_z) also produce equivalent notch radii (ρ).

6.2 Experimental Methodology

To determine the surface finish parameters R_z and ρ , detailed profilometry studies were conducted at the University of Alberta NanoFab facility. By using nanometer scale profilometers it was possible to precisely measure the radii of the machining marks produced by the same machining operations that would be utilized for manufacture of the fatigue specimens; i.e. turning on a CNC lathe and subsequent polishing with 220-grit emery paper to a 16 μ -inch R_a surface finish. The pre-clad coupon geometry used for the laser cladding surface finish assessment is shown in Figure 7.4. The un-clad 4140 surface finish sample comprised a bar machined to 2.830 inch diameter.

Two regions 180° apart were sectioned from each of the clad and unclad samples. The surface roughness of each specimen was then measured using an Alpha-Step IQ surface profiler. The surface roughness parameters and radii of 12 notches from each location (24 total for each the clad and unclad samples) were measured for each specimen. The resulting ρ measurements were statistically analyzed through the Mann-Whitney test to determine if they were statistically different.

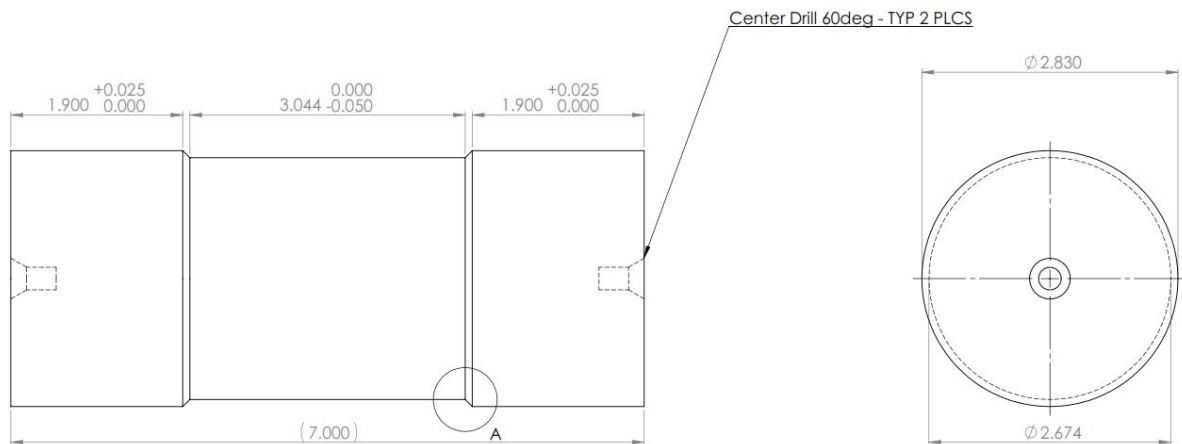


Figure 6.4: Pre-cladding Surface finish specimen dimensions. Following laser processing the sample was machined flush to the 2.830 inch diameter

6.3 Profilometry Results

The measurements data for each of the clad and unclad specimens is given in Figures 7.5 – 7.24. A summary of the measured data is given in Tables 7.2 and 7.3.

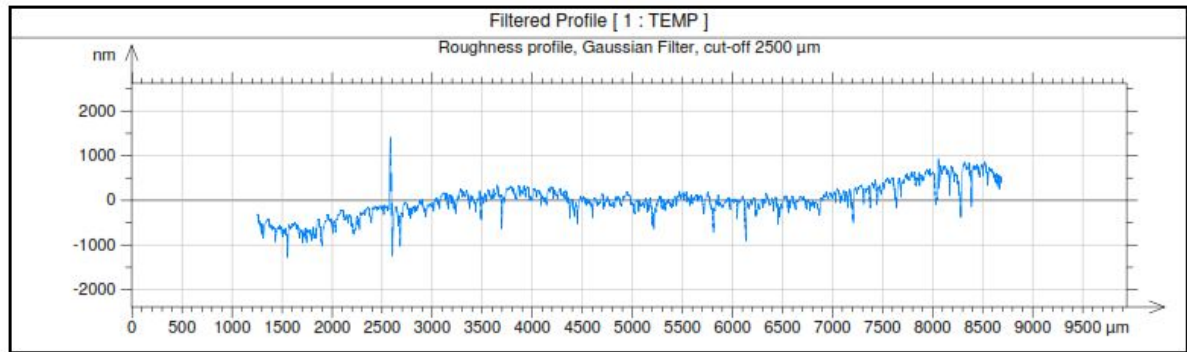
Table 6.2: Summary of measured surface roughness parameters

| Coupon | R _a (nm) | R _q (nm) | R _p (nm) | R _z (nm) |
|--------------------|---------------------|---------------------|---------------------|---------------------|
| Clad Specimen 1 | 271 | 345 | 857 | 2052 |
| Clad Specimen 2 | 403 | 507 | 1020 | 1840 |
| Average | 337 | 426 | 939 | 1946 |
| Control Specimen 1 | 439 | 531 | 1033 | 2614 |
| Control Specimen 2 | 386 | 495 | 650 | 2623 |
| Average | 413 | 513 | 842 | 2619 |

Table 6.3: Notch radii measured on both the control and clad surface finish specimens

| Clad Specimen 1 | Clad Specimen 2 | Control Specimen 1 | Control Specimen 2 |
|-----------------|-----------------|--------------------|--------------------|
| 120.0 | 64.2 | 97.8 | 27.7 |
| 67.3 | 23.7 | 23.8 | 74.3 |
| 40.7 | 105.0 | 72.7 | 19.4 |
| 19.8 | 38.9 | 90.9 | 60.6 |
| 24.9 | 39.1 | 15.0 | 98.7 |
| 29.4 | 29.3 | 27.5 | 37.5 |
| 120.0 | 16.3 | 40.2 | 61.7 |
| 47.9 | 35.7 | 23.8 | 43.4 |
| 26.1 | 13.5 | 18.3 | 23.5 |
| 20.0 | 23.0 | 15.8 | 74.6 |
| 47.5 | 166.0 | 18.4 | 116.0 |
| 87.2 | 66.2 | 106.0 | 208.0 |

6.3.1 Laser Clad Surface Roughness Data



| Results from Filtered Profile | |
|-------------------------------|--------------------|
| Ls | 8 μm |
| Lc | 2500 μm |
| Ra | 271 nm |
| Rq | 345 nm |
| Rp | 857 nm |
| Rv | 1195 nm |
| Rz | 2052 nm |
| Rt | 2810 nm |
| R3z | 1222 nm |

Figure 6.5: Clad sample specimen 1 roughness profile

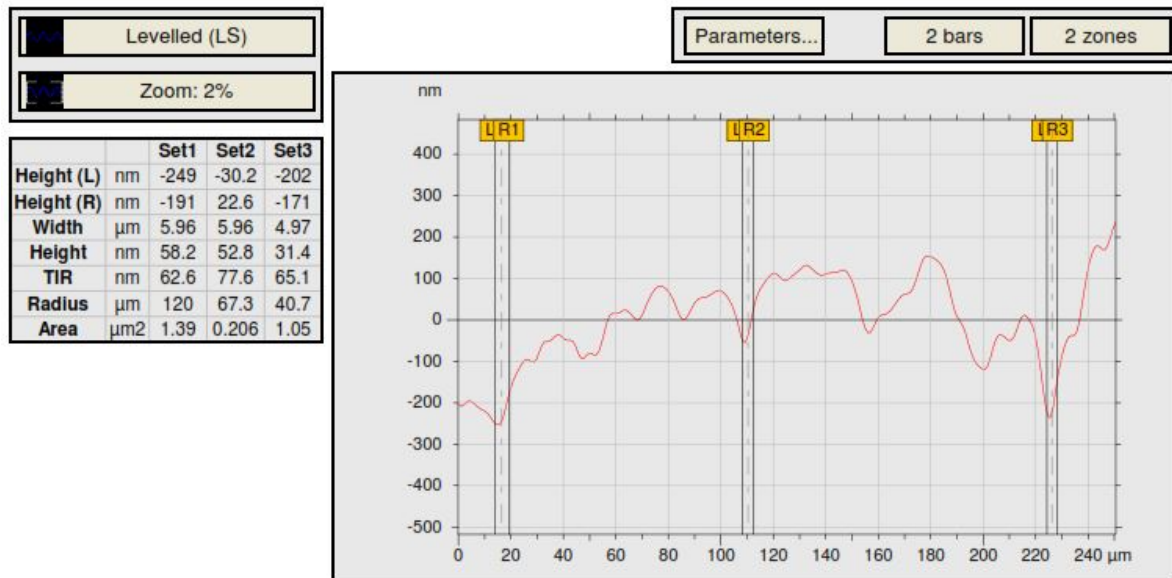


Figure 6.6: Notch radii measurements at location 1, which was randomly selected from the profile shown in Figure 7.5

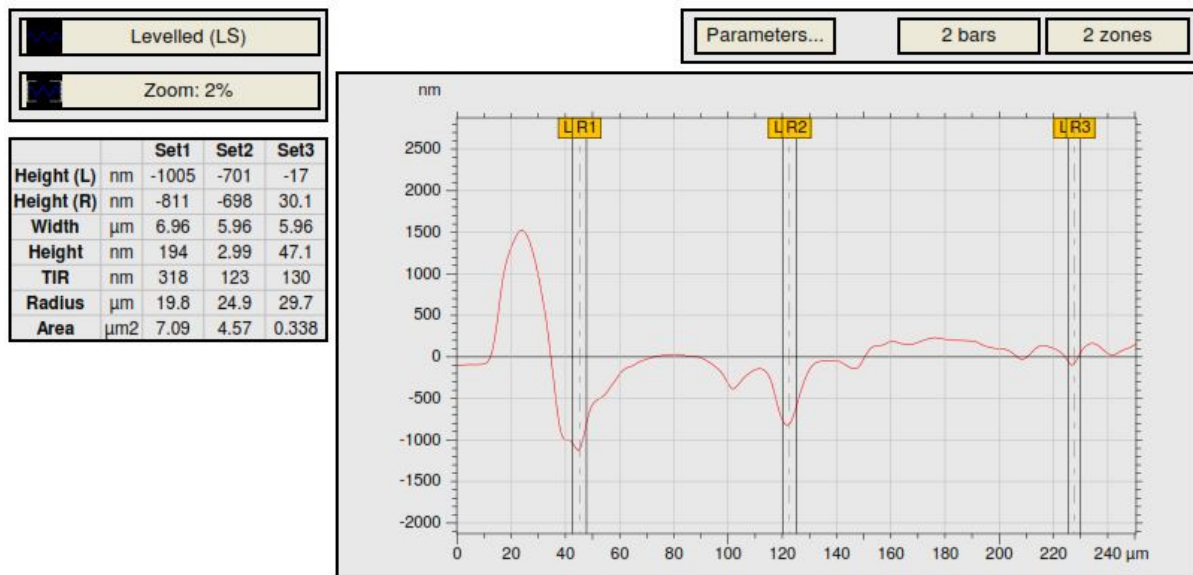


Figure 6.7: Notch radii measurements at location 2, which was randomly selected from the profile shown in Figure 7.5

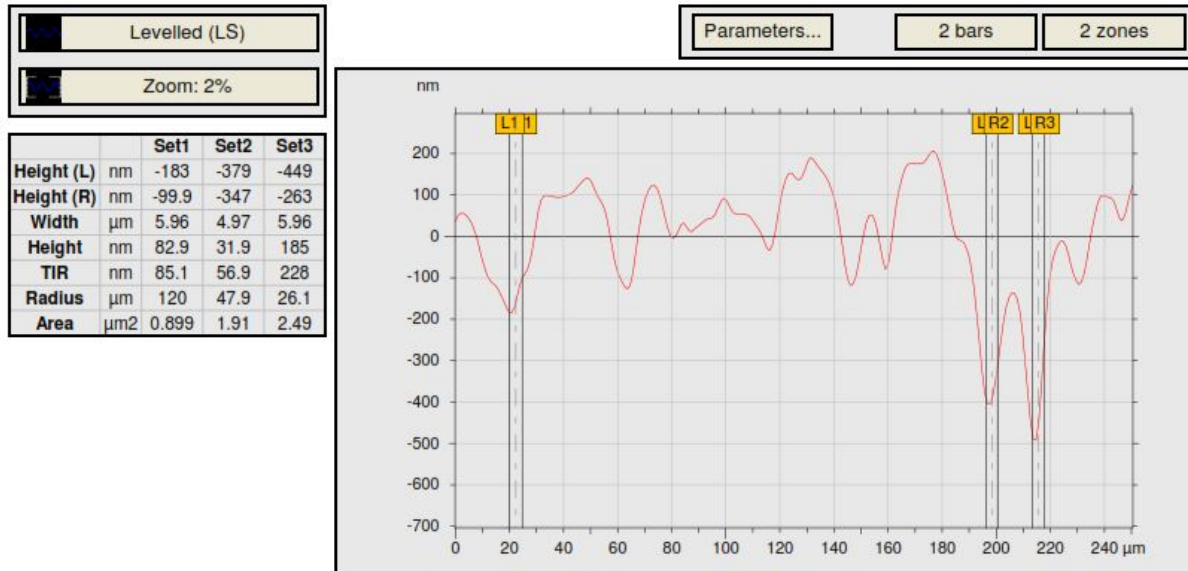


Figure 6.8: Notch radii measurements at location 3, which was randomly selected from the profile shown in Figure 7.5

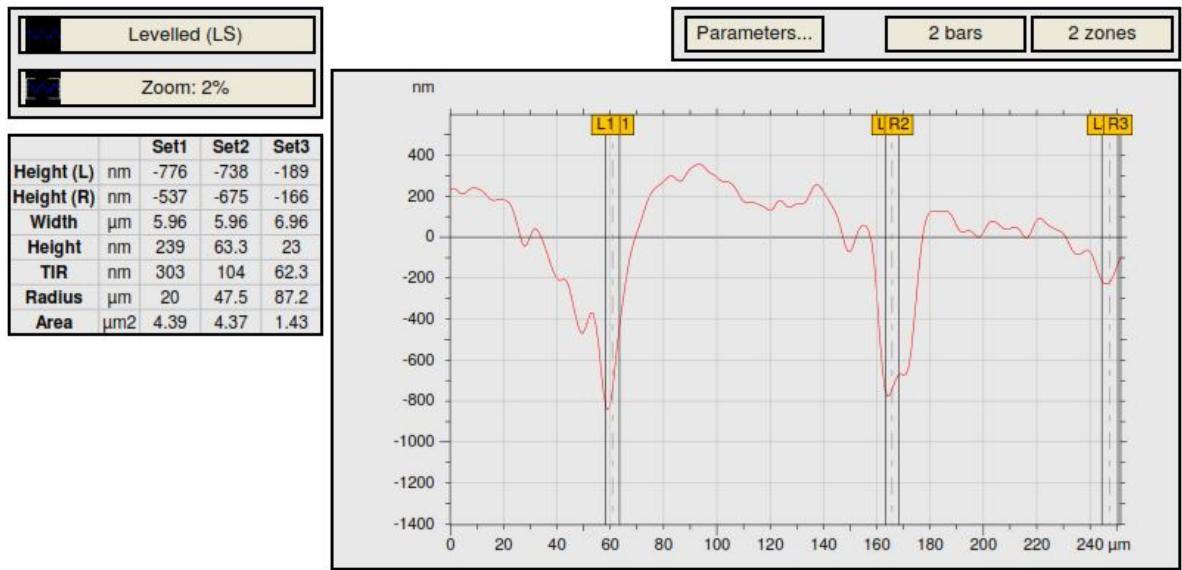


Figure 6.9: Notch radii measurements at location 4, which was randomly selected from the profile shown in Figure 7.5

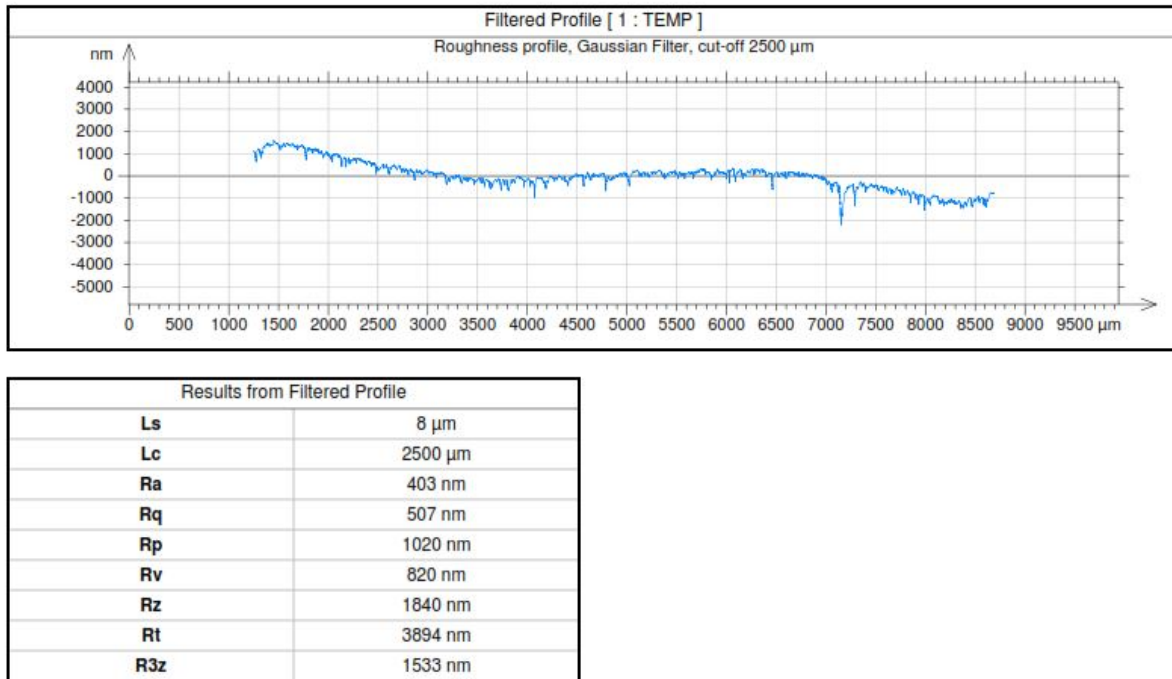


Figure 6.10: Clad sample specimen 2 roughness profile

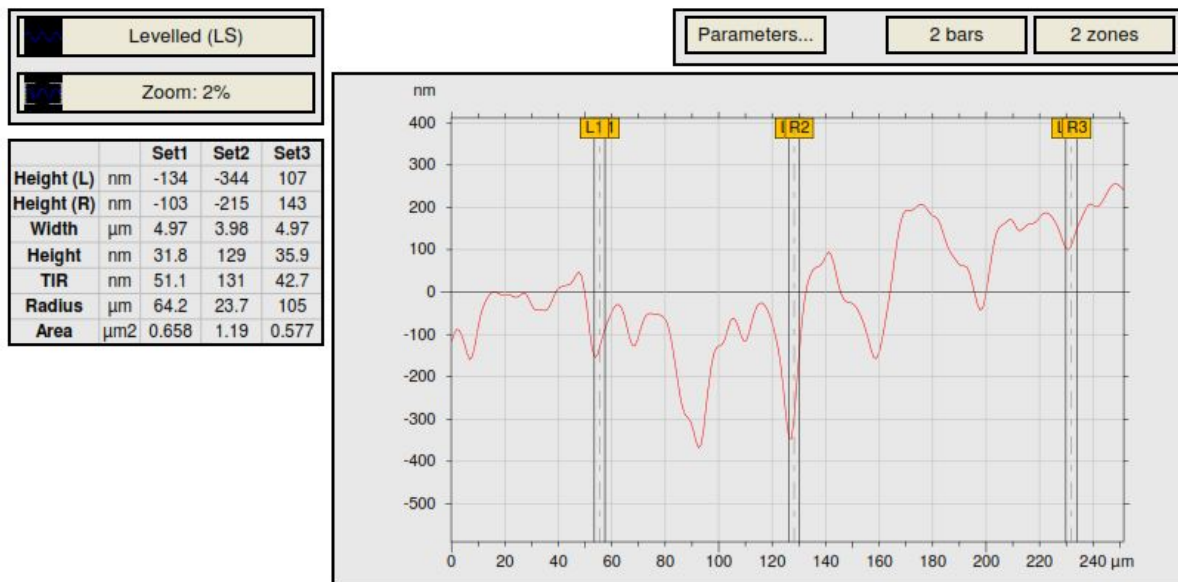


Figure 6.11: Notch radii measurements at location 1, which was randomly selected from the profile shown in Figure 7.10

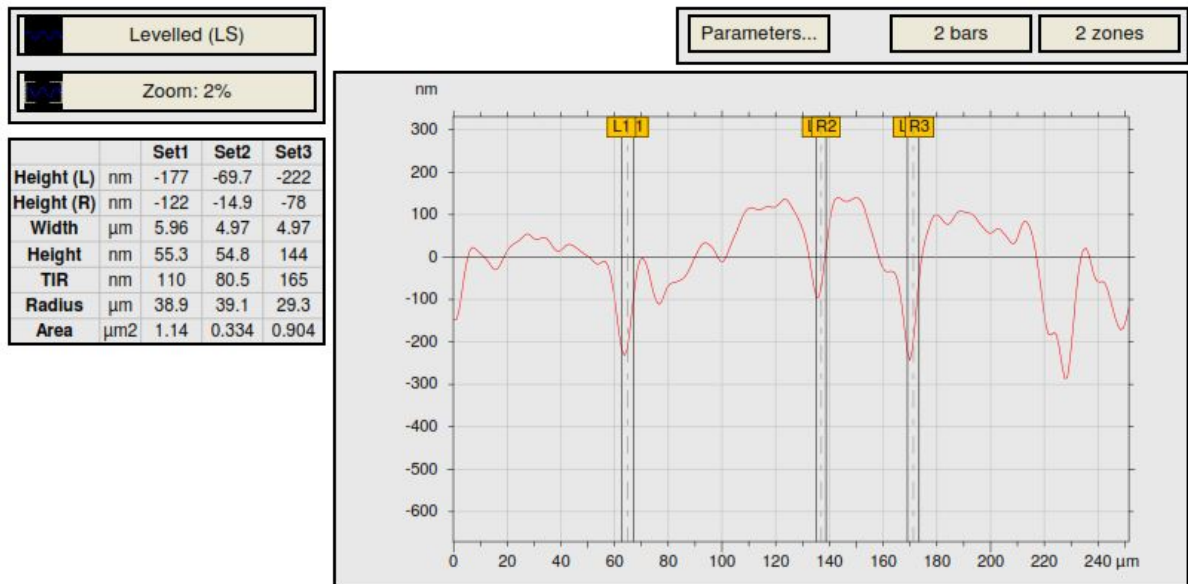


Figure 6.12: Notch radii measurements at location 2, which was randomly selected from the profile shown in Figure 7.10

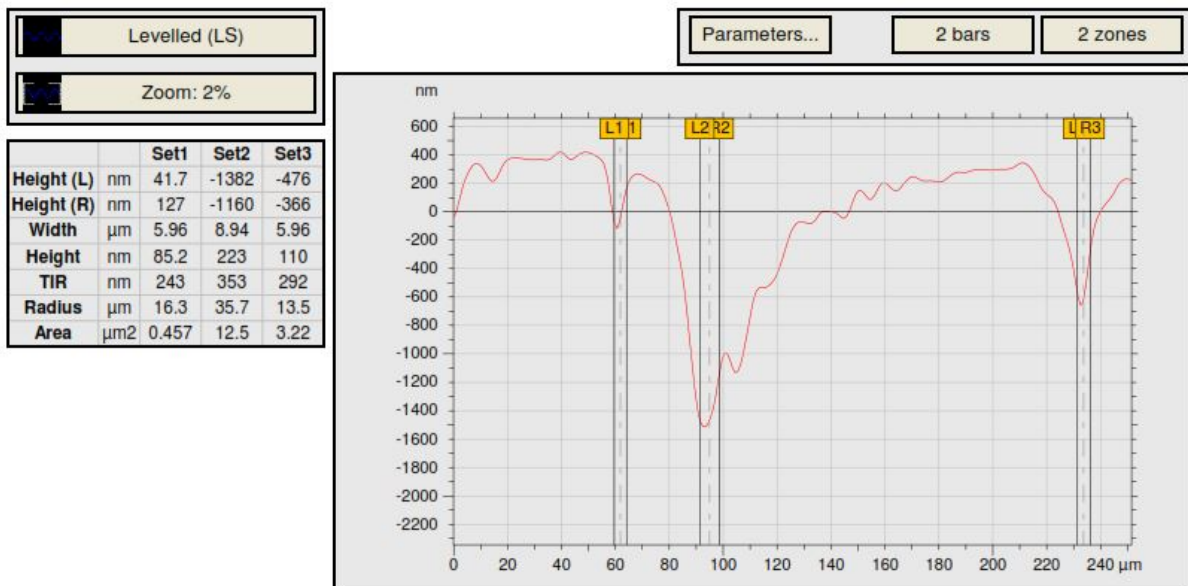


Figure 6.13: Notch radii measurements at location 3, which was randomly selected from the profile shown in Figure 7.10

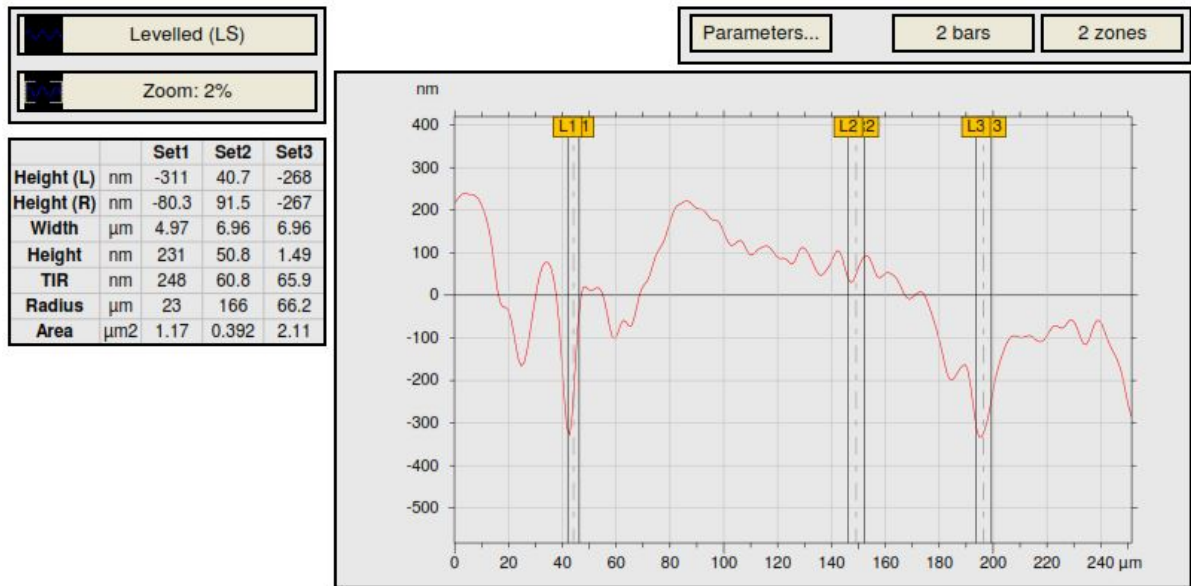


Figure 6.14: Notch radii measurements at location 4, which was randomly selected from the profile shown in Figure 7.10

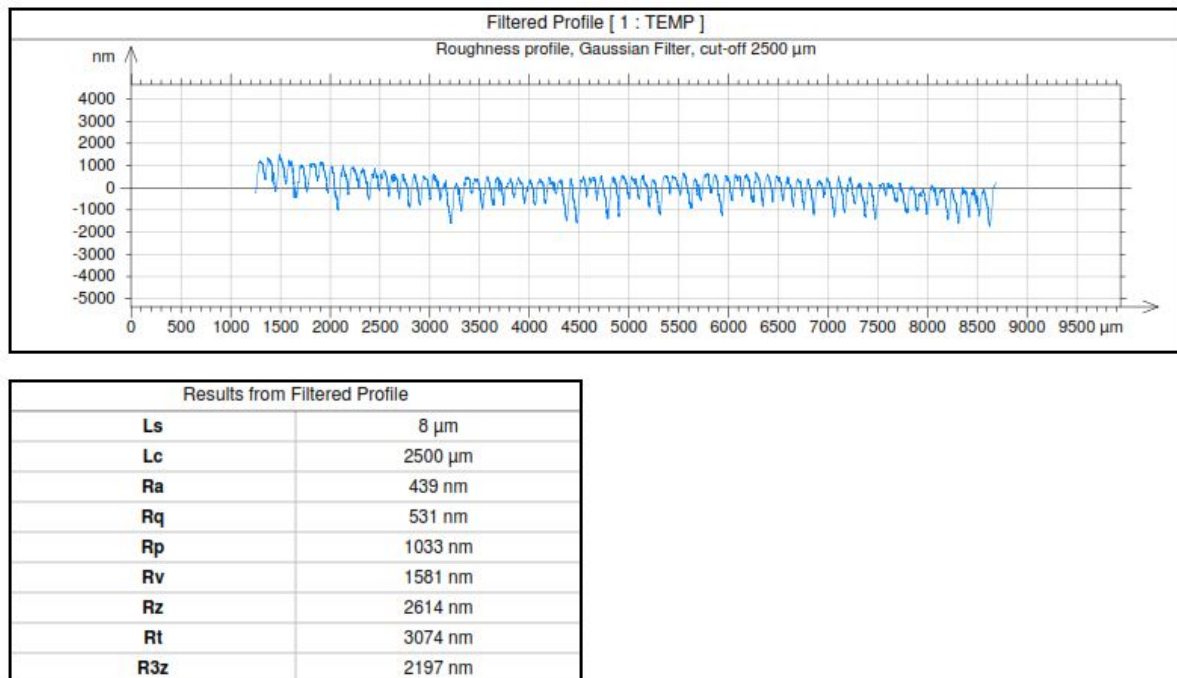


Figure 6.15: Control sample specimen 1 roughness profile

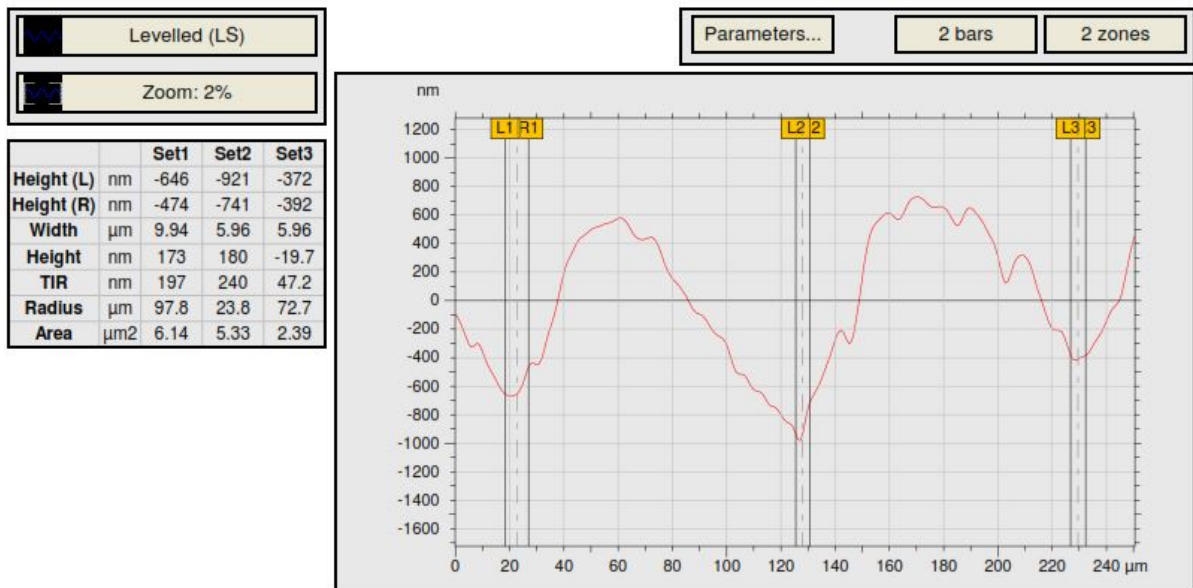


Figure 6.16: Notch radii measurements at location 1, which was randomly selected from the profile shown in Figure 7.15

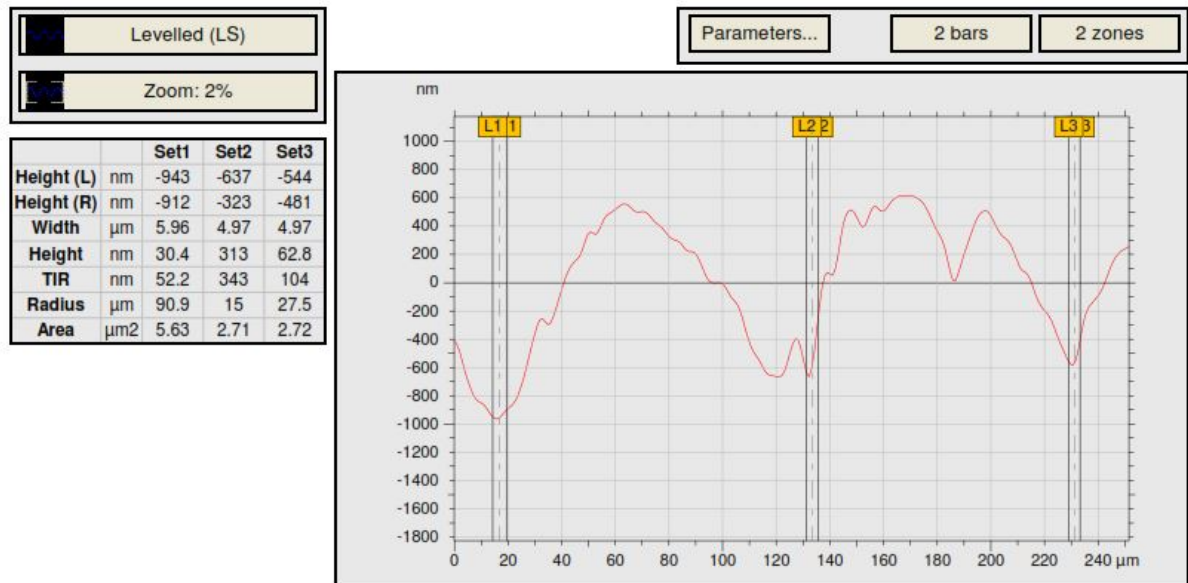


Figure 6.17: Notch radii measurements at location 2, which was randomly selected from the profile shown in Figure 7.15

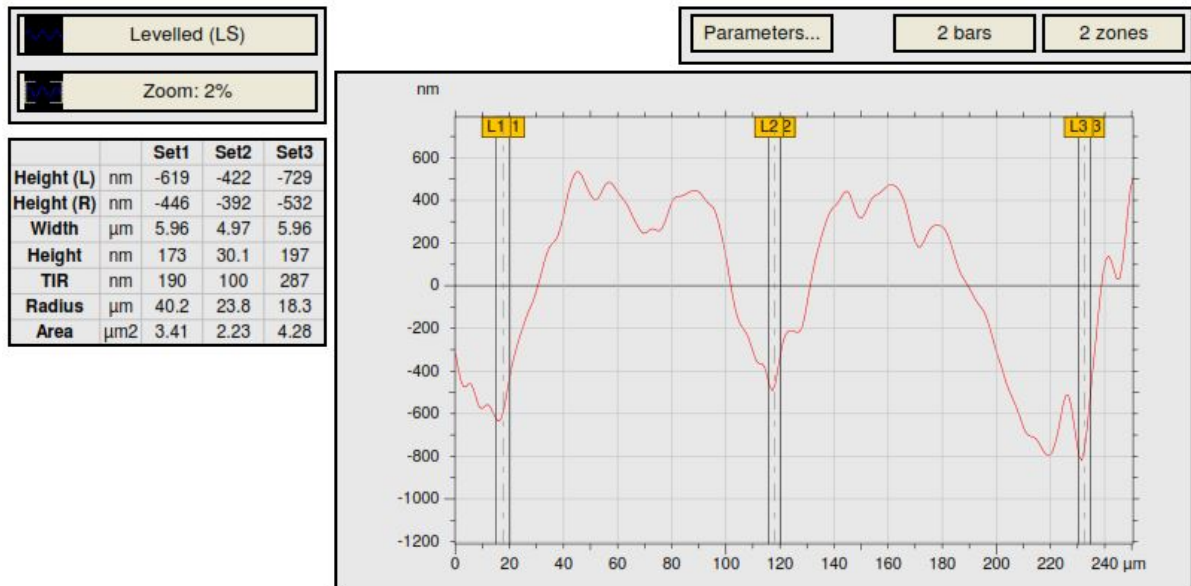


Figure 6.18: Notch radii measurements at location 3, which was randomly selected from the profile shown in Figure 7.15

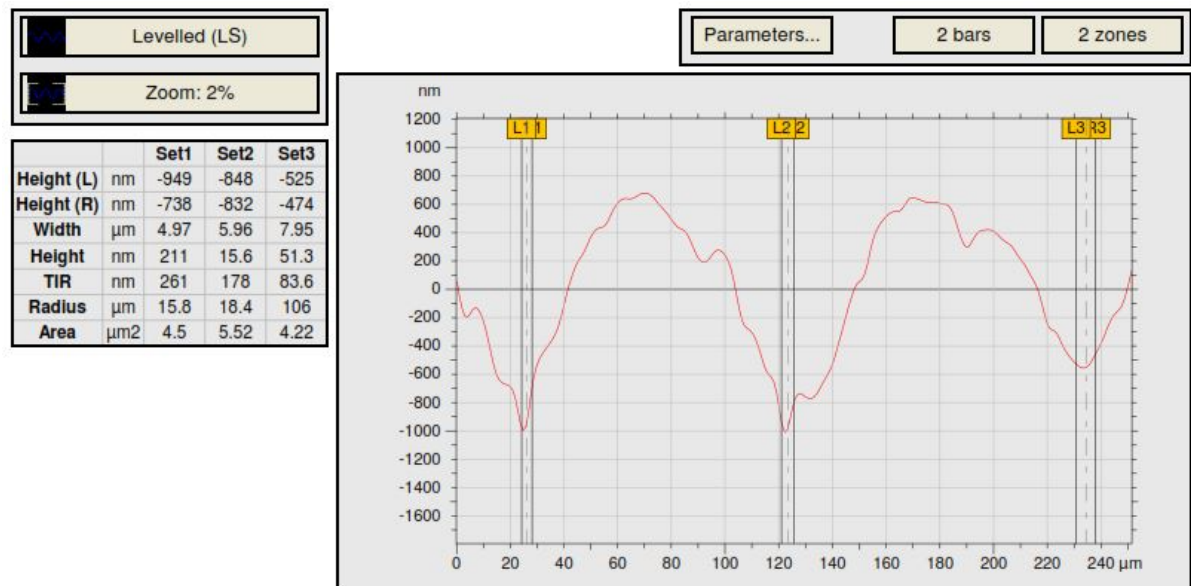


Figure 6.19: Notch radii measurements at location 4, which was randomly selected from the profile shown in Figure 7.15

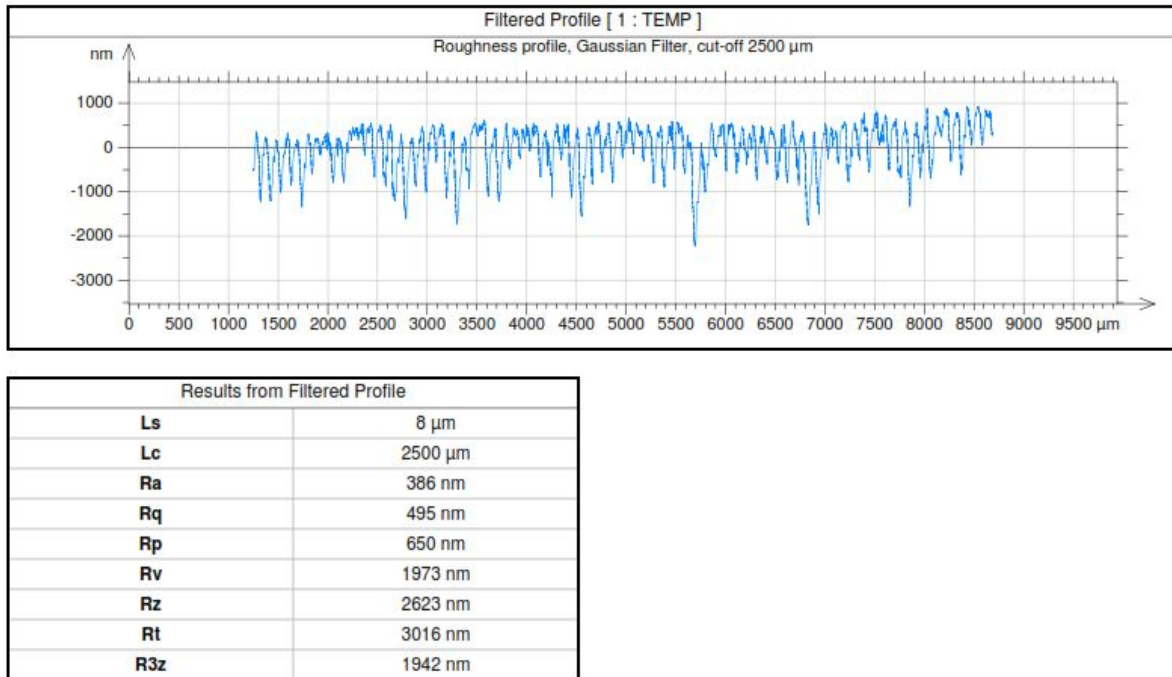


Figure 6.20: Control sample specimen 2 roughness profile

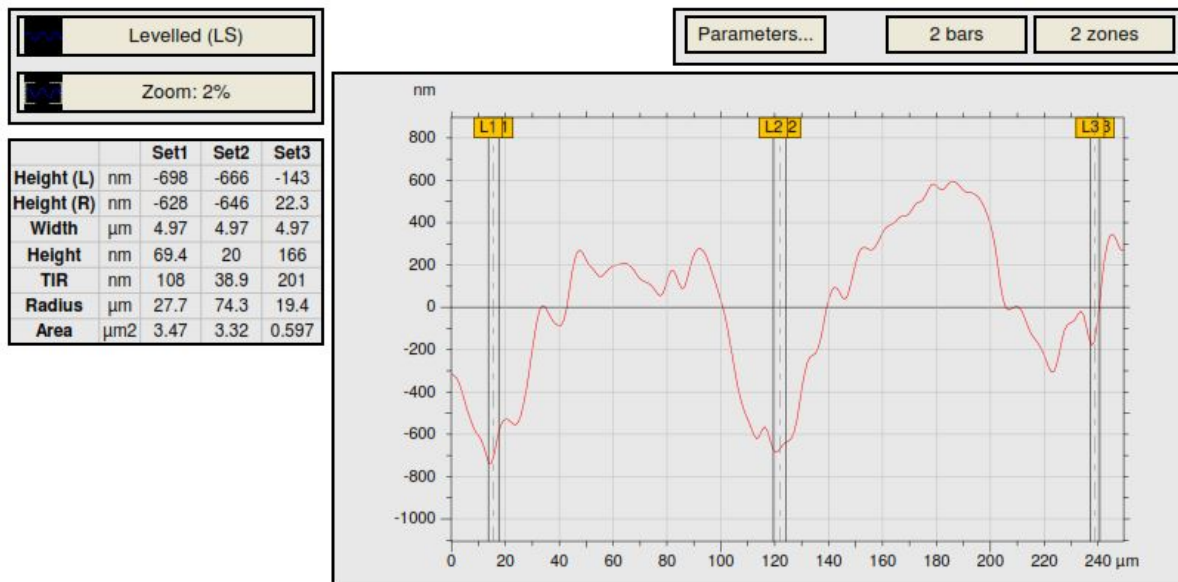


Figure 6.21: Notch radii measurements at location 1, which was randomly selected from the profile shown in Figure 7.20

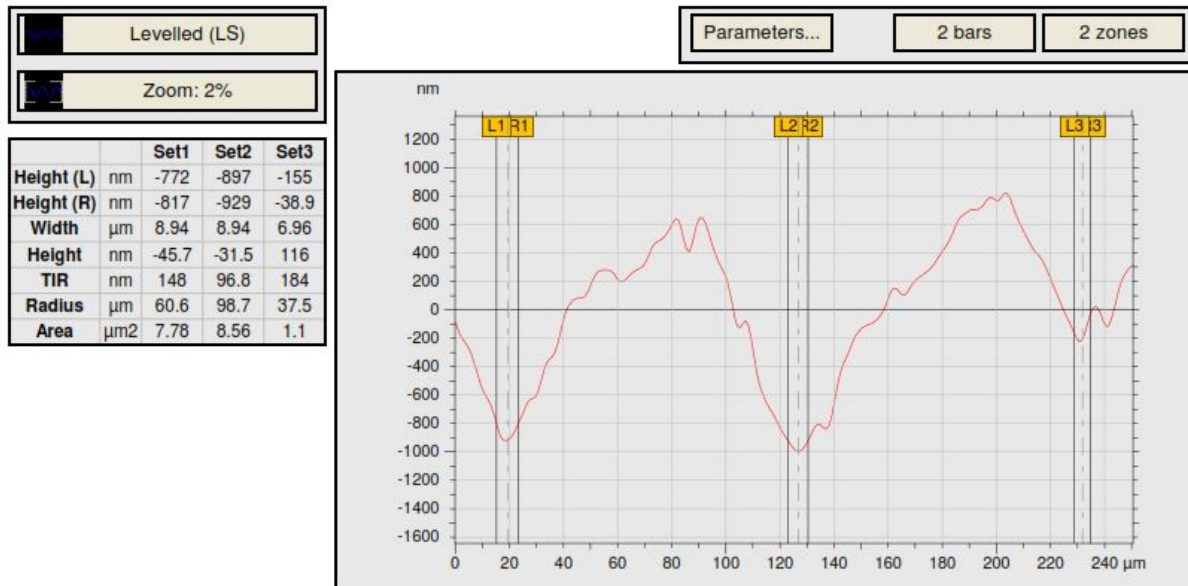


Figure 6.22: Notch radii measurements at location 2, which was randomly selected from the profile shown in Figure 7.20

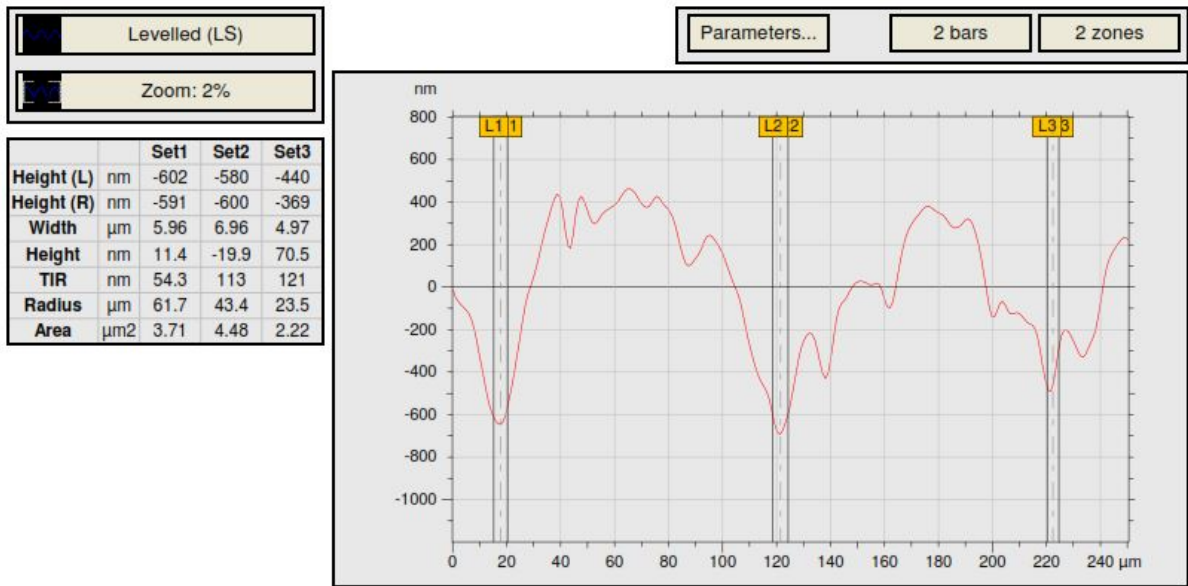


Figure 6.23: Notch radii measurements at location 3, which was randomly selected from the profile shown in Figure 7.20

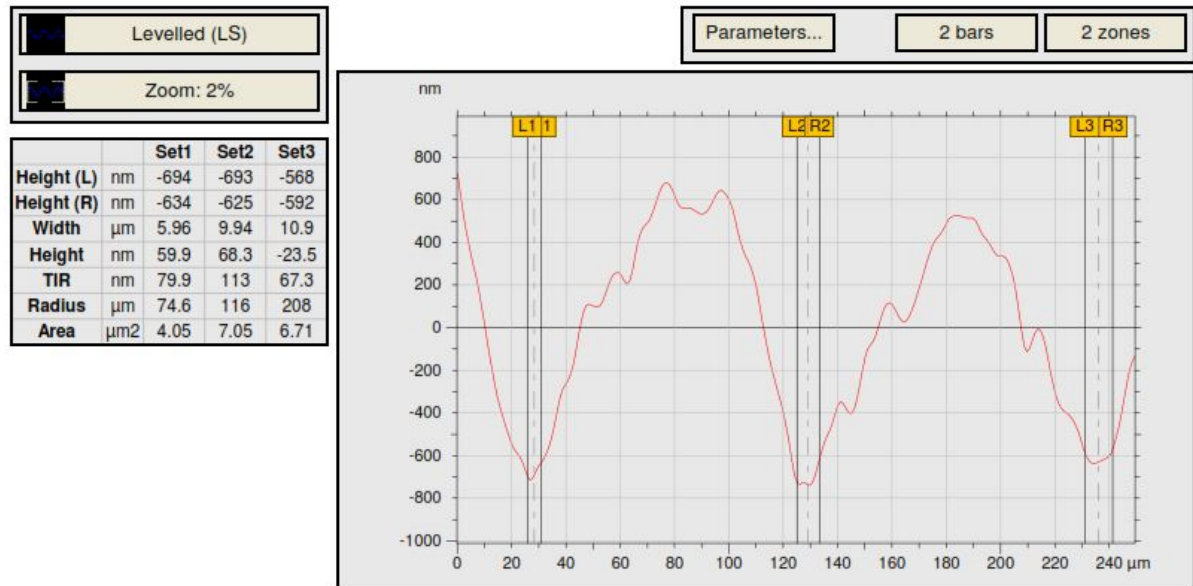


Figure 6.24: Notch radii measurements at location 4, which was randomly selected from the profile shown in Figure 7.20

6.4 Statistical Analysis: Mann-Whitney Test

The Mann-Whitney test is used to make inferences about the difference between two population medians based on data from random samples. In this case it was used to determine if the median of the notch radii for clad and control samples was the same. All calculations were carried out using MiniTab software.

The median notch radius was calculated to be $39.00 \mu\text{m}$ for the clad sample and $41.80 \mu\text{m}$ for the control sample. The Mann-Whitney statistic was calculated to be 582.0 and the associated p-value is 0.91. Therefore, there is no statistical difference between the notch radii at the 90% confidence interval.

6.5 Conclusion

Statistical analysis of the notch radii determined that there is no statistical difference in the machining induced surface roughness between clad and unclad samples. Therefore, the effect of surface roughness and laser cladding do not interact, and the effects of surface roughness can be managed through appropriate blocking.

Appendix C – Fractography

7.1 Introduction

Chapter 3 summarized the results of the fractographic analysis. The complete data set, including tabular summaries of the initiation locations and and fatigue data for each block, is provided below. The data is arranged alphabetically by block with scanning electron microscopy (SEM) data presented at the end. Where appropriate, electron dispersive spectroscopy (EDS) spectra and composition maps are provided below the relevant SEM image.

7.2 Optical Fractography

7.2.1 Block A

Table 7.4: Running stress, cycles to failure, and failure initiation location for the Block A samples

| Specimen | Cycles to Failure | Stress (psi) | Failure Initiation Location |
|----------|-------------------|--------------|-----------------------------|
| A-CO | 259197 | 55916 | Surface defect initiation |
| A-NO | 205670 | 54791 | Fusion Line Inclusion |
| A-30 | 157489 | 55892 | Fusion Line Inclusion |
| A-60 | 222112 | 56673 | Mid-overlay oxide |



Figure 7.25: A-CO coupon showing fracture initiation at a "dent" in the surface

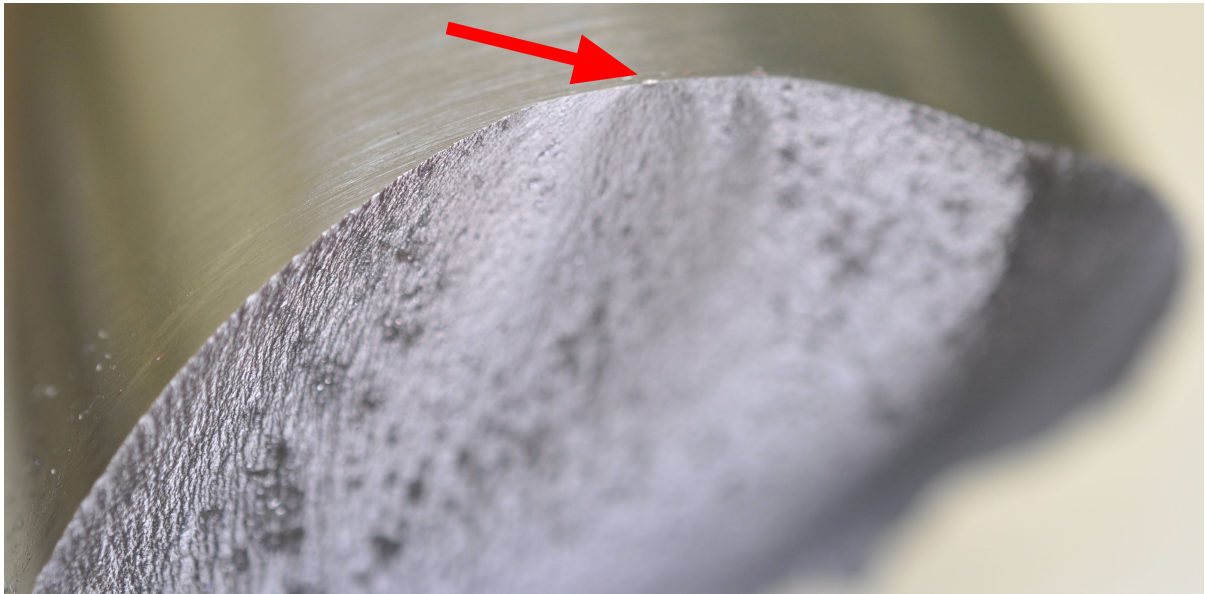


Figure 7.26: A-CO coupon OD view of initiating dent

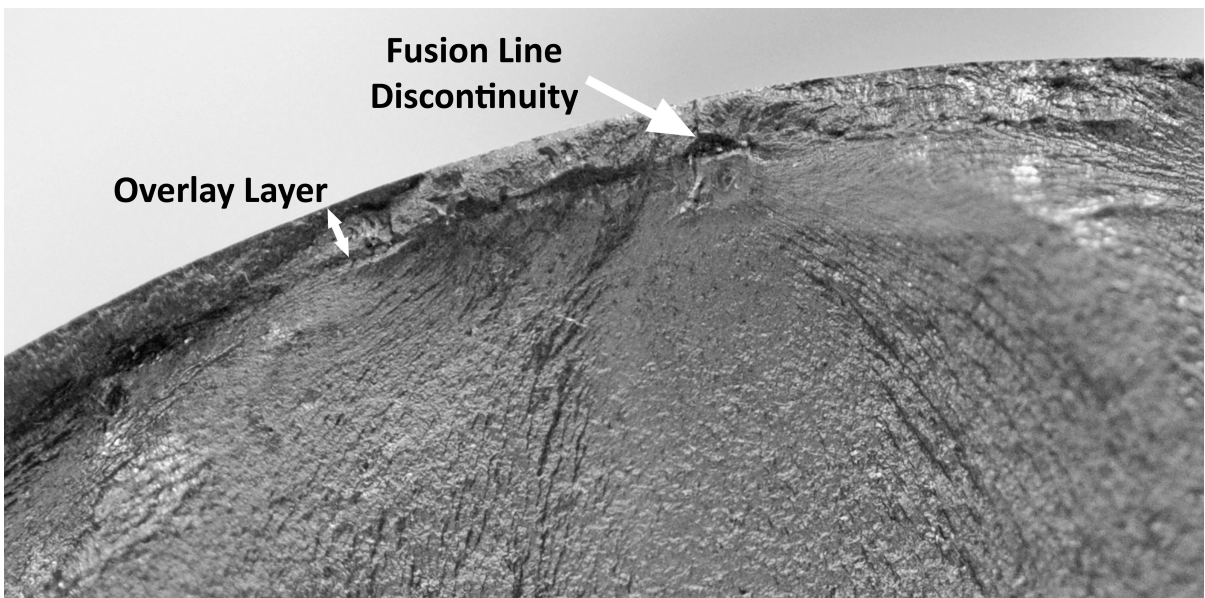


Figure 7.27: A-NO fracture initiation at an entrapped oxide located at the fusion line



Figure 7.28: A-30 fracture initiation at an multiple adjacent entrapped oxides located at the fusion line



Figure 7.29: A-60 fracture initiation at a circular entrapped oxide in the overlay region

7.2.2 Block B

Table 7.5: Running stress, cycles to failure, and failure initiation location for the Block B samples

| Specimen | Cycles to Failure | Stress (psi) | Failure Initiation Location |
|----------|-------------------|--------------|-----------------------------|
| B-CO | 140703 | 54918 | Surface Initiation |
| B-NO | 208567 | 57963 | Fusion Line Inclusion |
| B-30 | 522947 | 56410 | HAZ Inclusion |
| B-60 | 497976 | 54591 | HAZ Inclusion |



Figure 7.30: B-CO coupon fracture initiation at the surface



Figure 7.31: B-NO coupon fracture initiation at a fusion line oxide

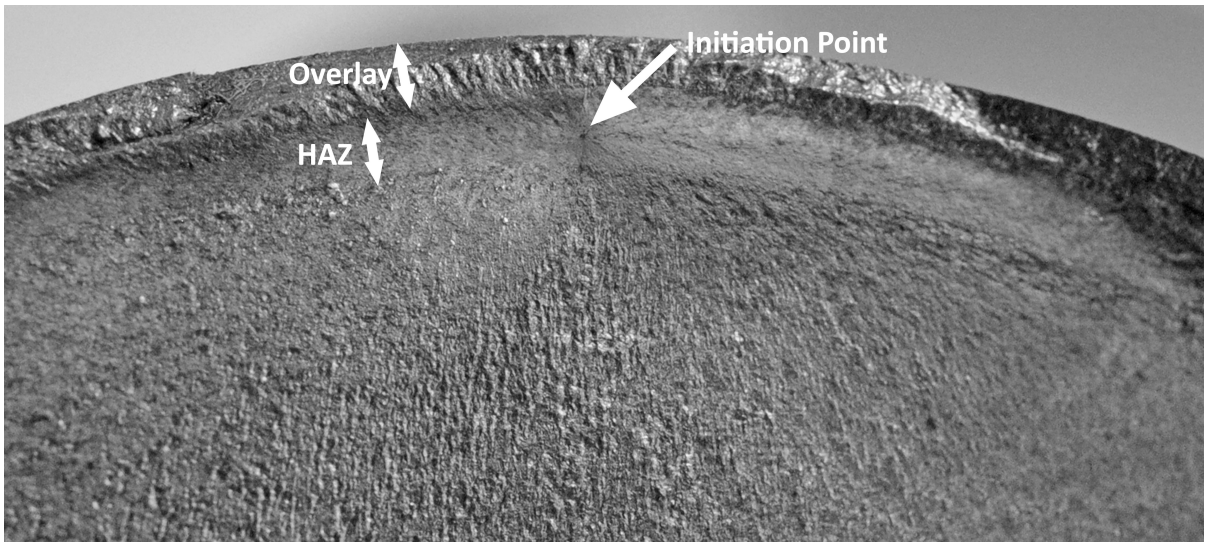


Figure 7.32: B-30 coupon fracture initiation at a non metallic inclusion located in the HAZ



Figure 7.33: B-60 coupon fracture initiation at a non metallic inclusion located in the HAZ

7.2.3 Block C

Table 7.6: Running stress, cycles to failure, and failure initiation location for the Block C samples

| Specimen | Cycles to Failure | Stress (psi) | Failure Initiation Location |
|----------|-------------------|--------------|-----------------------------|
| C-CO | 428793 | 55264 | Surface Initiation |
| C-NO | 103622 | 54301 | Fusion Line Inclusion |
| C-30 | 614668 | 55297 | HAZ Inclusion |
| C-60 | 195482 | 55080 | Fusion Line Discontinuity |



Figure 7.34: C-CO coupon fracture initiation at the surface

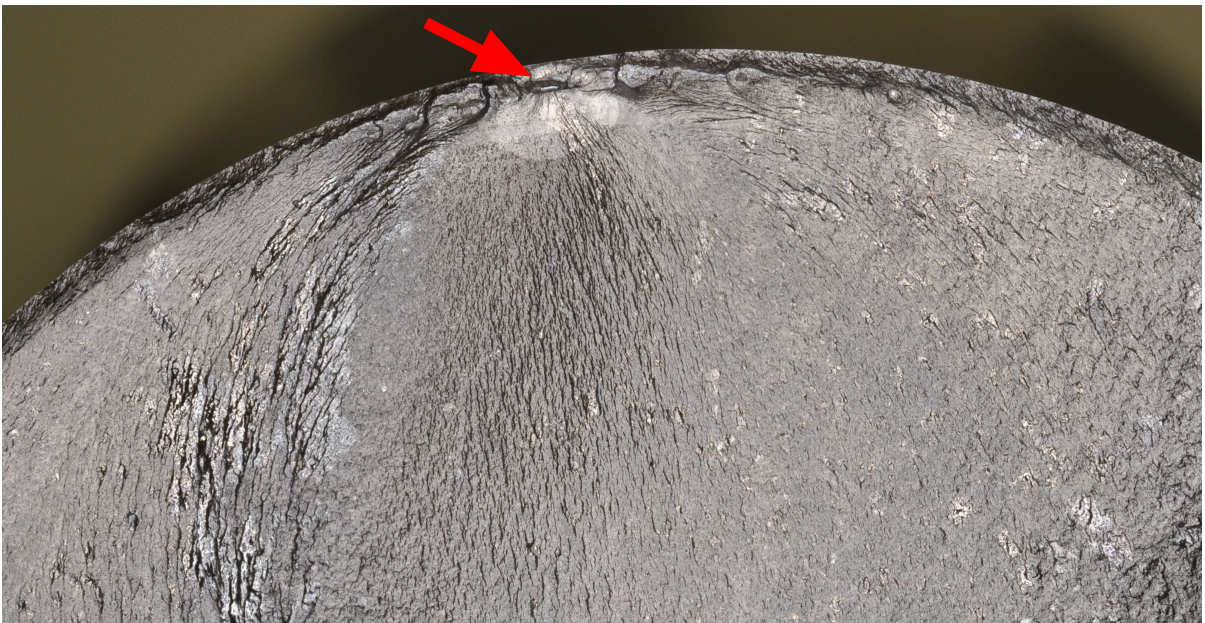


Figure 7.35: C-NO coupon fracture initiation at a fusion line oxide inclusion



Figure 7.36: C-30 coupon fracture initiation at a non metallic inclusion in the HAZ



Figure 7.37: C-60 coupon fracture initiation at a fusion line discontinuity

7.2.4 Block D

Table 7.7: Running stress, cycles to failure, and failure initiation location for the Block D samples

| Specimen | Cycles to Failure | Stress (psi) | Failure Initiation Location |
|----------|-------------------|--------------|-----------------------------|
| D-CO | 279969 | 53901 | Surface Initiation |
| D-NO | 306552 | 56438 | Fusion Line Discontinuity |
| D-30 | 252782 | 51895 | Fusion Line Inclusion |
| D-60 | 503252 | 56313 | Surface Initiation |



Figure 7.38: D-CO coupon fracture initiation at multiple locations on the surface



Figure 7.39: D-NO coupon fracture initiation at a fusion line discontinuity

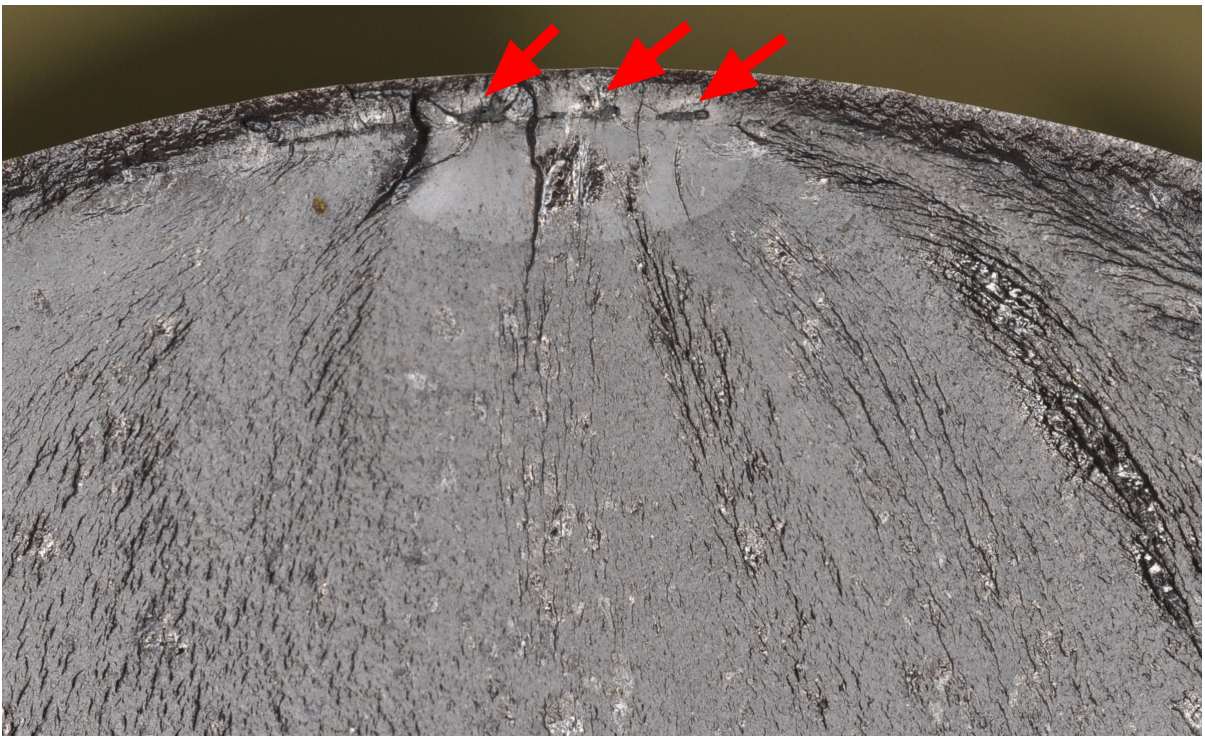


Figure 7.40: D-30 coupon fracture initiation at multiple fusion line oxide inclusions

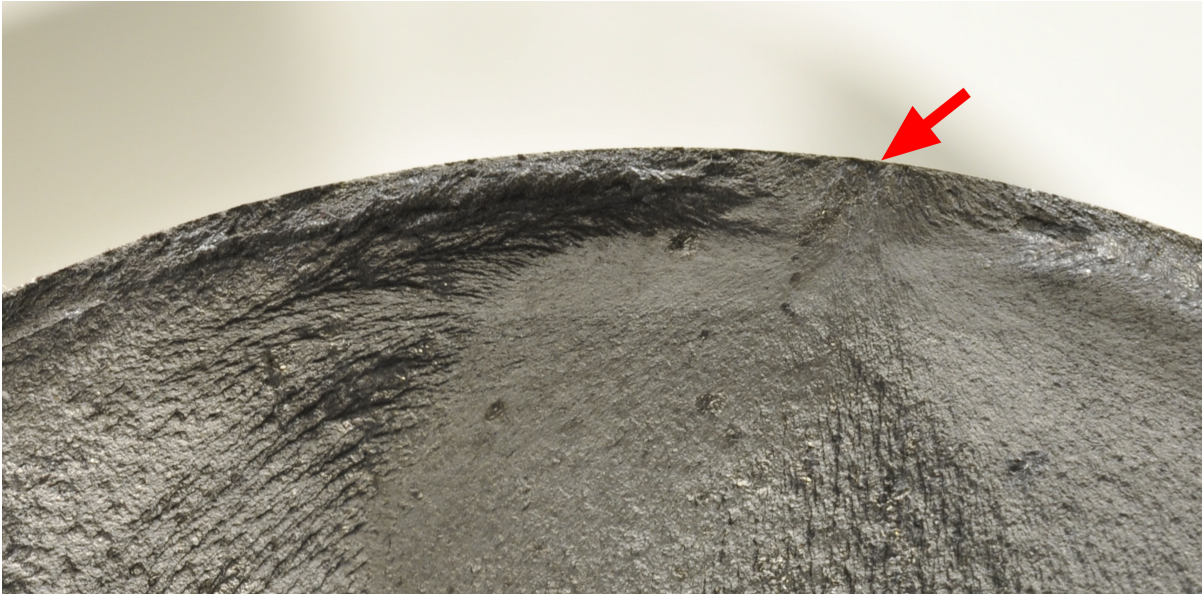


Figure 7.41: D-60 coupon fracture initiation at the surface

7.2.5 Block E

Table 7.8: Running stress, cycles to failure, and failure initiation location for the Block E samples

| Specimen | Cycles to Failure | Stress (psi) | Failure Initiation Location |
|----------|-------------------|--------------|-----------------------------|
| E-CO | 183848 | 55385 | Surface Initiation |
| E-NO | - | - | - |
| E-30 | 725759 | 54853 | HAZ Inclusion |
| E-60 | 154472 | 54437 | Fusion Line |



Figure 7.42: E-CO coupon fracture initiation at the surface



Figure 7.43: E-30 coupon fracture initiation at a non metallic inclusion located in the HAZ

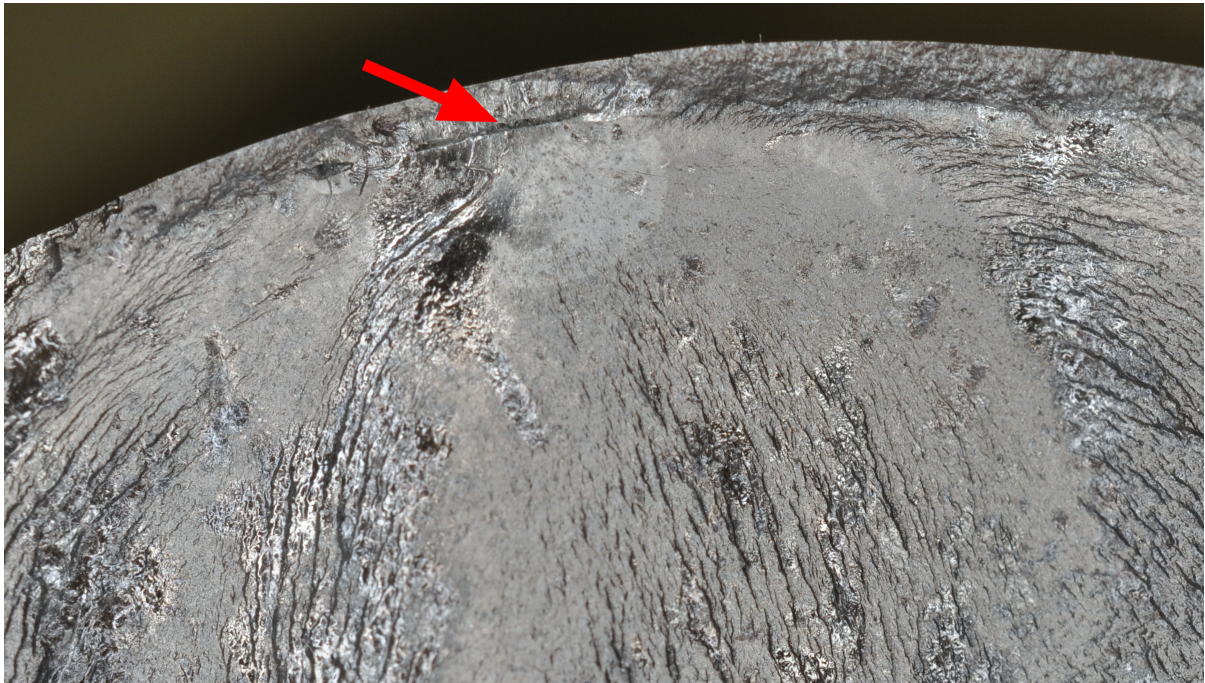


Figure 7.44: E-60 coupon fracture initiation at the fusion line

7.2.6 Block F

Table 7.9: Running stress, cycles to failure, and failure initiation location for the Block F samples

| Specimen | Cycles to Failure | Stress (psi) | Failure Initiation Location |
|----------|-------------------|--------------|---|
| F-CO | 235596 | 56107 | Surface and Near Surface Initiation |
| F-NO | 140504 | 57196 | Linear Fusion Line Defect and HAZ Inclusion |
| F-30 | 274486 | 57868 | Haz Inclusion |
| F-60 | 501034 | 56140 | Near Surface Porosity |

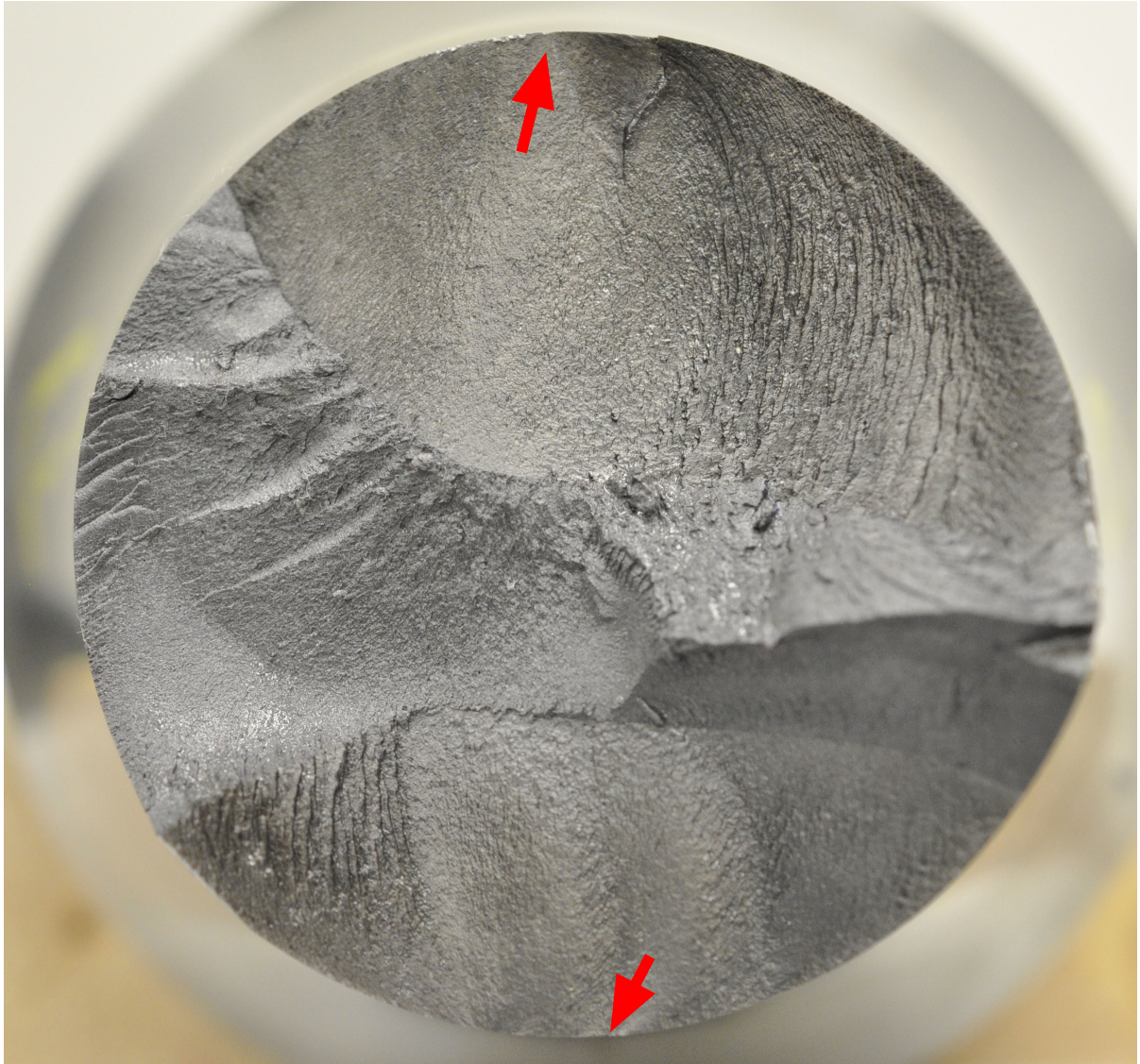


Figure 7.45: F-CO coupon overview showing initiation and propagation of multiple fractures

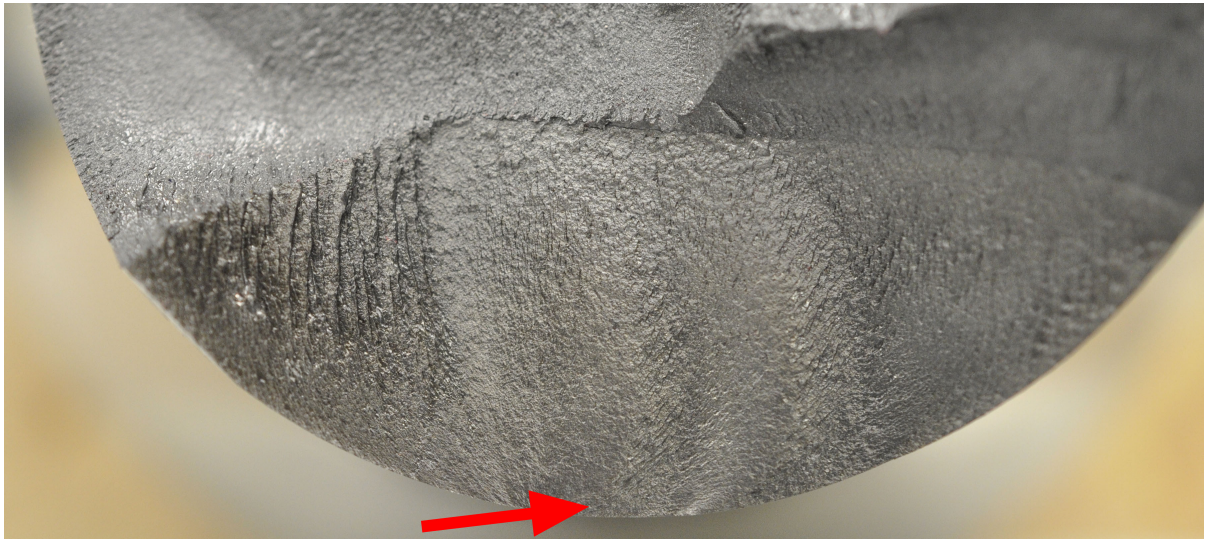


Figure 7.46: F-CO coupon surface initiation of the lower fracture shown in 8.45



Figure 7.47: F-CO coupon surface initiation of the upper fracture shown in Figure 8.45.

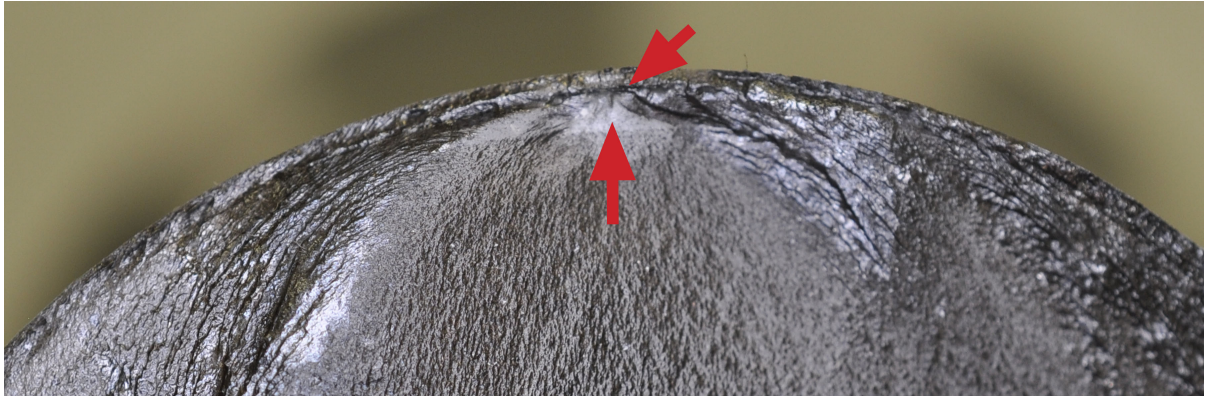


Figure 7.48: F-NO coupon showing adjacent initiation at a fusion line discontinuity and a non metallic inclusion located in the HAZ



Figure 7.49: F-30 coupon showing multiple fracture initiation locations. The fracture initiated at location 1 dominated failure



Figure 7.50: Location 1 of the F-30 fracture shown in Figure 8.49. Initiation occurred at a non metallic inclusion in the HAZ

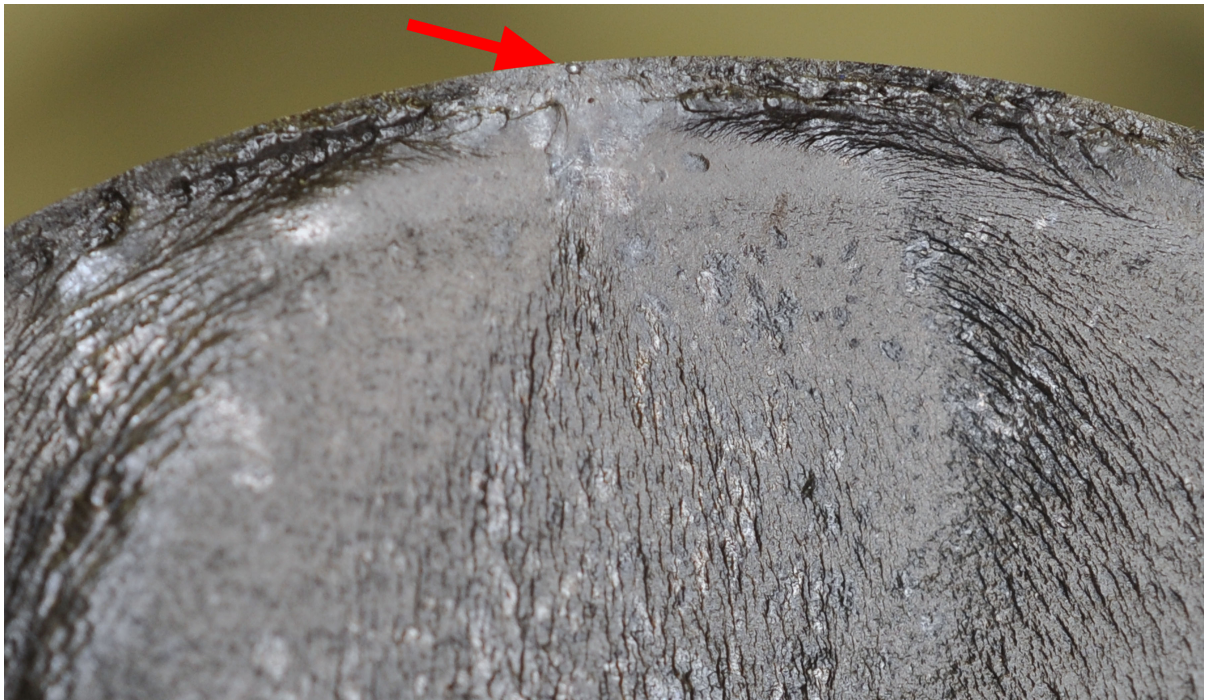


Figure 7.51: F-60 coupon fracture initiated at porosity in the overlay layer

7.3 SEM Fractography

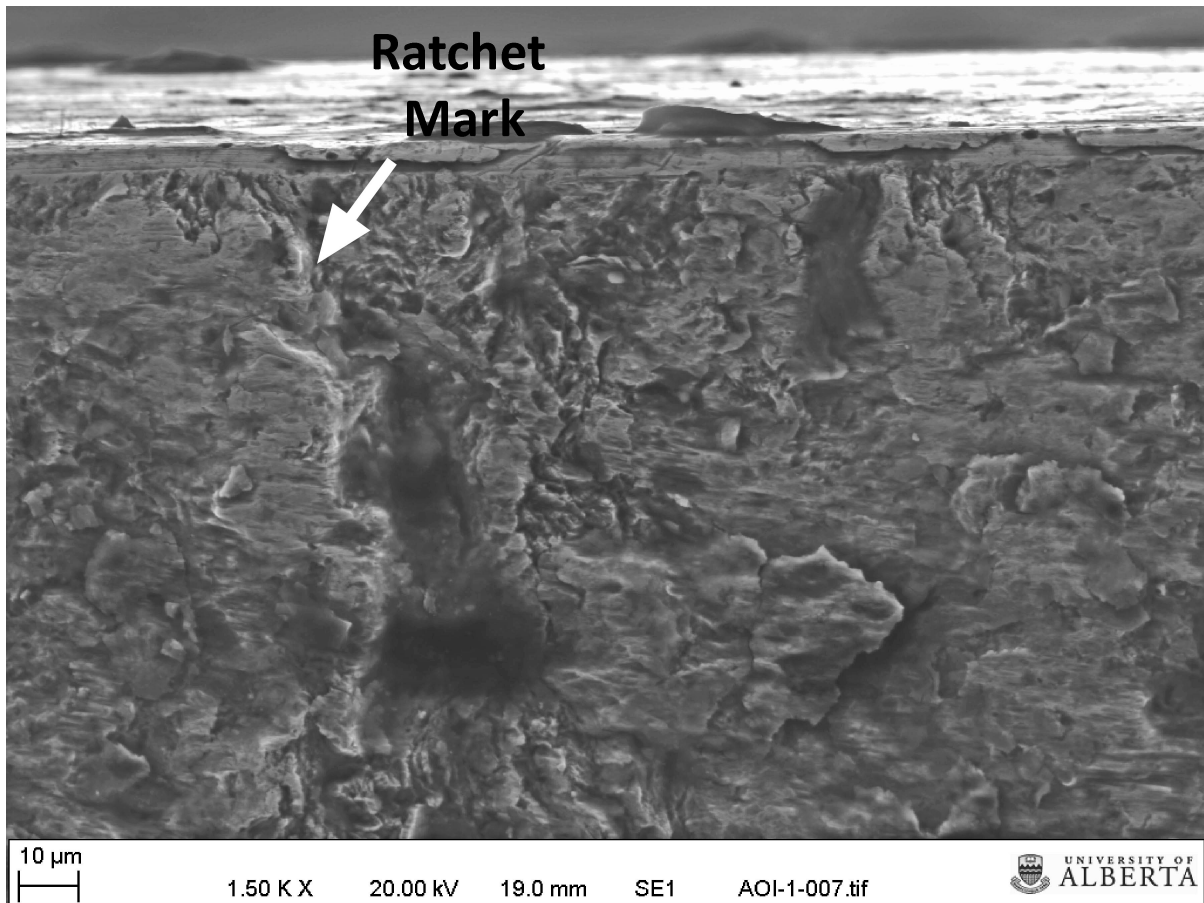


Figure 7.52: B-CO Secondary electron (SE) image showing the presence of a ratchet mark perpendicular to the sample surface.

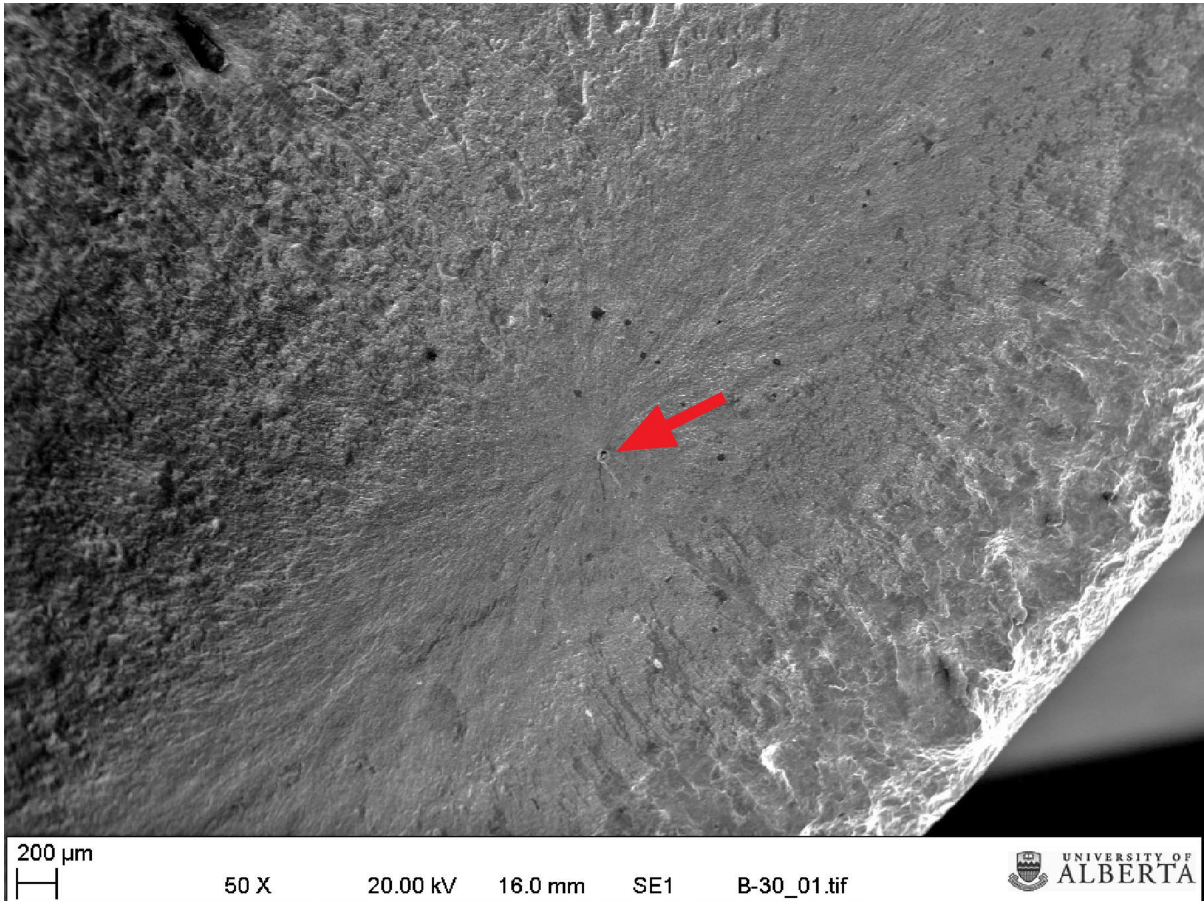


Figure 7.53: B-30 SE image showing fracture initiation at a non metallic inclusion located in the substrate HAZ.

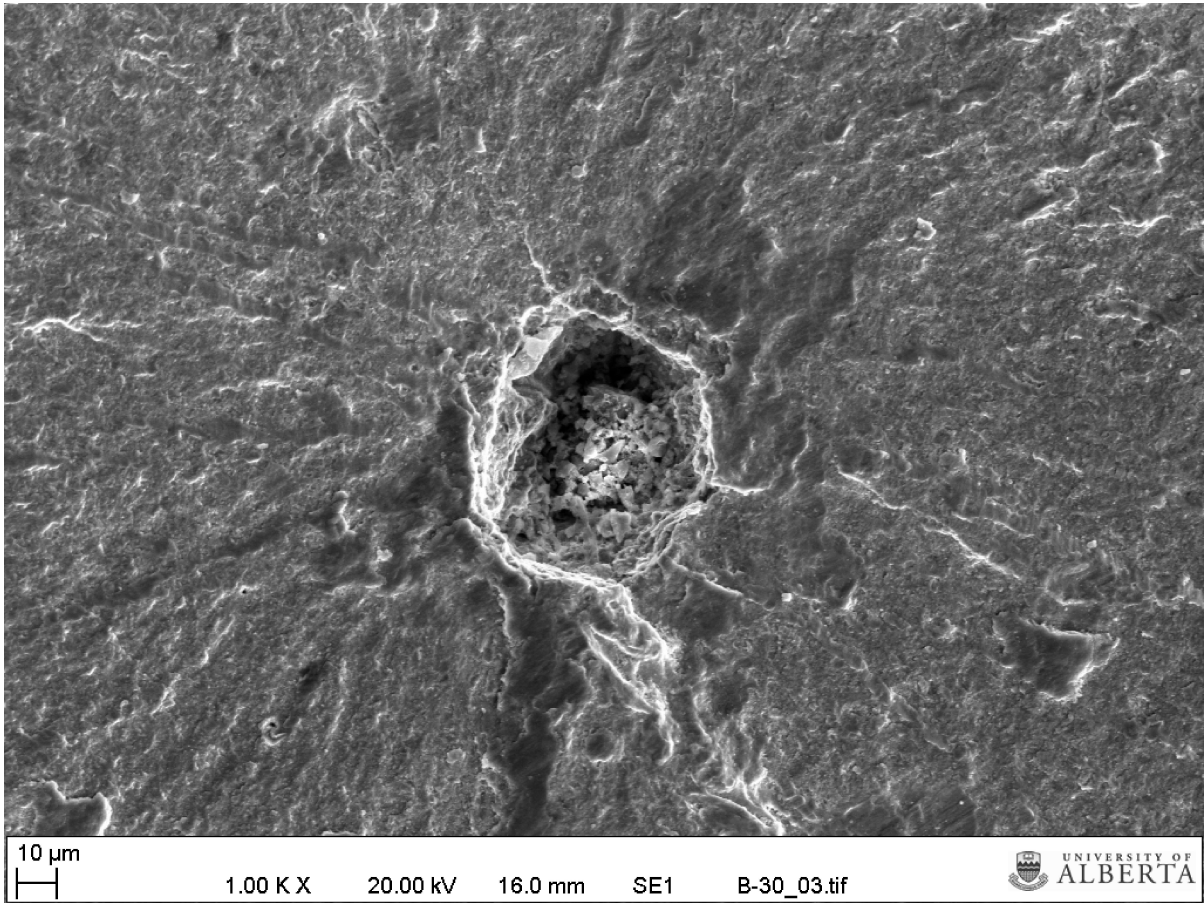
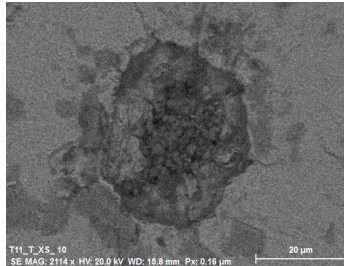


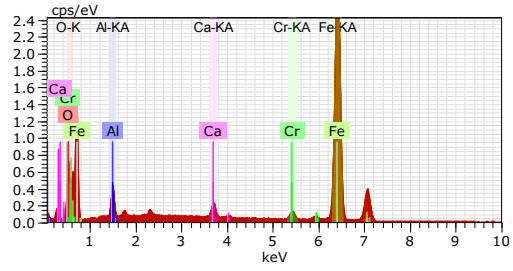
Figure 7.54: B-30 SE image of the non-metallic inclusion

Application Note

Company / Department

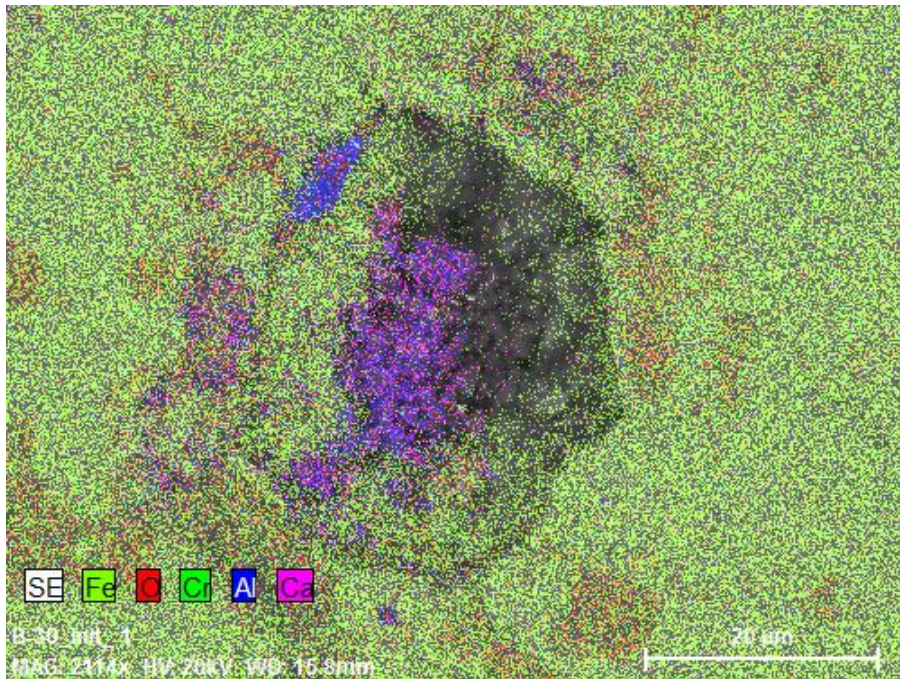


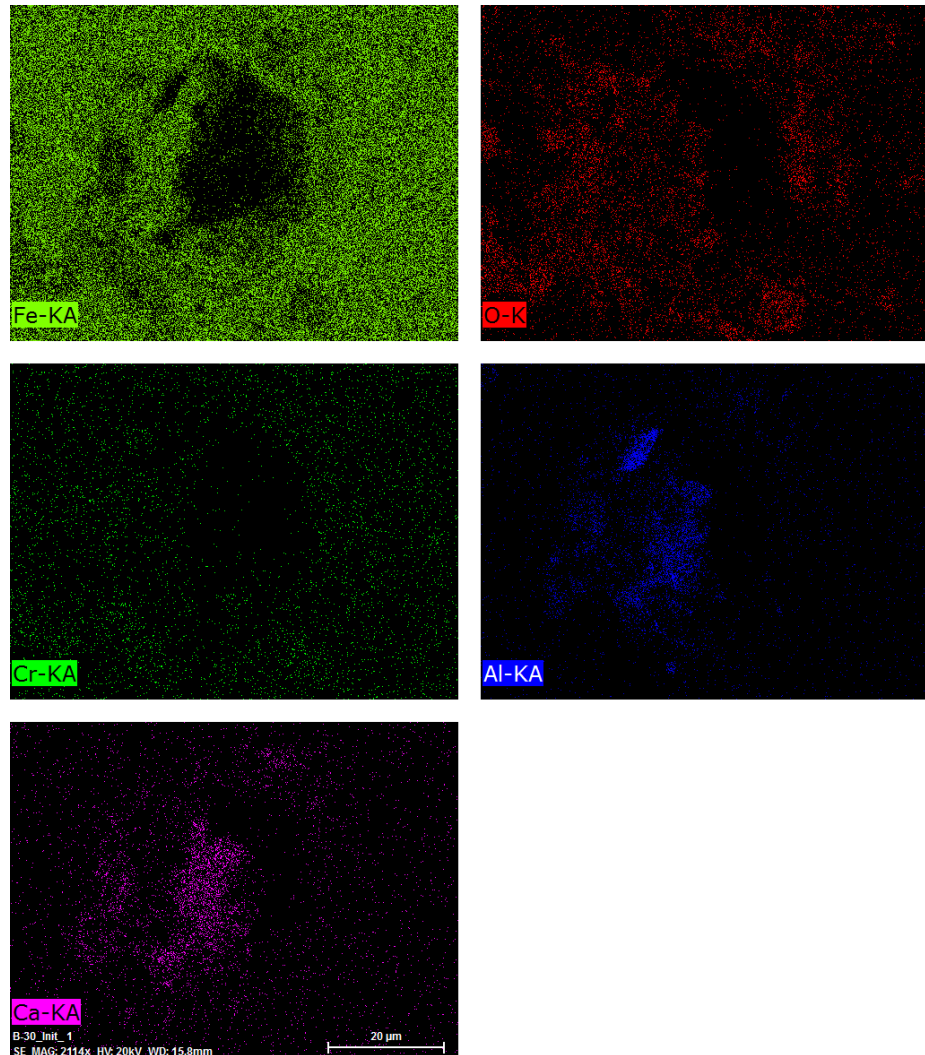
T11_T_XS_10 Date: 8/23/2016 11:59:03 AM
 Image size: 500 x 375
 Mag: 2114.03662 x HV: 20.0 kV



Map Date: 8/23/2016 11:59:37 AM HV: 20.0 kV
 Puls th.: 1.51 kcps

B-30_Init_1 Date: 8/23/2016 11:59:38 AM
 Image size: 500 x 375
 Mag: 2114.03662 x HV: 20.0 kV

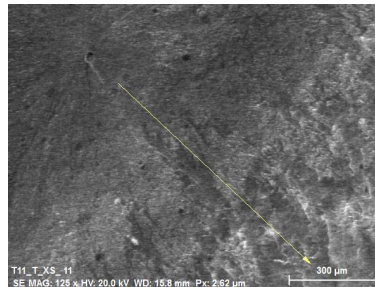




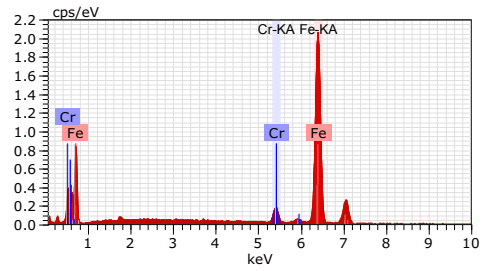
Fe-KA, O-K, Cr-KA, Al-KA, Ca-KA Date:8/23/2016 12:04:32 PM
Image size:500 x 375
Mag:2114.03662x
HV:20.0kV

Application Note

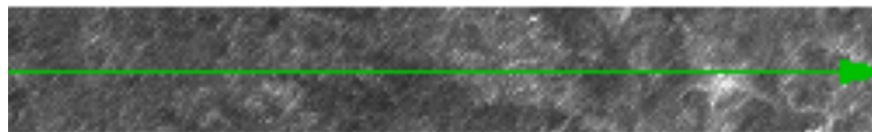
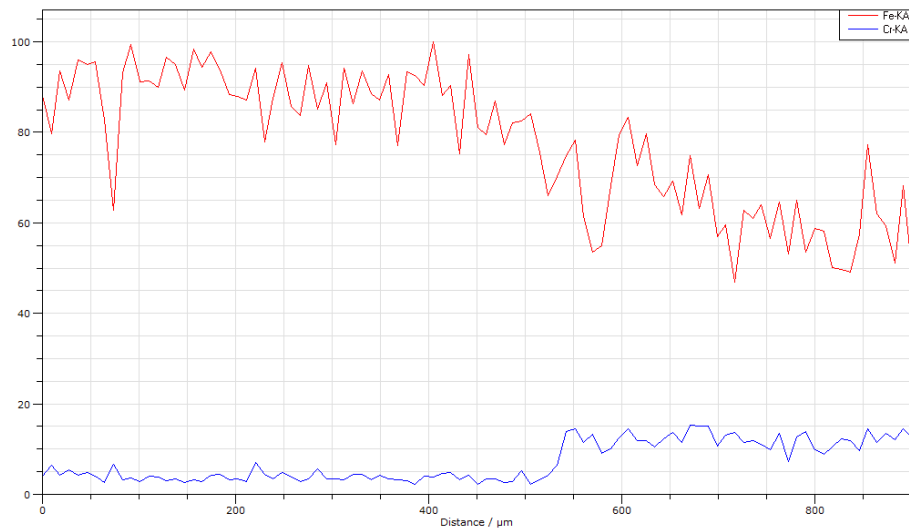
Company / Department



T11_T_XS_11 Date: 8/23/2016 12:12:57
PMImage size: 500 x
375 Magn: 125 HV: 20.0 kV



Scan Date: 8/23/2016 12:13:37 PM HV: 20.0 kV
Puls th.: 0.98 kcps



Fusion_line_1 Date: 8/23/2016 12:17:38 PM Measure time: 2:20 min Start: (145, 104)
End: (209, 242) Length: 011 μm

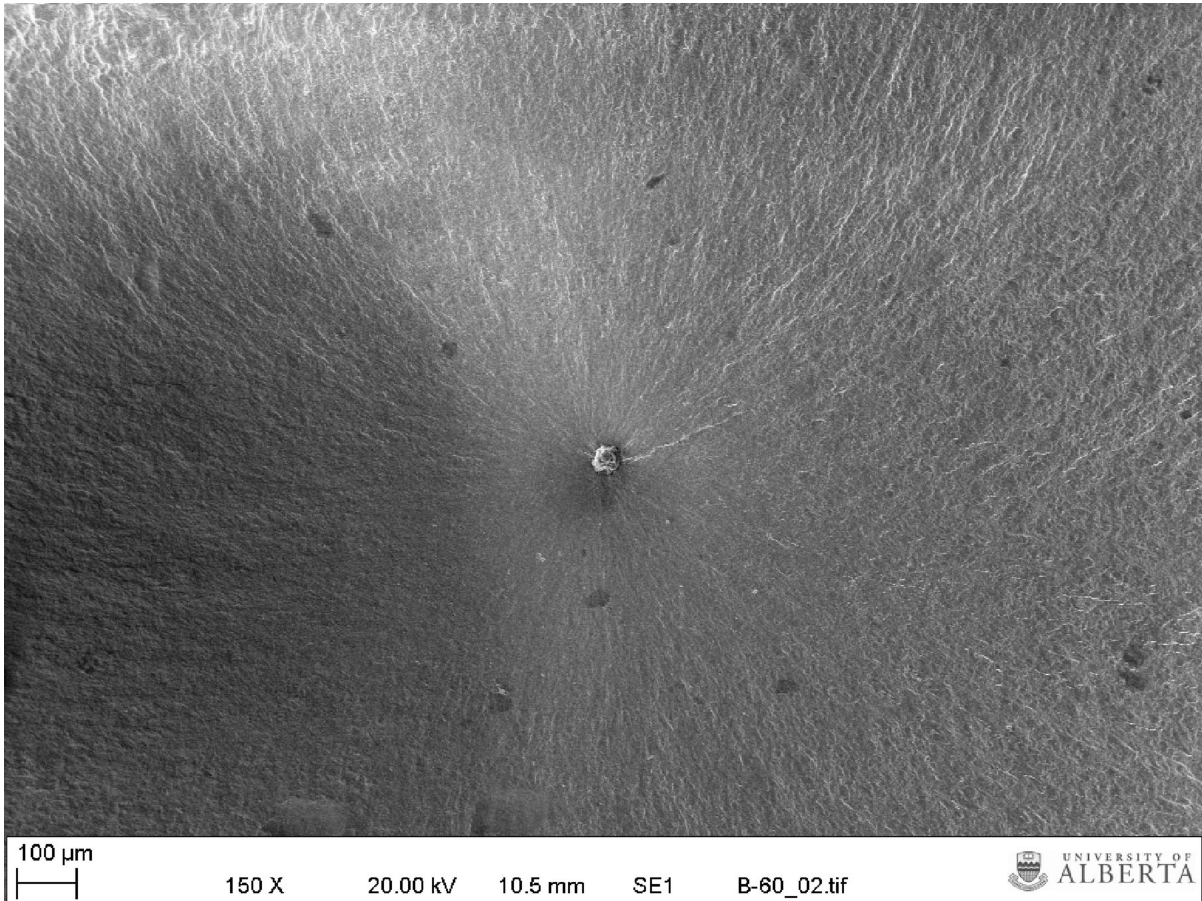


Figure 7.55: B-60 SE image showing fracture initiation at a non metallic inclusion located in the substrate HAZ.

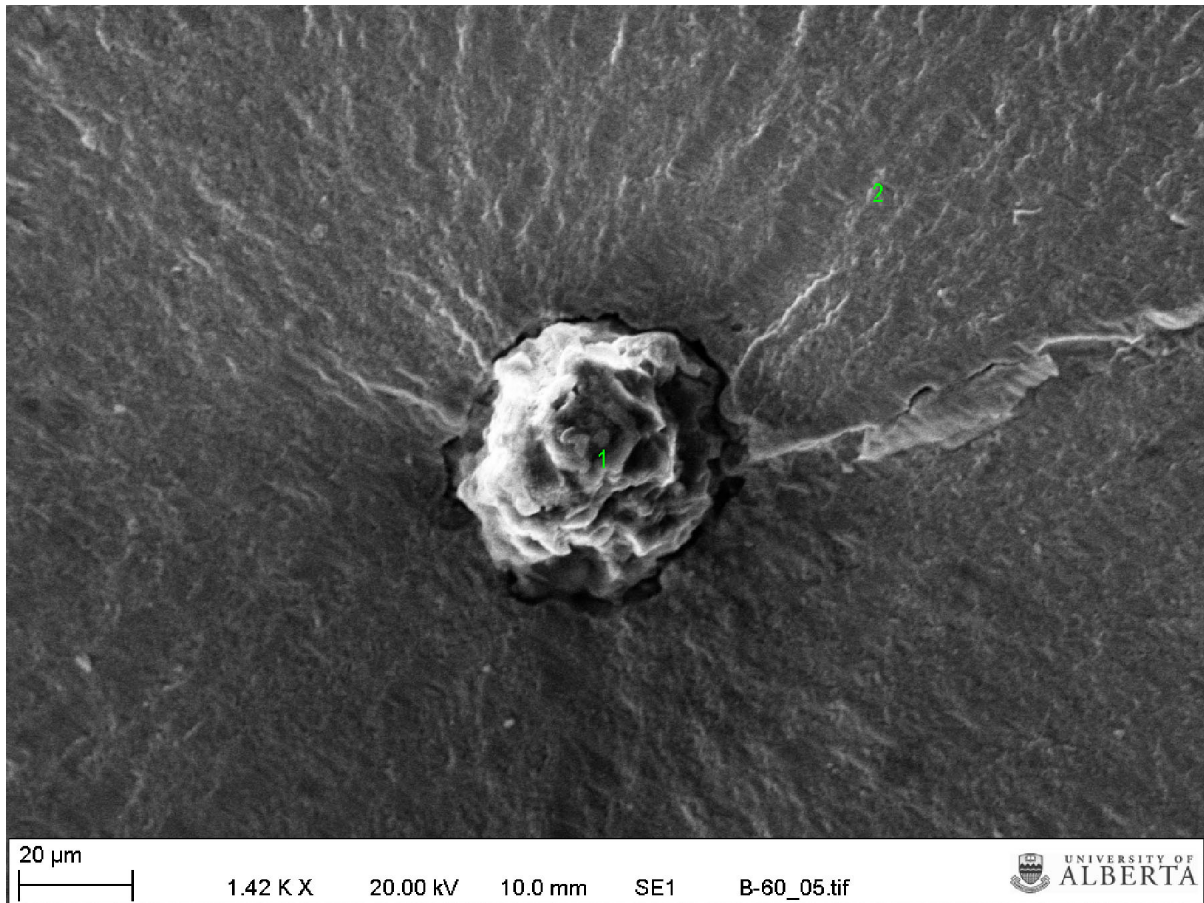
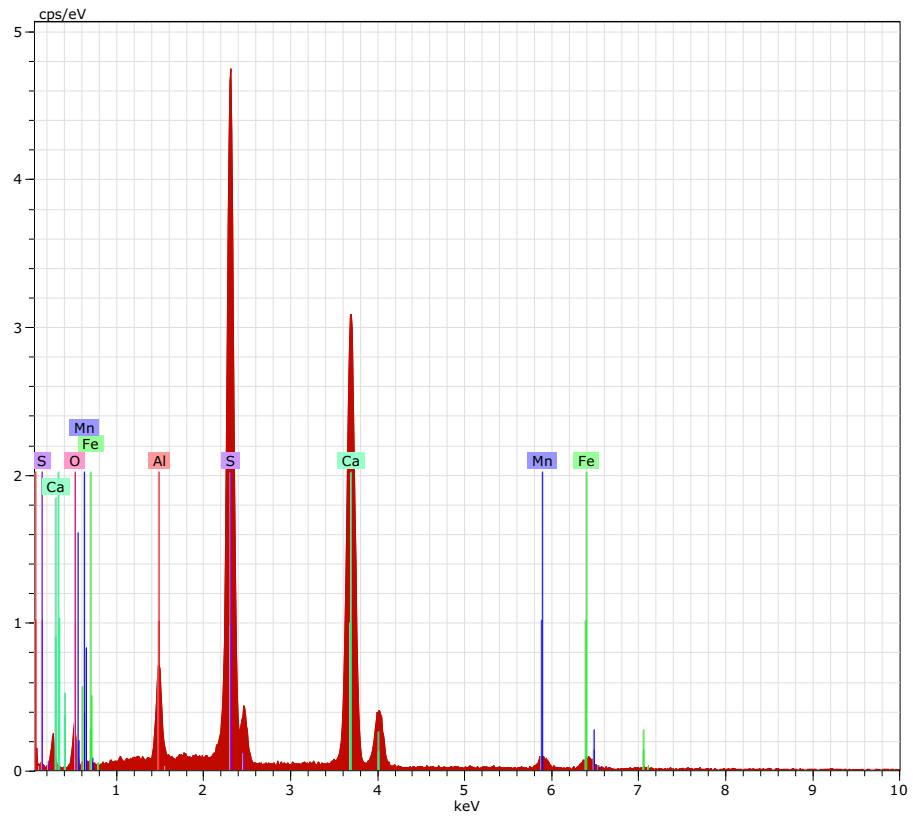


Figure 7.56: B-60 SE image of the inclusion shown in Figure 8.55. EDS analysis was conducted at the locations marked 1 and 2.



EAS SEM Lab

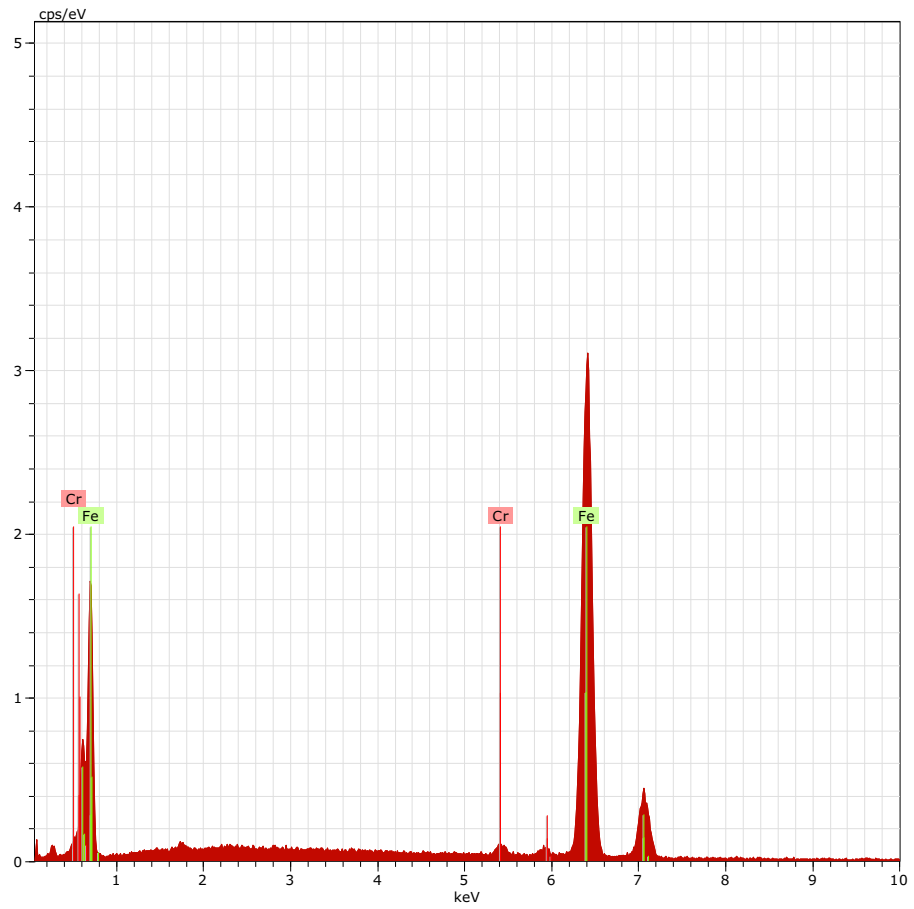


B-60_1 Date:8/19/2016 11:10:50 AM HV:20.0kV Puls th.:1.56kcps

| El | AN | Series | unn. C [wt.%] | norm. C [wt.%] | Atom. C [at.%] | Error (1 Sigma) [wt.%] |
|--------|----|----------|---------------|----------------|----------------|------------------------|
| Ca | 20 | K-series | 41.27 | 43.93 | 32.74 | 1.25 |
| S | 16 | K-series | 27.21 | 28.95 | 26.97 | 1.01 |
| O | 8 | K-series | 16.58 | 17.65 | 32.94 | 3.35 |
| Al | 13 | K-series | 3.70 | 3.94 | 4.36 | 0.22 |
| Fe | 26 | K-series | 2.70 | 2.88 | 1.54 | 0.14 |
| Mn | 25 | K-series | 2.50 | 2.66 | 1.44 | 0.13 |
| Total: | | | 93.96 | 100.00 | 100.00 | |



EAS SEM Lab



B-60_2 Date:8/19/2016 11:15:24 AM HV:20.0kV Puls th.:1.35kcps

| El | AN | Series | unn. C [wt.%] | norm. C [wt.%] | Atom. C [at.%] | Error (1 Sigma) [wt.%] |
|--------|----|----------|---------------|----------------|----------------|------------------------|
| Fe | 26 | K-series | 96.45 | 98.93 | 98.85 | 2.62 |
| Cr | 24 | K-series | 1.05 | 1.07 | 1.15 | 0.07 |
| Total: | | | 97.50 | 100.00 | 100.00 | |

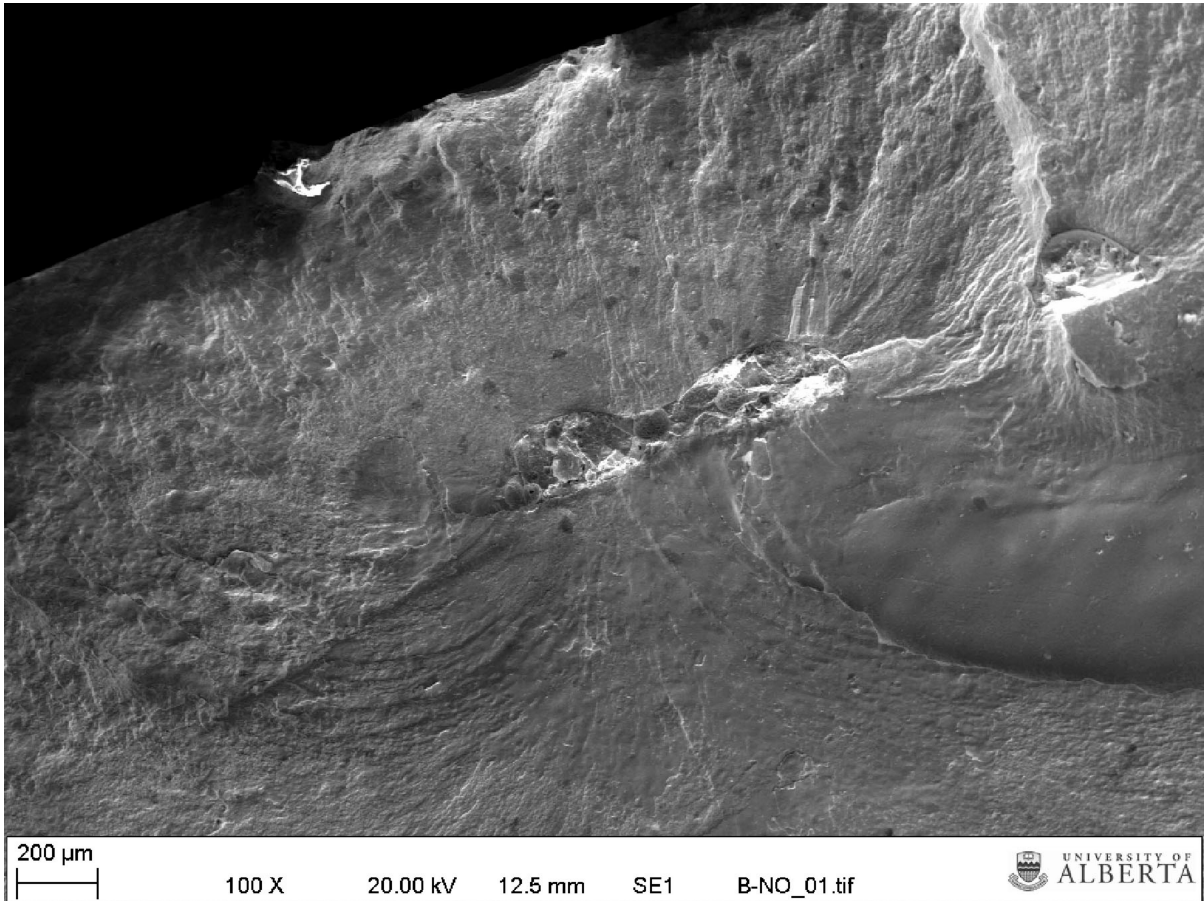


Figure 7.57: B-NO SE image showing fracture initiation at a non metallic inclusion located at the fusion line.

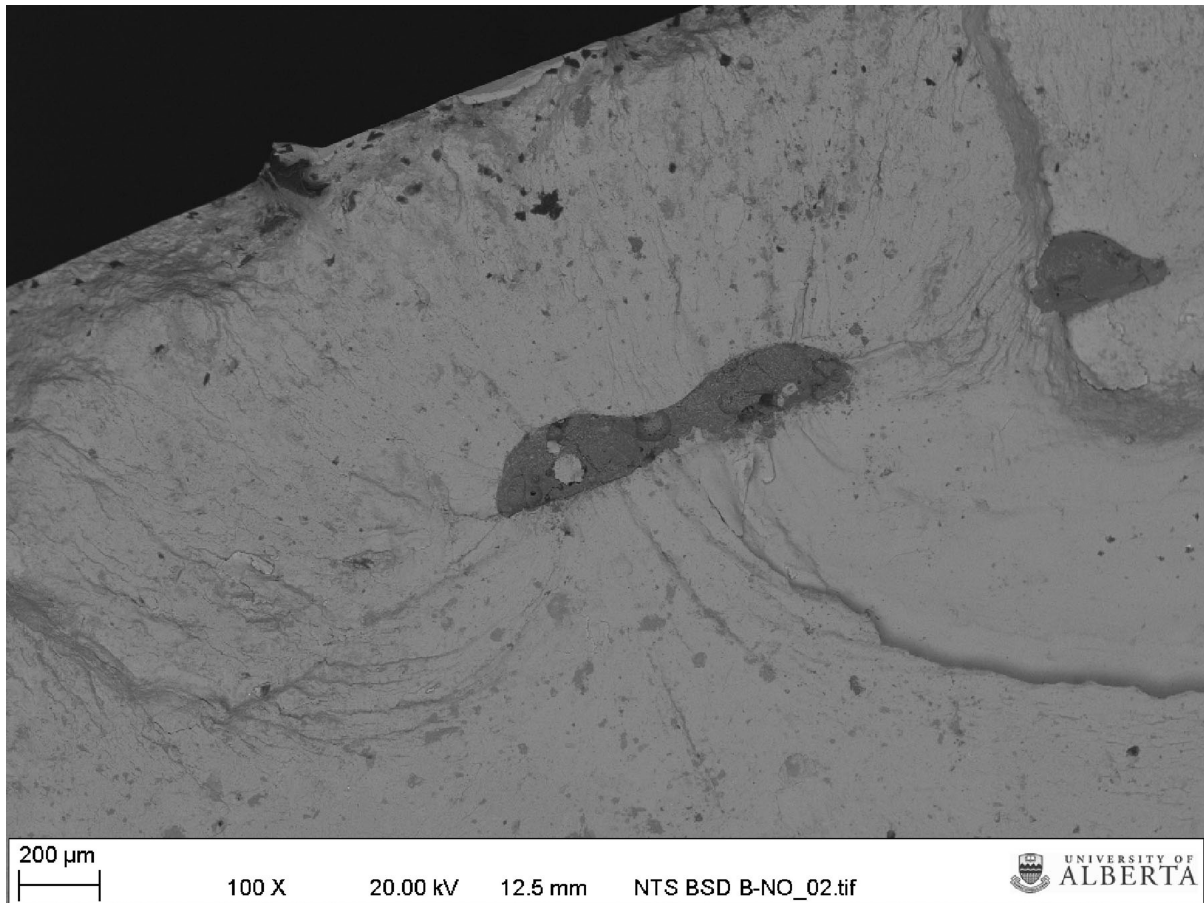


Figure 7.58: B-NO Back Scatter Electron (BSE) image showing fracture initiation at a non metallic inclusion located at the fusion line.

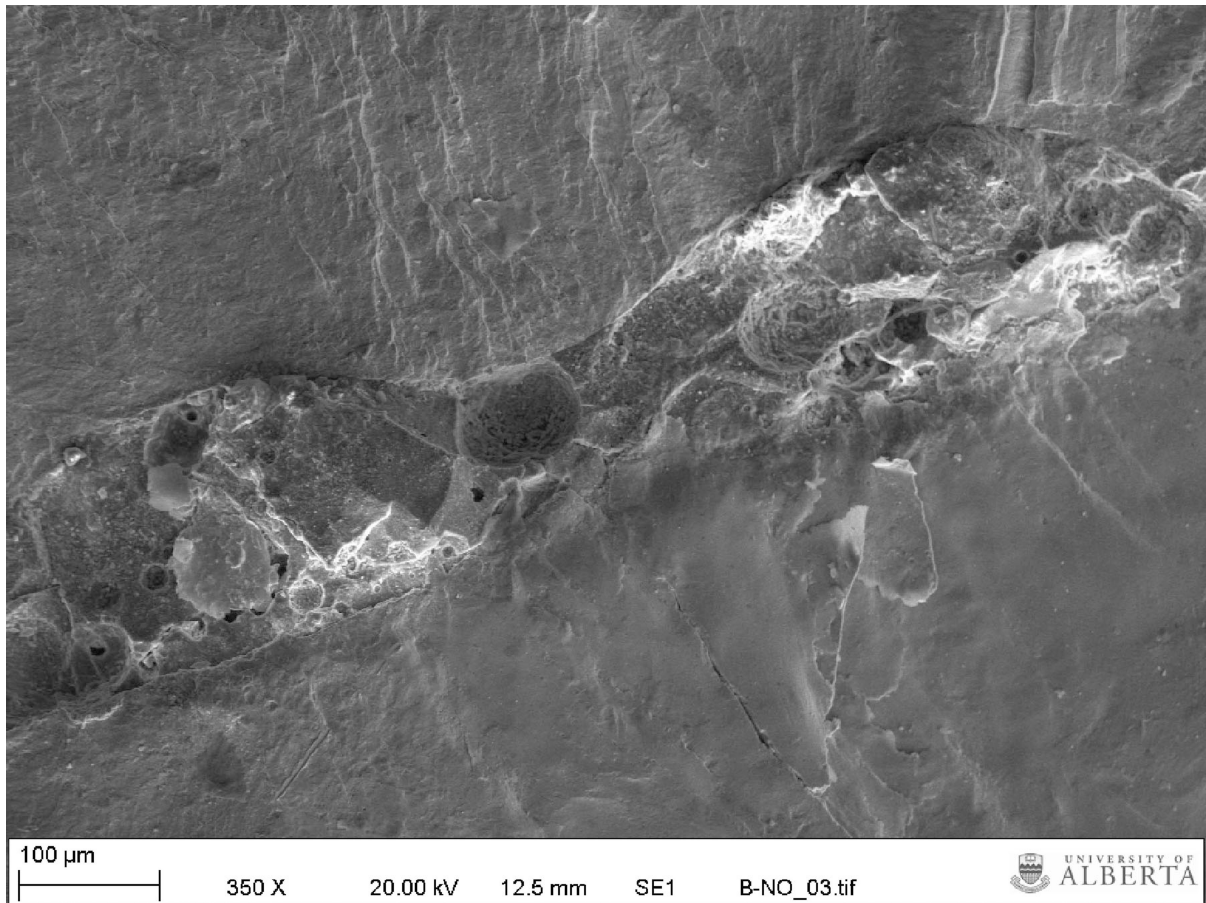


Figure 7.59: B-NO high magnification SE image of the fusion line inclusion.

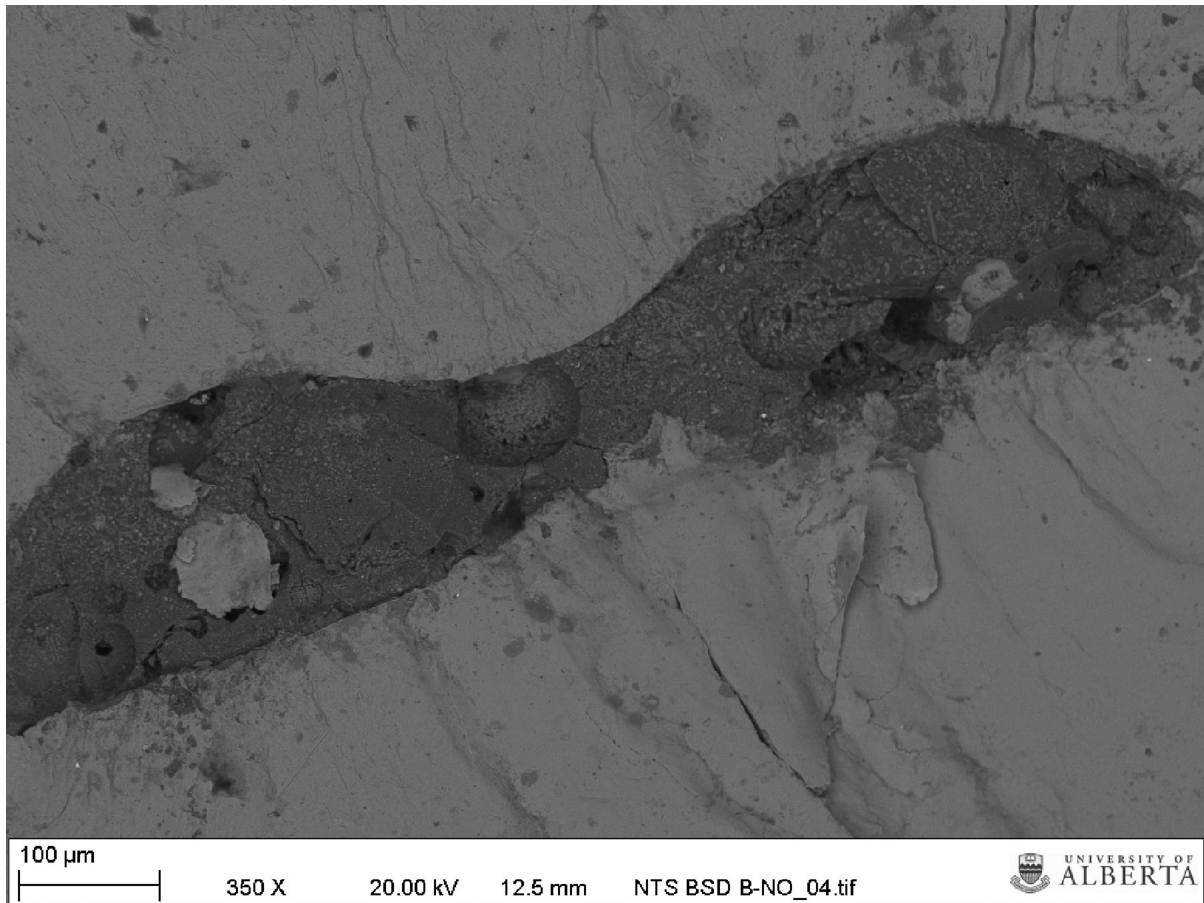
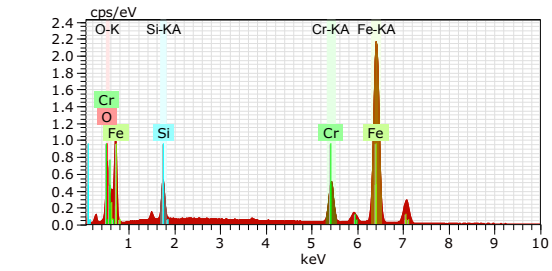
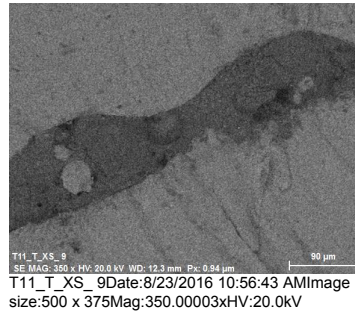


Figure 7.60: B-NO high magnification BSE image of the fusion line inclusion.

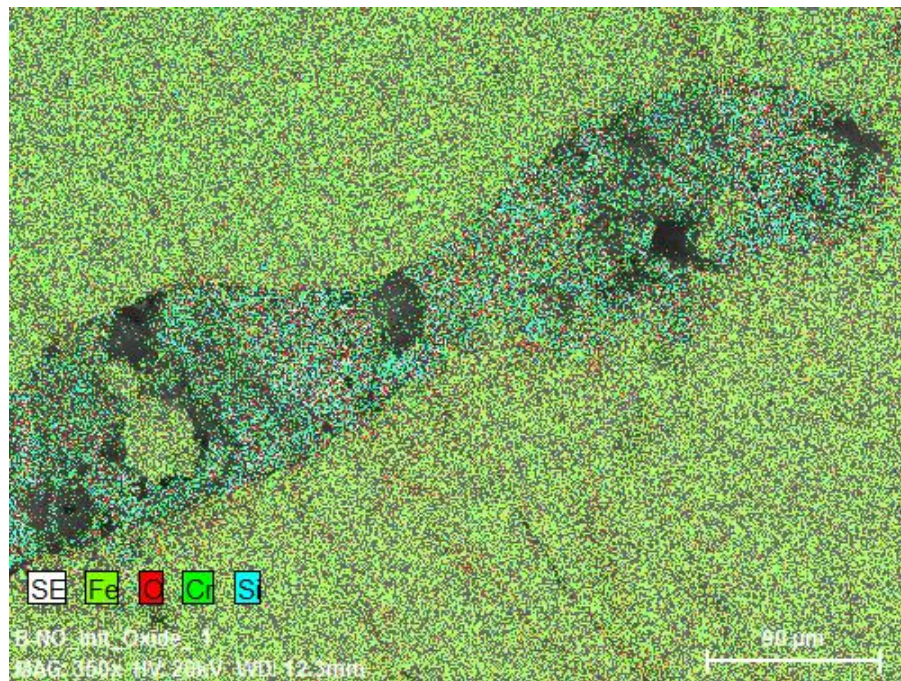
Application Note

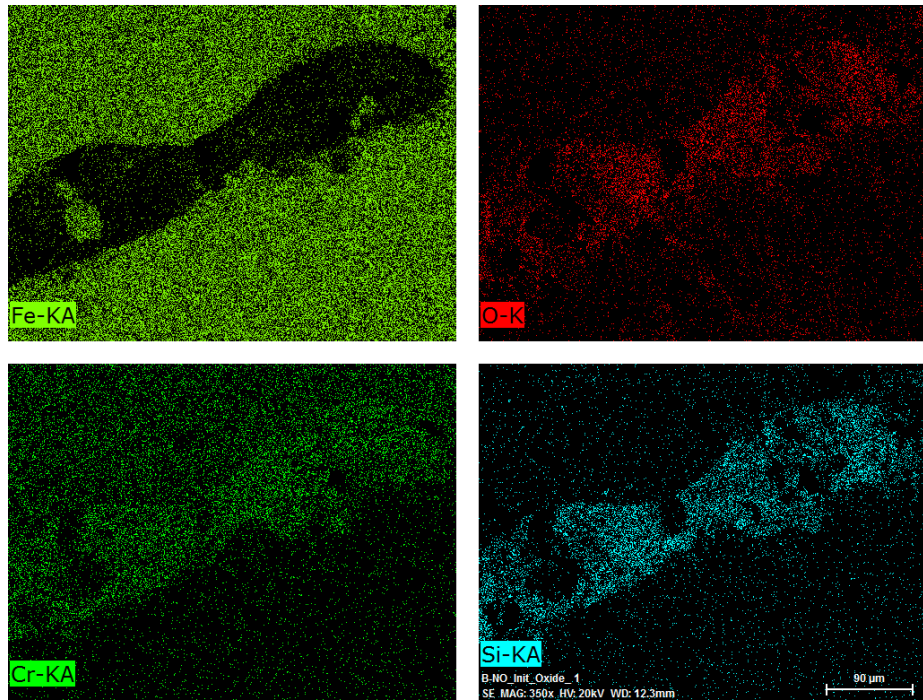
Company / Department



Map Date: 8/23/2016 10:57:32 AM HV: 20.0kV
Puls th.: 1.27kcps

B-NO_Init_Oxide_1 Date: 8/23/2016 10:57:33 AM Image size: 500 x 375
Mag: 350.00003x HV: 20.0kV





Fe-KA, O-K, Cr-KA, Si-KA Date: 8/23/2016 11:04:51 AM
Image size: 500 x 375
Mag: 350.00003x
HV: 20.0kV

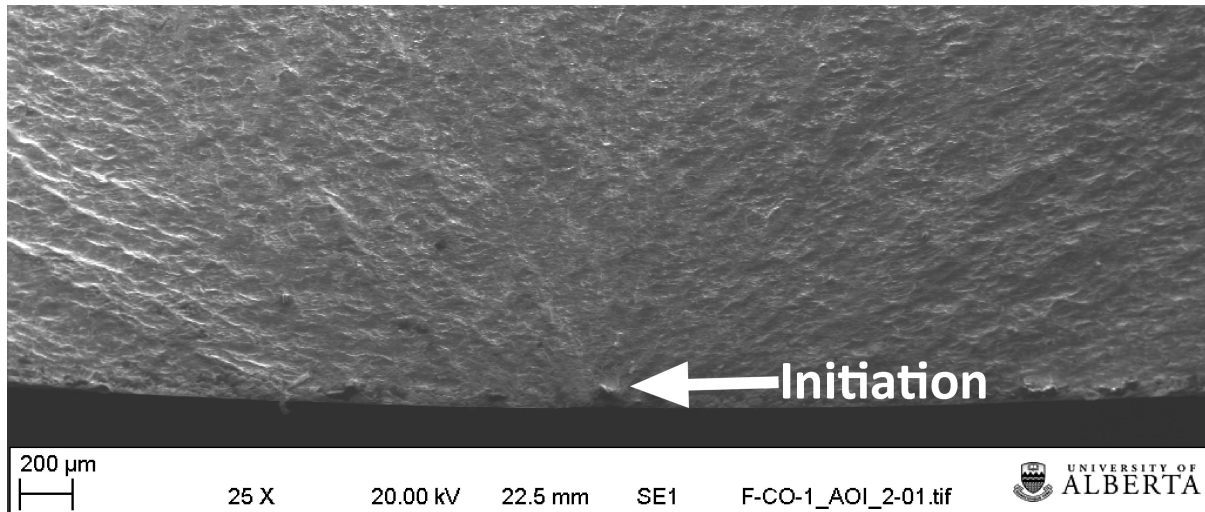
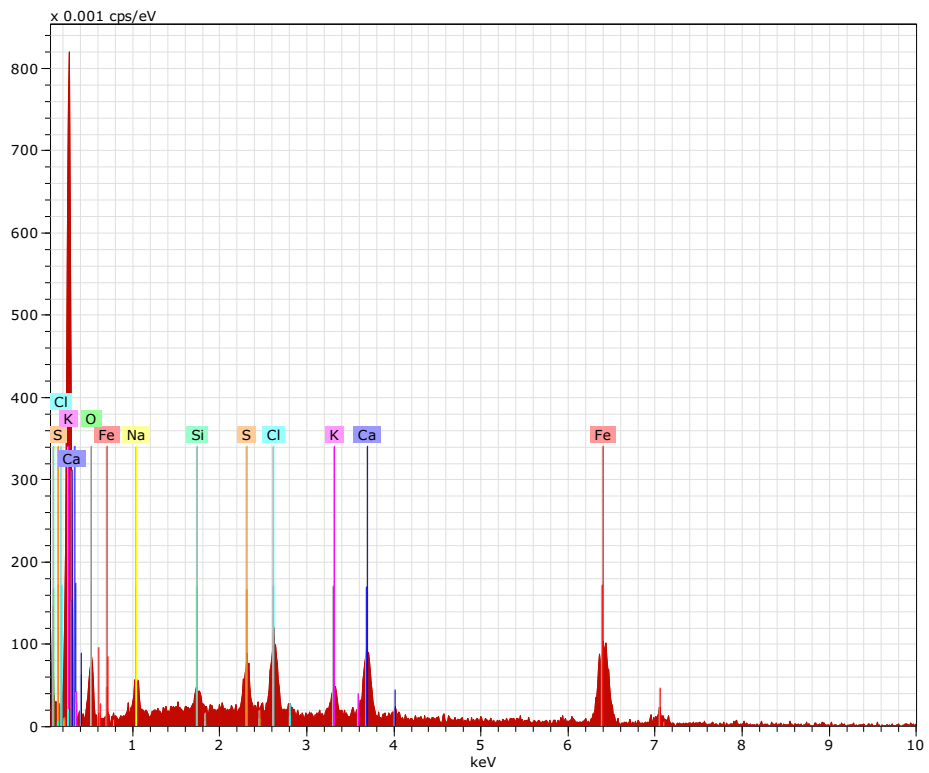


Figure 7.61: F-CO SE image of the initiation location shown in Figure 8.46. Initiation occurred at a near surface non metallic inclusion.



EAS SEM Lab



F-CO_AOI_2-1 Date:2/19/2017 5:28:12 PM HV:20.0kV Puls th.:0.36kcps

| El | AN | Series | unn. C [wt.%] | norm. C [wt.%] | Atom. C [at.%] | Error (1 Sigma) [wt.%] |
|--------|----|----------|---------------|----------------|----------------|------------------------|
| Fe | 26 | K-series | 13.72 | 39.48 | 21.25 | 0.52 |
| O | 8 | K-series | 8.66 | 24.93 | 46.84 | 2.37 |
| Ca | 20 | K-series | 4.24 | 12.20 | 9.15 | 0.21 |
| Cl | 17 | K-series | 2.79 | 8.04 | 6.82 | 0.16 |
| Na | 11 | K-series | 1.97 | 5.66 | 7.41 | 0.22 |
| K | 19 | K-series | 1.47 | 4.24 | 3.26 | 0.11 |
| S | 16 | K-series | 1.44 | 4.15 | 3.89 | 0.11 |
| Si | 14 | K-series | 0.44 | 1.28 | 1.37 | 0.06 |
| Total: | | | 34.74 | 100.00 | 100.00 | |

Appendix D – Residual Stress Data

8.1 Introduction

Strain data acquired during hole drilling was processed using the computation method for non-uniform stresses in a thick work piece as outlined in ASTM E837-2008 [31]. Due to the iterative nature of the calculations, a MatLab script was written to perform the calculations. The script is presented in Appendix 10.2; all raw data and computational outputs are provided in the Residual Stress Data section below. For each of the residual stress samples the strain gauge rosette was installed so that the reference direction corresponded to the longitudinal axis of the part as shown in Figure 9.62.



Figure 8.62: RS-30 strain gauge rosette installation

8.2 Residual Stress Data

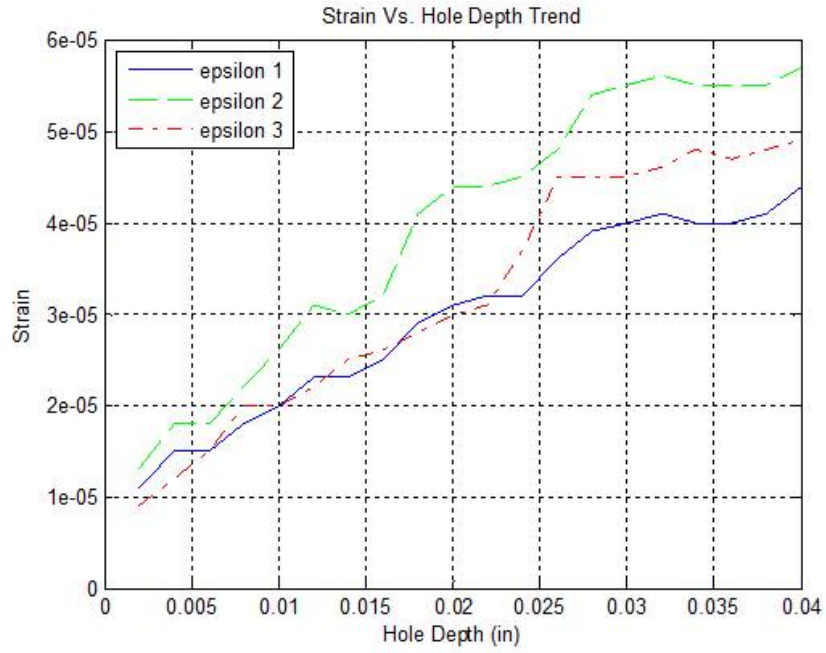


Figure 8.63: R-CO measured strain Vs. Depth

| Hole Depth (in) | Strain 1 | Strain 2 | Strain 3 |
|--------------------|---------------------|-------------------|-----------------------|
| | Reference Direction | 45 deg. frm. Ref. | Perpendicular to Ref. |
| 0.0020 | 1.1000e-05 | 1.3000e-05 | 9.0000e-06 |
| 0.0040 | 1.5000e-05 | 1.8000e-05 | 1.2000e-05 |
| 0.0060 | 1.5000e-05 | 1.8000e-05 | 1.5000e-05 |
| 0.0080 | 1.8000e-05 | 2.2000e-05 | 2.0000e-05 |
| 0.0100 | 2.0000e-05 | 2.6000e-05 | 2.0000e-05 |
| 0.0120 | 2.3000e-05 | 3.1000e-05 | 2.2000e-05 |
| 0.0140 | 2.3000e-05 | 3.0000e-05 | 2.5000e-05 |
| 0.0160 | 2.5000e-05 | 3.2000e-05 | 2.6000e-05 |
| 0.0180 | 2.9000e-05 | 4.1000e-05 | 2.8000e-05 |
| 0.0200 | 3.1000e-05 | 4.4000e-05 | 3.0000e-05 |
| 0.0220 | 3.2000e-05 | 4.4000e-05 | 3.1000e-05 |
| 0.0240 | 3.2000e-05 | 4.5000e-05 | 3.7000e-05 |
| 0.0260 | 3.6000e-05 | 4.8000e-05 | 4.5000e-05 |
| 0.0280 | 3.9000e-05 | 5.4000e-05 | 4.5000e-05 |
| 0.0300 | 4.0000e-05 | 5.5000e-05 | 4.5000e-05 |
| 0.0320 | 4.1000e-05 | 5.6000e-05 | 4.6000e-05 |
| 0.0340 | 4.0000e-05 | 5.5000e-05 | 4.8000e-05 |
| 0.0360 | 4.0000e-05 | 5.5000e-05 | 4.7000e-05 |
| 0.0380 | 4.1000e-05 | 5.5000e-05 | 4.8000e-05 |
| 0.0400 | 4.4000e-05 | 5.7000e-05 | 4.9000e-05 |

Figure 8.64: RS-CO tabulated strain data

| Hole Depth (in) | Combined Strain p | Combined Strain q | Combined Strain t | Stress P (psi) | Stress Q (psi) | Stress T (psi) |
|-----------------|-------------------|-------------------|-------------------|----------------|----------------|----------------|
| 0.0020 | 1.0000e-05 | -1.0000e-06 | -3.0000e-06 | -3.2561e+04 | 858.9536 | 3.6180e+03 |
| 0.0040 | 1.3500e-05 | -1.5000e-06 | -4.5000e-06 | -5.5427e+03 | 25.5235 | 88.0716 |
| 0.0060 | 1.5000e-05 | 0 | -3.0000e-06 | 1.1191e+03 | -1.1103e+03 | 766.7730 |
| 0.0080 | 1.9000e-05 | 1.0000e-06 | -3.0000e-06 | -5.0509e+03 | -793.0404 | 1.9663e+03 |
| 0.0100 | 2.0000e-05 | 0 | -6.0000e-06 | 1.0049e+03 | 566.6948 | 3.0113e+03 |
| 0.0120 | 2.2500e-05 | -5.0000e-07 | -8.5000e-06 | -2.1515e+03 | 380.1408 | 2.1356e+03 |
| 0.0140 | 2.4000e-05 | 1.0000e-06 | -6.0000e-06 | -532.0586 | -70.6085 | 1.6631e+03 |
| 0.0160 | 2.5500e-05 | 5.0000e-07 | -6.5000e-06 | -1.0770e+03 | 1.1514e+03 | 4.0849e+03 |
| 0.0180 | 2.8500e-05 | -5.0000e-07 | -1.2500e-05 | -6.0227e+03 | 661.1810 | 2.3428e+03 |
| 0.0200 | 3.0500e-05 | -5.0000e-07 | -1.3500e-05 | -2.7004e+03 | -591.9416 | -1.0293e+03 |
| 0.0220 | 3.1500e-05 | -5.0000e-07 | -1.2500e-05 | -5.1474e+03 | -2.7900e+03 | -4.3715e+03 |
| 0.0240 | 3.4500e-05 | 2.5000e-06 | -1.0500e-05 | -1.8093e+04 | -4.5742e+03 | -4.9721e+03 |
| 0.0260 | 4.0500e-05 | 4.5000e-06 | -7.5000e-06 | 2.3450e+03 | -2.4272e+03 | -1.5249e+03 |
| 0.0280 | 4.2000e-05 | 3.0000e-06 | -1.2000e-05 | -1.2938e+04 | 1.4248e+03 | 3.2837e+03 |
| 0.0300 | 4.2500e-05 | 2.5000e-06 | -1.2500e-05 | -3.6348e+03 | 2.0706e+03 | 3.1379e+03 |
| 0.0320 | 4.3500e-05 | 2.5000e-06 | -1.2500e-05 | 3.5526e+03 | 66.3528 | -75.0741 |
| 0.0340 | 4.4000e-05 | 4.0000e-06 | -1.1000e-05 | 7.5841e+03 | -1.5903e+03 | -2.8165e+03 |
| 0.0360 | 4.3500e-05 | 3.5000e-06 | -1.1500e-05 | 5.5418e+03 | -685.9370 | -3.1183e+03 |
| 0.0380 | 4.4500e-05 | 3.5000e-06 | -1.0500e-05 | -8.9628e+03 | 1.6499e+03 | -1.8820e+03 |
| 0.0400 | 4.6500e-05 | 2.5000e-06 | -1.0500e-05 | -2.8783e+04 | 4.5136e+03 | -174.2092 |

Figure 8.65: RS-CO combination strain data

| | Standard Error Estimate |
|-------------------|-------------------------|
| Combined Strain p | 5.1471e-13 |
| Combined Strain q | 3.2941e-13 |
| Combined Strain t | 1.4529e-12 |

Figure 8.66: RS-CO estimated standard error in the combined strain calculations

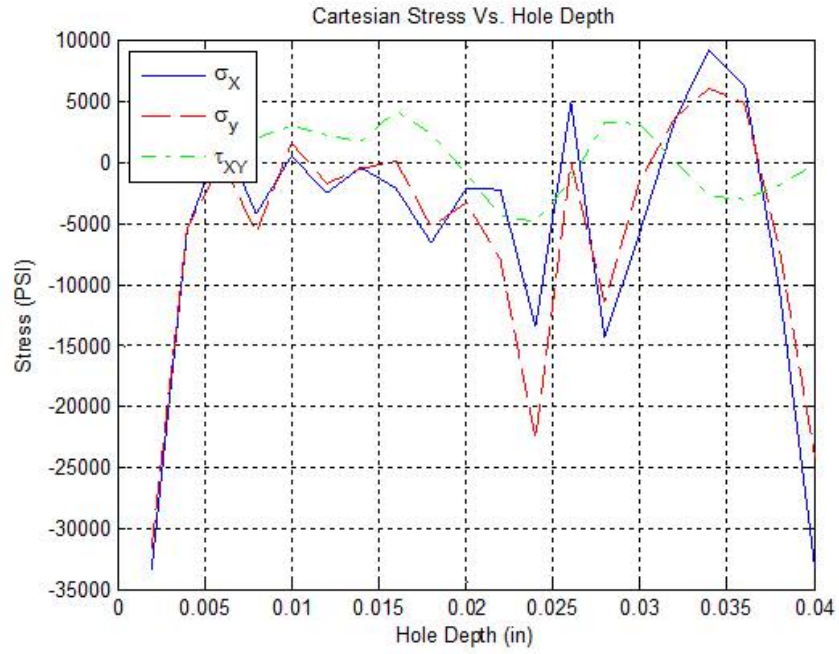


Figure 8.67: RS-CO Cartesian stresses versus depth. The X-direction corresponds to the longitudinal axis of the sample

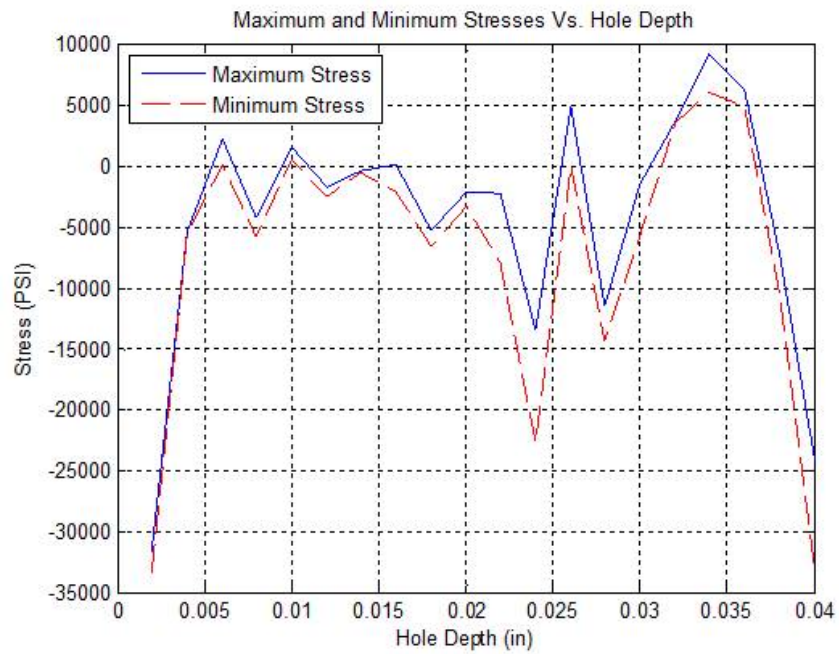


Figure 8.68: RS-CO magnitude of the maximum and minimum stresses as a function of depth below the surface

| Hole Depth (in) | Maximum Stress (psi) | Principal Direction (Deg.) Meas. Frm. Reference Dir. |
|--------------------|-------------------------|---|
| 0.0020 | -3.1702e+04 | -51.6778 |
| 0.0040 | -5.5172e+03 | -53.0809 |
| 0.0060 | 2.2294e+03 | -17.3139 |
| 0.0080 | -4.2578e+03 | -34.0177 |
| 0.0100 | 1.5716e+03 | -50.3289 |
| 0.0120 | -1.7713e+03 | -50.0466 |
| 0.0140 | -461.4501 | -43.7845 |
| 0.0160 | 74.3615 | -52.8704 |
| 0.0180 | -5.3615e+03 | -52.8799 |
| 0.0200 | -2.1085e+03 | 30.0485 |
| 0.0220 | -2.3574e+03 | 28.7266 |
| 0.0240 | -1.3518e+04 | 23.6934 |
| 0.0260 | 4.7722e+03 | 16.0692 |
| 0.0280 | -1.1514e+04 | -56.7279 |
| 0.0300 | -1.5642e+03 | -61.7097 |
| 0.0320 | 3.6190e+03 | 65.7356 |
| 0.0340 | 9.1745e+03 | 30.2743 |
| 0.0360 | 6.2278e+03 | 38.7970 |
| 0.0380 | -7.3130e+03 | 65.6196 |
| 0.0400 | -2.4269e+04 | 88.8948 |

Figure 8.69: RS-CO direction in which the maximum stresses act relative to the longitudinal axis of the sample (reference direction)

| Hole Depth (in) | Minimum Stress (psi) | Principal Direction (Deg.) Meas. Perp. to Reference Dir. |
|--------------------|-------------------------|---|
| 0.0020 | -3.3420e+04 | -51.6778 |
| 0.0040 | -5.5682e+03 | -53.0809 |
| 0.0060 | 8.7306 | -17.3139 |
| 0.0080 | -5.8439e+03 | -34.0177 |
| 0.0100 | 438.1755 | -50.3289 |
| 0.0120 | -2.5316e+03 | -50.0466 |
| 0.0140 | -602.6671 | -43.7845 |
| 0.0160 | -2.2284e+03 | -52.8704 |
| 0.0180 | -6.6838e+03 | -52.8799 |
| 0.0200 | -3.2924e+03 | 30.0485 |
| 0.0220 | -7.9374e+03 | 28.7266 |
| 0.0240 | -2.2667e+04 | 23.6934 |
| 0.0260 | -82.2019 | 16.0692 |
| 0.0280 | -1.4363e+04 | -56.7279 |
| 0.0300 | -5.7054e+03 | -61.7097 |
| 0.0320 | 3.4863e+03 | 65.7356 |
| 0.0340 | 5.9938e+03 | 30.2743 |
| 0.0360 | 4.8559e+03 | 38.7970 |
| 0.0380 | -1.0613e+04 | 65.6196 |
| 0.0400 | -3.3296e+04 | 88.8948 |

Figure 8.70: RS-CO direction in which the minimum stresses act relative to the longitudinal axis of the sample (reference direction)

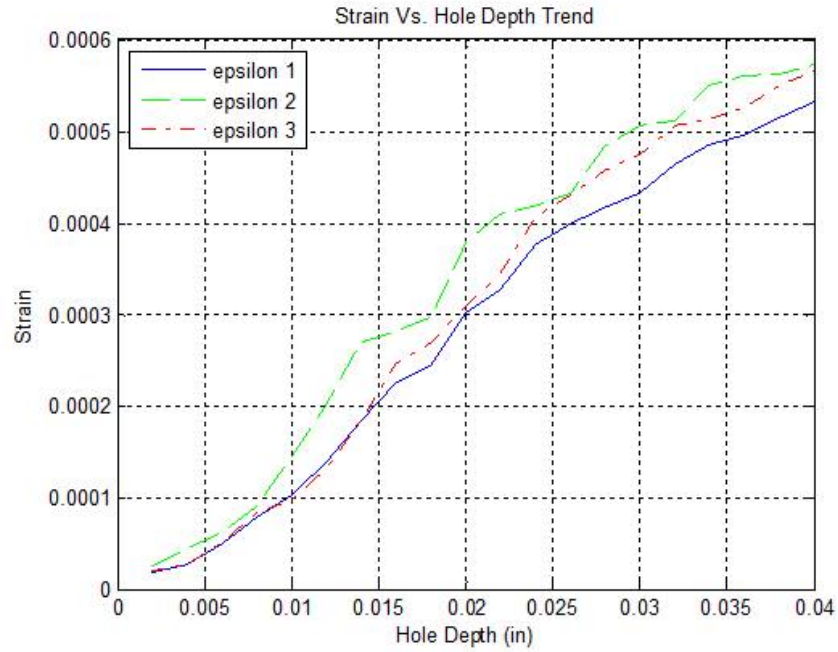


Figure 8.71: R-NO measured strain Vs. Depth

| Hole Depth (in) | Strain 1 Reference Direction | Strain 2 45 deg. frm. Ref. | Strain 3 Perpendicular to Ref. |
|-----------------|------------------------------|----------------------------|--------------------------------|
| 0.0020 | 1.8000e-05 | 2.5000e-05 | 2.0000e-05 |
| 0.0040 | 2.8000e-05 | 4.5000e-05 | 2.7000e-05 |
| 0.0060 | 5.0000e-05 | 6.3000e-05 | 5.1000e-05 |
| 0.0080 | 7.8000e-05 | 9.0000e-05 | 8.3000e-05 |
| 0.0100 | 1.0200e-04 | 1.4500e-04 | 9.7000e-05 |
| 0.0120 | 1.4000e-04 | 2.0300e-04 | 1.3300e-04 |
| 0.0140 | 1.8400e-04 | 2.6900e-04 | 1.8400e-04 |
| 0.0160 | 2.2600e-04 | 2.8100e-04 | 2.4600e-04 |
| 0.0180 | 2.4500e-04 | 2.9700e-04 | 2.7000e-04 |
| 0.0200 | 3.0200e-04 | 3.7900e-04 | 3.0900e-04 |
| 0.0220 | 3.2700e-04 | 4.1000e-04 | 3.4500e-04 |
| 0.0240 | 3.7600e-04 | 4.1800e-04 | 4.0600e-04 |
| 0.0260 | 4.0000e-04 | 4.3200e-04 | 4.3100e-04 |
| 0.0280 | 4.1700e-04 | 4.8400e-04 | 4.5700e-04 |
| 0.0300 | 4.3300e-04 | 5.0600e-04 | 4.7400e-04 |
| 0.0320 | 4.6400e-04 | 5.1100e-04 | 5.0600e-04 |
| 0.0340 | 4.8500e-04 | 5.5000e-04 | 5.1300e-04 |
| 0.0360 | 4.9500e-04 | 5.6000e-04 | 5.2500e-04 |
| 0.0380 | 5.1500e-04 | 5.6300e-04 | 5.5000e-04 |
| 0.0400 | 5.3200e-04 | 5.7200e-04 | 5.6500e-04 |

Figure 8.72: RS-NO tabulated strain data

| Hole Depth (in) | Combined Strain p | Combined Strain q | Combined Strain t | Stress P (psi) | Stress Q (psi) | Stress T (psi) |
|-----------------|-------------------|-------------------|-------------------|----------------|----------------|----------------|
| 0.0020 | 1.9000e-05 | 1.0000e-06 | -6.0000e-06 | -4.3607e+04 | 2.1215e+03 | 1.5038e+04 |
| 0.0040 | 2.7500e-05 | -5.0000e-07 | -1.7500e-05 | -3.7583e+04 | 147.0780 | 1.1565e+03 |
| 0.0060 | 5.0500e-05 | 5.0000e-07 | -1.2500e-05 | -4.0984e+04 | -1.3929e+03 | 1.6922e+03 |
| 0.0080 | 8.0500e-05 | 2.5000e-06 | -9.5000e-06 | -4.6784e+04 | -170.9597 | 1.6364e+04 |
| 0.0100 | 9.9500e-05 | -2.5000e-06 | -4.5500e-05 | -5.4574e+04 | 1.4239e+03 | 3.4477e+04 |
| 0.0120 | 1.3650e-04 | -3.5000e-06 | -6.6500e-05 | -7.3616e+04 | -703.9999 | 3.0703e+04 |
| 0.0140 | 1.8400e-04 | 0 | -8.5000e-05 | -8.8209e+04 | -4.7217e+03 | 7.7951e+03 |
| 0.0160 | 2.3600e-04 | 1.0000e-05 | -4.5000e-05 | -8.7378e+04 | -6.1601e+03 | -1.6793e+04 |
| 0.0180 | 2.5750e-04 | 1.2500e-05 | -3.9500e-05 | -8.3312e+04 | -3.5525e+03 | -2.1067e+04 |
| 0.0200 | 3.0550e-04 | 3.5000e-06 | -7.3500e-05 | -9.7374e+04 | -858.8897 | -1.1237e+04 |
| 0.0220 | 3.3600e-04 | 9.0000e-06 | -7.4000e-05 | -1.0765e+05 | -3.0736e+03 | -2.0046e+04 |
| 0.0240 | 3.9100e-04 | 1.5000e-05 | -2.7000e-05 | -9.3724e+04 | -5.8026e+03 | -2.9136e+04 |
| 0.0260 | 4.1550e-04 | 1.5500e-05 | -1.6500e-05 | -4.9225e+04 | -5.8717e+03 | -1.1961e+04 |
| 0.0280 | 4.3700e-04 | 2.0000e-05 | -4.7000e-05 | -3.3306e+04 | -3.5457e+03 | 1.1020e+04 |
| 0.0300 | 4.5350e-04 | 2.0500e-05 | -5.2500e-05 | -3.9634e+04 | 676.5706 | 1.4013e+04 |
| 0.0320 | 4.8500e-04 | 2.1000e-05 | -2.6000e-05 | -5.5074e+04 | 4.5927e+03 | 5.6829e+03 |
| 0.0340 | 4.9900e-04 | 1.4000e-05 | -5.1000e-05 | -6.9219e+04 | 6.0278e+03 | -1.2395e+03 |
| 0.0360 | 5.1000e-04 | 1.5000e-05 | -5.0000e-05 | -8.4619e+04 | 4.0456e+03 | -1.3797e+04 |
| 0.0380 | 5.3250e-04 | 1.7500e-05 | -3.0500e-05 | -1.0259e+05 | 1.0681e+03 | -2.6746e+04 |
| 0.0400 | 5.4850e-04 | 1.6500e-05 | -2.3500e-05 | -1.2097e+05 | -1.7838e+03 | -3.8712e+04 |

Figure 8.73: RS-NO combination strain data

| | Standard Error Estimate |
|-------------------|-------------------------|
| Combined Strain p | 4.5510e-11 |
| Combined Strain q | 5.4279e-12 |
| Combined Strain t | 1.3999e-10 |

Figure 8.74: RS-NO estimated standard error in the combined strain calculations

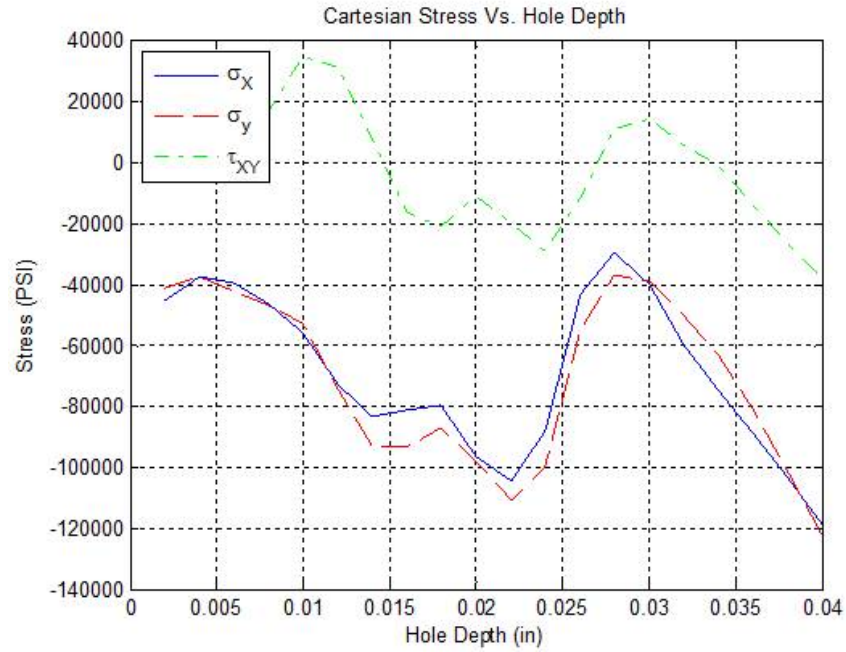


Figure 8.75: RS-NO Cartesian stresses versus depth. The X-direction corresponds to the longitudinal axis of the sample

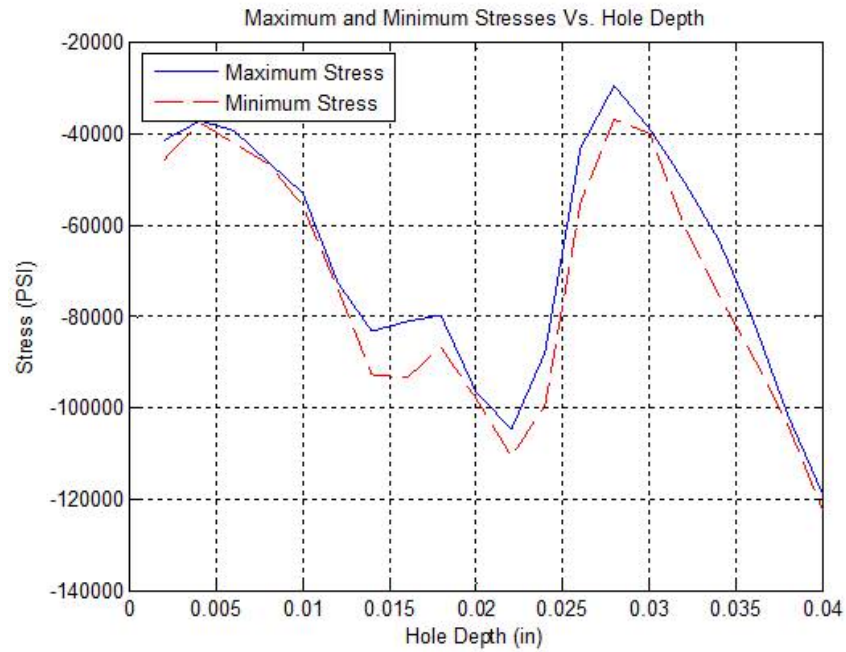


Figure 8.76: RS-NO magnitude of the maximum and minimum stresses as a function of depth below the surface

| Hole Depth (in) | Maximum Stress (psi) | Principal Direction (Deg.) Meas. Frm. Reference Dir. |
|--------------------|-------------------------|---|
| 0.0020 | -4.1486e+04 | -49.0150 |
| 0.0040 | -3.7436e+04 | -48.6238 |
| 0.0060 | -3.9591e+04 | -25.2701 |
| 0.0080 | -4.6614e+04 | -44.7007 |
| 0.0100 | -5.3151e+04 | -46.1825 |
| 0.0120 | -7.2912e+04 | -44.3432 |
| 0.0140 | -8.3488e+04 | -29.3979 |
| 0.0160 | -8.1218e+04 | 34.9278 |
| 0.0180 | -7.9759e+04 | 40.2142 |
| 0.0200 | -9.6515e+04 | 42.8145 |
| 0.0220 | -1.0458e+05 | 40.6415 |
| 0.0240 | -8.7921e+04 | 39.3683 |
| 0.0260 | -4.3353e+04 | 31.9268 |
| 0.0280 | -2.9760e+04 | -36.0823 |
| 0.0300 | -3.8958e+04 | -46.3821 |
| 0.0320 | -5.0482e+04 | -64.4720 |
| 0.0340 | -6.3191e+04 | 84.1902 |
| 0.0360 | -8.0574e+04 | 53.1710 |
| 0.0380 | -1.0152e+05 | 46.1435 |
| 0.0400 | -1.1918e+05 | 43.6809 |

Figure 8.77: RS-NO direction in which the maximum stresses act relative to the longitudinal axis of the sample (reference direction)

| Hole Depth (in) | Minimum Stress (psi) | Principal Direction (Deg.) Meas. Perp. to Reference Dir. |
|--------------------|-------------------------|---|
| 0.0020 | -4.5729e+04 | -49.0150 |
| 0.0040 | -3.7730e+04 | -48.6238 |
| 0.0060 | -4.2377e+04 | -25.2701 |
| 0.0080 | -4.6955e+04 | -44.7007 |
| 0.0100 | -5.5998e+04 | -46.1825 |
| 0.0120 | -7.4320e+04 | -44.3432 |
| 0.0140 | -9.2931e+04 | -29.3979 |
| 0.0160 | -9.3538e+04 | 34.9278 |
| 0.0180 | -8.6864e+04 | 40.2142 |
| 0.0200 | -9.8232e+04 | 42.8145 |
| 0.0220 | -1.1072e+05 | 40.6415 |
| 0.0240 | -9.9526e+04 | 39.3683 |
| 0.0260 | -5.5097e+04 | 31.9268 |
| 0.0280 | -3.6852e+04 | -36.0823 |
| 0.0300 | -4.0311e+04 | -46.3821 |
| 0.0320 | -5.9667e+04 | -64.4720 |
| 0.0340 | -7.5247e+04 | 84.1902 |
| 0.0360 | -8.8665e+04 | 53.1710 |
| 0.0380 | -1.0365e+05 | 46.1435 |
| 0.0400 | -1.2275e+05 | 43.6809 |

Figure 8.78: RS-NO direction in which the minimum stresses act relative to the longitudinal axis of the sample (reference direction)

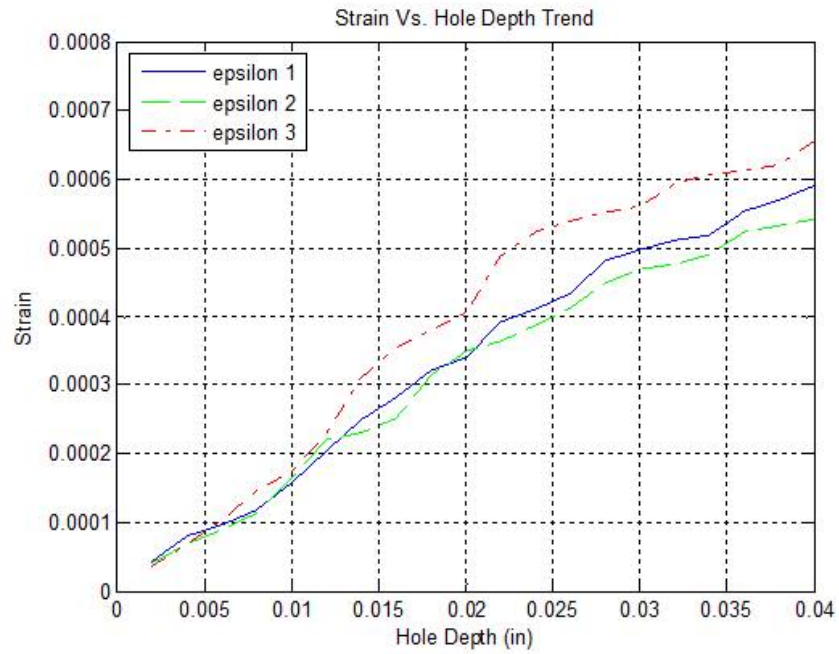


Figure 8.79: R-30 measured strain Vs. Depth

| Hole Depth (in) | Strain 1 Reference Direction | Strain 2 45 deg. frm. Ref. | Strain 3 Perpendicular to Ref. |
|-----------------|---------------------------------|-------------------------------|-----------------------------------|
| 0.0020 | 4.4000e-05 | 4.0000e-05 | 3.6000e-05 |
| 0.0040 | 8.0000e-05 | 6.8000e-05 | 6.8000e-05 |
| 0.0060 | 9.8000e-05 | 8.9000e-05 | 1.0300e-04 |
| 0.0080 | 1.1800e-04 | 1.1300e-04 | 1.4600e-04 |
| 0.0100 | 1.5700e-04 | 1.6400e-04 | 1.7500e-04 |
| 0.0120 | 2.0400e-04 | 2.2000e-04 | 2.3100e-04 |
| 0.0140 | 2.4800e-04 | 2.3100e-04 | 3.1100e-04 |
| 0.0160 | 2.8100e-04 | 2.5100e-04 | 3.5500e-04 |
| 0.0180 | 3.2100e-04 | 3.1500e-04 | 3.7900e-04 |
| 0.0200 | 3.4100e-04 | 3.4900e-04 | 4.0500e-04 |
| 0.0220 | 3.9200e-04 | 3.6300e-04 | 4.8700e-04 |
| 0.0240 | 4.1100e-04 | 3.8800e-04 | 5.2200e-04 |
| 0.0260 | 4.3400e-04 | 4.1400e-04 | 5.4000e-04 |
| 0.0280 | 4.8000e-04 | 4.4700e-04 | 5.5000e-04 |
| 0.0300 | 4.9800e-04 | 4.6900e-04 | 5.6000e-04 |
| 0.0320 | 5.1100e-04 | 4.7500e-04 | 5.9400e-04 |
| 0.0340 | 5.1800e-04 | 4.9000e-04 | 6.0800e-04 |
| 0.0360 | 5.5300e-04 | 5.2300e-04 | 6.1200e-04 |
| 0.0380 | 5.6900e-04 | 5.3300e-04 | 6.2100e-04 |
| 0.0400 | 5.9100e-04 | 5.4100e-04 | 6.5600e-04 |

Figure 8.80: RS-30 tabulated strain data

| Hole Depth (in) | Combined Strain p | Combined Strain q | Combined Strain t | Stress P (psi) | Stress Q (psi) | Stress T (psi) |
|-----------------|-------------------|-------------------|-------------------|----------------|----------------|----------------|
| 0.0020 | 4.0000e-05 | -4.0000e-06 | 0 | -1.1296e+05 | 5.9543e+03 | 1.1424e+04 |
| 0.0040 | 7.4000e-05 | -6.0000e-06 | 6.0000e-06 | -7.9176e+04 | 719.0314 | 651.4540 |
| 0.0060 | 1.0050e-04 | 2.5000e-06 | 1.1500e-05 | -5.6988e+04 | -1.2101e+04 | -1.8337e+04 |
| 0.0080 | 1.3200e-04 | 1.4000e-05 | 1.9000e-05 | -5.6180e+04 | -1.2127e+04 | -1.0032e+04 |
| 0.0100 | 1.6600e-04 | 9.0000e-06 | 2.0000e-06 | -7.2389e+04 | -3.3091e+03 | 1.8461e+03 |
| 0.0120 | 2.1750e-04 | 1.3500e-05 | -2.5000e-06 | -9.1185e+04 | -8.1546e+03 | -1.2497e+04 |
| 0.0140 | 2.7950e-04 | 3.1500e-05 | 4.8500e-05 | -9.4197e+04 | -1.1976e+04 | -2.8780e+04 |
| 0.0160 | 3.1800e-04 | 3.7000e-05 | 6.7000e-05 | -8.1362e+04 | -119.6715 | -8.5002e+03 |
| 0.0180 | 3.5000e-04 | 2.9000e-05 | 3.5000e-05 | -7.4404e+04 | -127.3987 | 7.0139e+03 |
| 0.0200 | 3.7300e-04 | 3.2000e-05 | 2.4000e-05 | -8.1838e+04 | -1.1335e+04 | -8.7869e+03 |
| 0.0220 | 4.3950e-04 | 4.7500e-05 | 7.6500e-05 | -8.9351e+04 | -2.0204e+04 | -3.2207e+04 |
| 0.0240 | 4.6650e-04 | 5.5500e-05 | 7.8500e-05 | -7.3959e+04 | -7.3947e+03 | -1.8643e+04 |
| 0.0260 | 4.8700e-04 | 5.3000e-05 | 7.3000e-05 | -4.5769e+04 | 1.7203e+04 | 6.0839e+03 |
| 0.0280 | 5.1500e-04 | 3.5000e-05 | 6.8000e-05 | -2.8902e+04 | 2.7769e+04 | 1.6922e+04 |
| 0.0300 | 5.2900e-04 | 3.1000e-05 | 6.0000e-05 | -2.6601e+04 | 1.0499e+04 | 1.1754e+04 |
| 0.0320 | 5.5250e-04 | 4.1500e-05 | 7.7500e-05 | -3.8245e+04 | -7.9158e+03 | 3.5610e+03 |
| 0.0340 | 5.6300e-04 | 4.5000e-05 | 7.3000e-05 | -6.0503e+04 | -3.1904e+03 | 5.5652e+03 |
| 0.0360 | 5.8250e-04 | 2.9500e-05 | 5.9500e-05 | -9.1475e+04 | 1.2924e+04 | 4.6088e+03 |
| 0.0380 | 5.9500e-04 | 2.6000e-05 | 6.2000e-05 | -1.2768e+05 | 1.7601e+04 | -1.0244e+04 |
| 0.0400 | 6.2350e-04 | 3.2500e-05 | 8.2500e-05 | -1.6628e+05 | 8.7619e+03 | -3.5637e+04 |

Figure 8.81: RS-30 combination strain data

| | Standard Error Estimate |
|-------------------|-------------------------|
| Combined Strain p | 4.5905e-11 |
| Combined Strain q | 1.5540e-11 |
| Combined Strain t | 1.1088e-10 |

Figure 8.82: RS-30 estimated standard error in the combined strain calculations

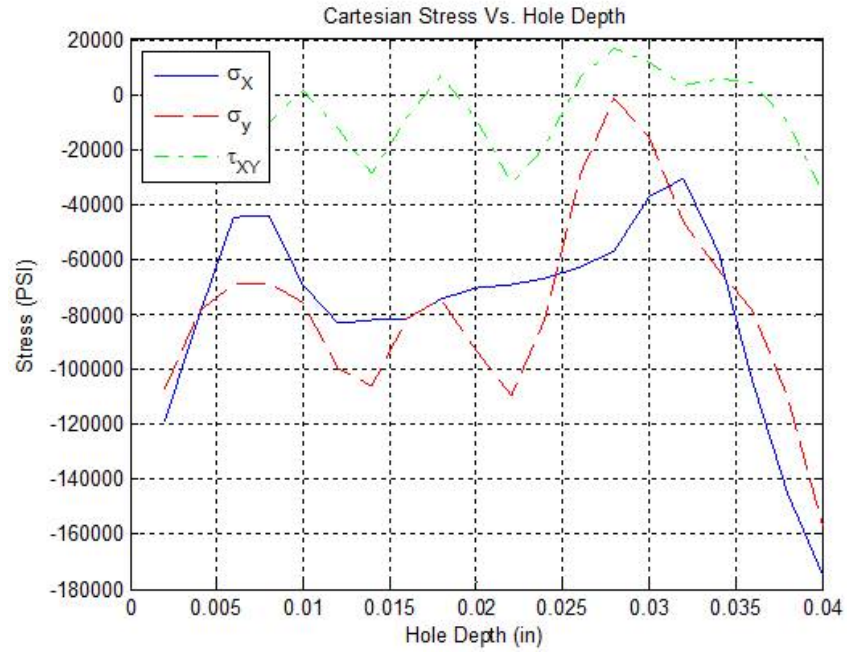


Figure 8.83: RS-30 Cartesian stresses versus depth. The X-direction corresponds to the longitudinal axis of the sample

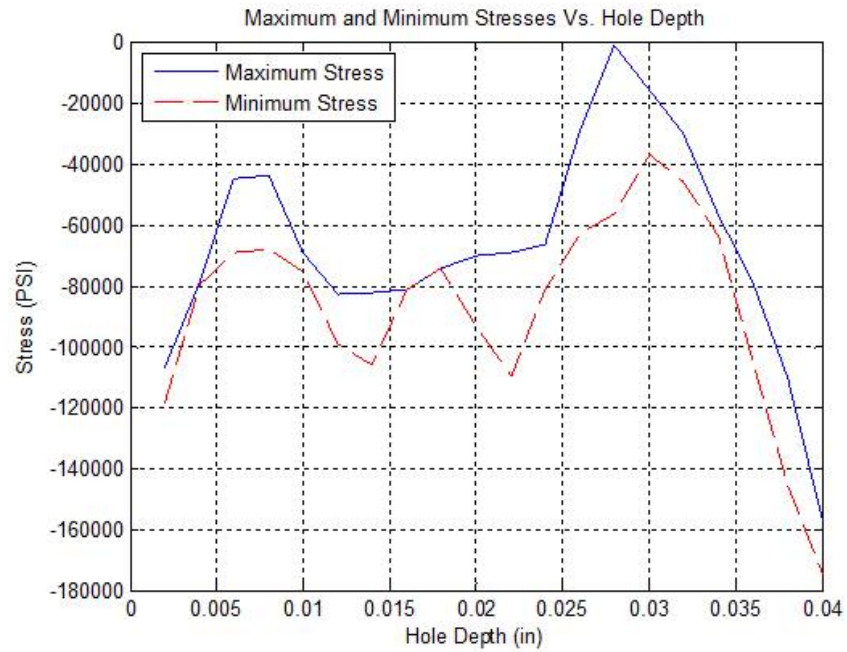


Figure 8.84: RS-30 magnitude of the maximum and minimum stresses as a function of depth below the surface

| Hole Depth (in) | Maximum Stress (psi) | Principal Direction (Deg.) Meas. Frm. Reference Dir. |
|--------------------|-------------------------|---|
| 0.0020 | -1.0701e+05 | -58.7643 |
| 0.0040 | -7.8457e+04 | -68.9115 |
| 0.0060 | -4.4887e+04 | 28.2896 |
| 0.0080 | -4.4053e+04 | 19.7997 |
| 0.0100 | -6.9080e+04 | -14.5785 |
| 0.0120 | -8.3031e+04 | 28.4374 |
| 0.0140 | -8.2221e+04 | 33.7030 |
| 0.0160 | -8.1243e+04 | 44.5967 |
| 0.0180 | -7.4277e+04 | -44.4797 |
| 0.0200 | -7.0503e+04 | 18.8910 |
| 0.0220 | -6.9147e+04 | 28.9495 |
| 0.0240 | -6.6564e+04 | 34.1824 |
| 0.0260 | -2.8566e+04 | -80.2619 |
| 0.0280 | -1.1334e+03 | -74.3208 |
| 0.0300 | -1.6102e+04 | -65.8858 |
| 0.0320 | -3.0329e+04 | -12.1104 |
| 0.0340 | -5.7312e+04 | -30.0878 |
| 0.0360 | -7.8551e+04 | -80.1868 |
| 0.0380 | -1.1008e+05 | 74.9003 |
| 0.0400 | -1.5752e+05 | 51.9065 |

Figure 8.85: RS-30 direction in which the maximum stresses act relative to the longitudinal axis of the sample (reference direction)

| Hole Depth (in) | Minimum Stress (psi) | Principal Direction (Deg.) Meas. Perp. to Reference Dir. |
|--------------------|-------------------------|---|
| 0.0020 | -1.1892e+05 | -58.7643 |
| 0.0040 | -7.9895e+04 | -68.9115 |
| 0.0060 | -6.9089e+04 | 28.2896 |
| 0.0080 | -6.8307e+04 | 19.7997 |
| 0.0100 | -7.5698e+04 | -14.5785 |
| 0.0120 | -9.9340e+04 | 28.4374 |
| 0.0140 | -1.0617e+05 | 33.7030 |
| 0.0160 | -8.1482e+04 | 44.5967 |
| 0.0180 | -7.4532e+04 | -44.4797 |
| 0.0200 | -9.3173e+04 | 18.8910 |
| 0.0220 | -1.0956e+05 | 28.9495 |
| 0.0240 | -8.1354e+04 | 34.1824 |
| 0.0260 | -6.2972e+04 | -80.2619 |
| 0.0280 | -5.6671e+04 | -74.3208 |
| 0.0300 | -3.7099e+04 | -65.8858 |
| 0.0320 | -4.6161e+04 | -12.1104 |
| 0.0340 | -6.3693e+04 | -30.0878 |
| 0.0360 | -1.0440e+05 | -80.1868 |
| 0.0380 | -1.4528e+05 | 74.9003 |
| 0.0400 | -1.7504e+05 | 51.9065 |

Figure 8.86: RS-30 direction in which the minimum stresses act relative to the longitudinal axis of the sample (reference direction)

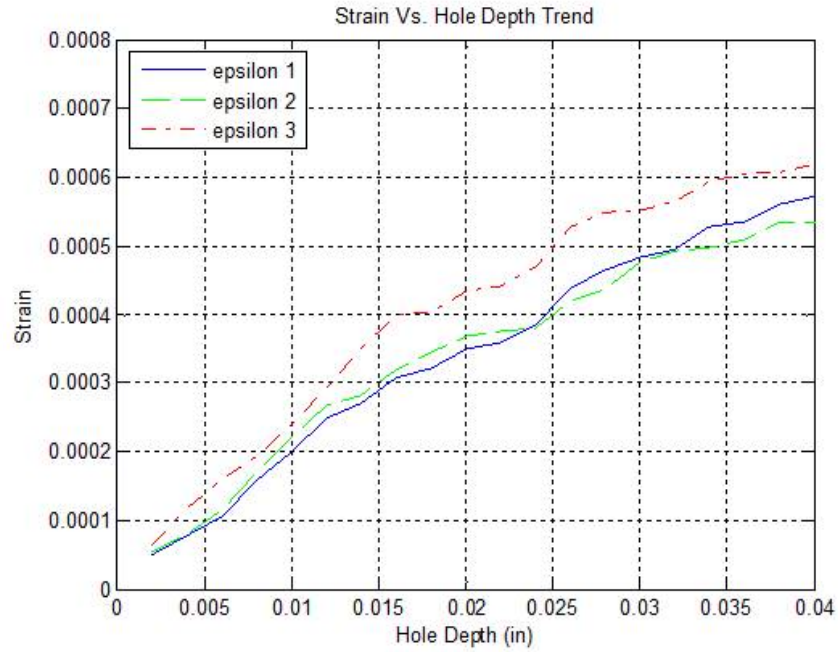


Figure 8.87: R-60 measured strain Vs. Depth

| Hole Depth (in) | Strain 1 Reference Direction | Strain 2 45 deg. frm. Ref. | Strain 3 Perpendicular to Ref. |
|-----------------|------------------------------|----------------------------|--------------------------------|
| 0.0020 | 5.1000e-05 | 5.6000e-05 | 6.4000e-05 |
| 0.0040 | 7.8000e-05 | 8.0000e-05 | 1.1900e-04 |
| 0.0060 | 1.0700e-04 | 1.1500e-04 | 1.6100e-04 |
| 0.0080 | 1.5700e-04 | 1.7000e-04 | 1.9400e-04 |
| 0.0100 | 1.9900e-04 | 2.2100e-04 | 2.3900e-04 |
| 0.0120 | 2.4900e-04 | 2.6700e-04 | 2.9300e-04 |
| 0.0140 | 2.7000e-04 | 2.8200e-04 | 3.4900e-04 |
| 0.0160 | 3.0700e-04 | 3.2000e-04 | 4.0000e-04 |
| 0.0180 | 3.2200e-04 | 3.4500e-04 | 4.0400e-04 |
| 0.0200 | 3.5000e-04 | 3.6800e-04 | 4.3300e-04 |
| 0.0220 | 3.5800e-04 | 3.7600e-04 | 4.4200e-04 |
| 0.0240 | 3.8500e-04 | 3.8100e-04 | 4.6900e-04 |
| 0.0260 | 4.3900e-04 | 4.1900e-04 | 5.2700e-04 |
| 0.0280 | 4.6400e-04 | 4.3700e-04 | 5.4800e-04 |
| 0.0300 | 4.8200e-04 | 4.7500e-04 | 5.5200e-04 |
| 0.0320 | 4.9500e-04 | 4.9300e-04 | 5.6400e-04 |
| 0.0340 | 5.2700e-04 | 4.9800e-04 | 5.9400e-04 |
| 0.0360 | 5.3500e-04 | 5.0800e-04 | 6.0500e-04 |
| 0.0380 | 5.6000e-04 | 5.3400e-04 | 6.0800e-04 |
| 0.0400 | 5.7300e-04 | 5.3500e-04 | 6.1900e-04 |

Figure 8.88: RS-60 tabulated strain data

| Hole Depth (in) | Combined Strain p | Combined Strain q | Combined Strain t | Stress P (psi) | Stress Q (psi) | Stress T (psi) |
|-----------------|-------------------|-------------------|-------------------|----------------|----------------|----------------|
| 0.0020 | 5.7500e-05 | 6.5000e-06 | 1.5000e-06 | -1.6367e+05 | -1.4435e+04 | -3.9203e+03 |
| 0.0040 | 9.8500e-05 | 2.0500e-05 | 1.8500e-05 | -8.2262e+04 | -873.5612 | -1.0910e+03 |
| 0.0060 | 1.3400e-04 | 2.7000e-05 | 1.9000e-05 | -5.2674e+04 | -2.7381e+04 | -1.4616e+04 |
| 0.0080 | 1.7550e-04 | 1.8500e-05 | 5.5000e-06 | -6.1810e+04 | 1.5330e+04 | 1.1568e+04 |
| 0.0100 | 2.1900e-04 | 2.0000e-05 | -2.0000e-06 | -6.8322e+04 | 3.3400e+03 | 1.2543e+04 |
| 0.0120 | 2.7100e-04 | 2.2000e-05 | 4.0000e-06 | -8.3239e+04 | -2.6239e+03 | -1.4356e+04 |
| 0.0140 | 3.0950e-04 | 3.9500e-05 | 2.7500e-05 | -5.7756e+04 | -3.3267e+04 | -3.3577e+04 |
| 0.0160 | 3.5350e-04 | 4.6500e-05 | 3.3500e-05 | -5.2659e+04 | -4.5644e+04 | -1.0193e+04 |
| 0.0180 | 3.6300e-04 | 4.1000e-05 | 1.8000e-05 | 2.0088e+04 | 6.1333e+04 | 2.6038e+04 |
| 0.0200 | 3.9150e-04 | 4.1500e-05 | 2.3500e-05 | -1.6191e+04 | 1.0370e+04 | 1.0233e+04 |
| 0.0220 | 4.0000e-04 | 4.2000e-05 | 2.4000e-05 | -2.6973e+04 | -2.5271e+03 | -1.5918e+04 |
| 0.0240 | 4.2700e-04 | 4.2000e-05 | 4.6000e-05 | -1.3314e+05 | -1.4306e+03 | -4.1850e+04 |
| 0.0260 | 4.8300e-04 | 4.4000e-05 | 6.4000e-05 | 1.5817e+04 | -3.1415e+03 | -3.0422e+04 |
| 0.0280 | 5.0600e-04 | 4.2000e-05 | 6.9000e-05 | -1.2971e+05 | 1.1823e+04 | 1.3747e+04 |
| 0.0300 | 5.1700e-04 | 3.5000e-05 | 4.2000e-05 | -4.7758e+04 | 1.4581e+04 | 4.3287e+04 |
| 0.0320 | 5.2950e-04 | 3.4500e-05 | 3.6500e-05 | -3.6376e+04 | 862.8520 | 1.2869e+04 |
| 0.0340 | 5.6050e-04 | 3.3500e-05 | 6.2500e-05 | -8.9993e+04 | 4.5029e+03 | -2.0030e+04 |
| 0.0360 | 5.7000e-04 | 3.5000e-05 | 6.2000e-05 | -5.8403e+04 | 1.9235e+04 | -6.9258e+03 |
| 0.0380 | 5.8400e-04 | 2.4000e-05 | 5.0000e-05 | -4.0031e+04 | 9.2993e+03 | -3.6363e+03 |
| 0.0400 | 5.9600e-04 | 2.3000e-05 | 6.1000e-05 | -3.5972e+04 | -829.1412 | -1.7897e+04 |

Figure 8.89: RS-60 combination strain data

| | Standard Error Estimate |
|-------------------|-------------------------|
| Combined Strain p | 4.6135e-11 |
| Combined Strain q | 8.8816e-12 |
| Combined Strain t | 4.0405e-11 |

Figure 8.90: RS-60 estimated standard error in the combined strain calculations

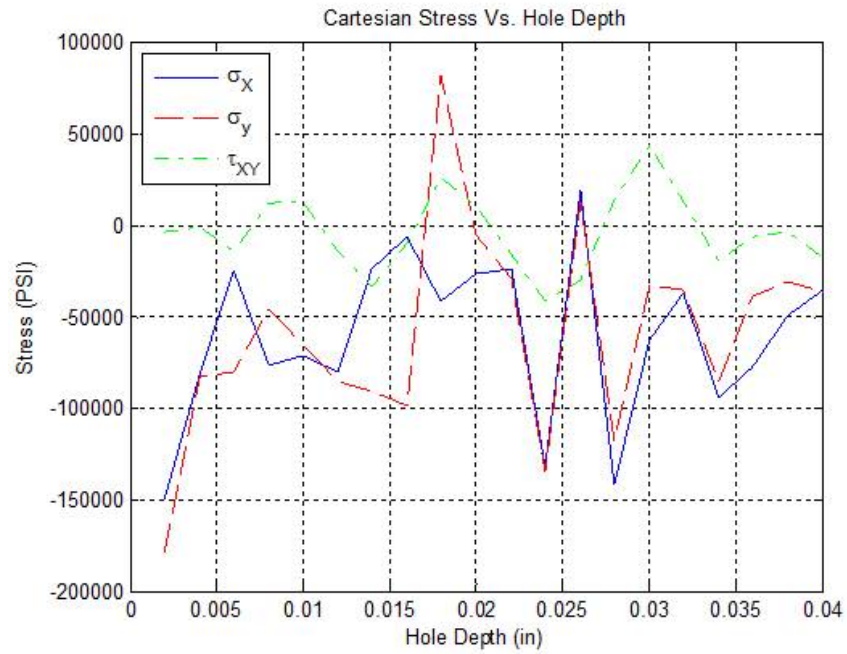


Figure 8.91: RS-60 Cartesian stresses versus depth. The X-direction corresponds to the longitudinal axis of the sample

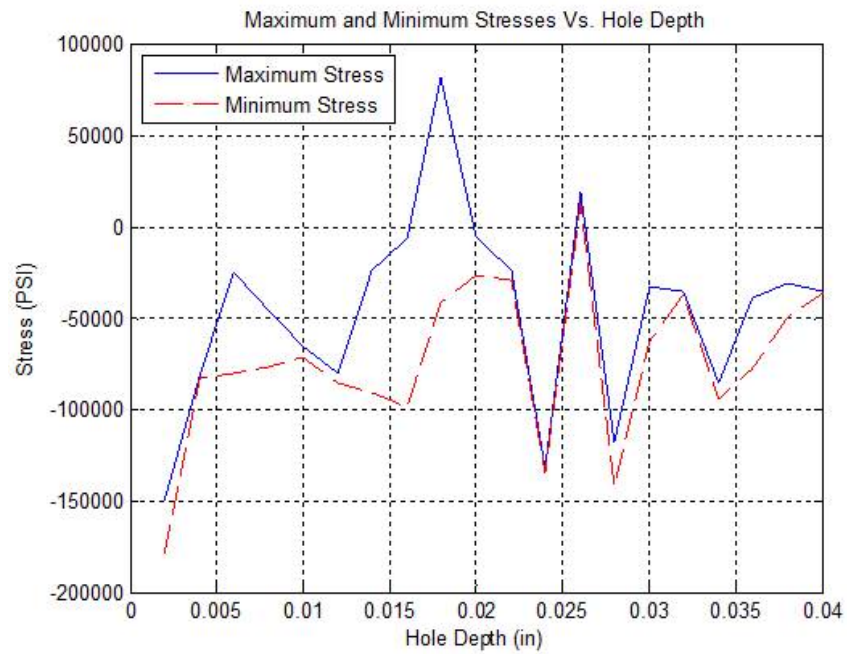


Figure 8.92: RS-60 magnitude of the maximum and minimum stresses as a function of depth below the surface

| Hole Depth (in) | Maximum Stress (psi) | Principal Direction (Deg.) Meas. Frm. Reference Dir. |
|--------------------|-------------------------|---|
| 0.0020 | -1.4924e+05 | 7.5971 |
| 0.0040 | -8.1388e+04 | 25.6575 |
| 0.0060 | -2.5293e+04 | 14.0467 |
| 0.0080 | -4.6481e+04 | -71.4802 |
| 0.0100 | -6.4982e+04 | -52.4553 |
| 0.0120 | -8.0615e+04 | 39.8212 |
| 0.0140 | -2.4488e+04 | 22.6326 |
| 0.0160 | -7.0149e+03 | 6.2944 |
| 0.0180 | 8.1421e+04 | -78.4985 |
| 0.0200 | -5.8216e+03 | -67.6897 |
| 0.0220 | -2.4445e+04 | 40.4896 |
| 0.0240 | -1.3171e+05 | 44.0211 |
| 0.0260 | 1.8959e+04 | 42.0521 |
| 0.0280 | -1.1789e+05 | -65.3488 |
| 0.0300 | -3.3178e+04 | -54.3078 |
| 0.0320 | -3.5513e+04 | -46.9179 |
| 0.0340 | -8.5491e+04 | 51.3348 |
| 0.0360 | -3.9168e+04 | 80.0991 |
| 0.0380 | -3.0732e+04 | 79.3216 |
| 0.0400 | -3.5143e+04 | 43.6737 |

Figure 8.93: RS-60 direction in which the maximum stresses act relative to the longitudinal axis of the sample (reference direction)

| Hole Depth (in) | Minimum Stress (psi) | Principal Direction (Deg.) Meas. Perp. to Reference Dir. |
|--------------------|-------------------------|---|
| 0.0020 | -1.7811e+05 | 7.5971 |
| 0.0040 | -8.3136e+04 | 25.6575 |
| 0.0060 | -8.0055e+04 | 14.0467 |
| 0.0080 | -7.7140e+04 | -71.4802 |
| 0.0100 | -7.1662e+04 | -52.4553 |
| 0.0120 | -8.5863e+04 | 39.8212 |
| 0.0140 | -9.1023e+04 | 22.6326 |
| 0.0160 | -9.8302e+04 | 6.2944 |
| 0.0180 | -4.1246e+04 | -78.4985 |
| 0.0200 | -2.6561e+04 | -67.6897 |
| 0.0220 | -2.9500e+04 | 40.4896 |
| 0.0240 | -1.3457e+05 | 44.0211 |
| 0.0260 | 1.2676e+04 | 42.0521 |
| 0.0280 | -1.4153e+05 | -65.3488 |
| 0.0300 | -6.2339e+04 | -54.3078 |
| 0.0320 | -3.7239e+04 | -46.9179 |
| 0.0340 | -9.4496e+04 | 51.3348 |
| 0.0360 | -7.7638e+04 | 80.0991 |
| 0.0380 | -4.9331e+04 | 79.3216 |
| 0.0400 | -3.6801e+04 | 43.6737 |

Figure 8.94: RS-60 direction in which the minimum stresses act relative to the longitudinal axis of the sample (reference direction)

Appendix E – Hardness Survey Data

9.1 Introduction

Microhardness surveys were conducted on each sample condition using an indenter load of 500g. For the laser processed coupons, RS-NO, RS-30, and RS-60, the hardness survey comprised a 10×15 matrix with 0.2 mm (0.005 inch) indent spacing. For the control specimen hardness survey, a 10×5 matrix with 0.2 mm (0.005 inch) spacing was used. The datum for each matrix, (1,1) was adjacent to the drilled hole near the sample surface. For all laser clad specimens, the fusion line was located approximately 0.040 inch (1 mm) below the sample surface. Overviews of the indent matrices and 3-D hardness color maps are presented in the subsequent section.

9.2 Hardness Data



Figure 9.95: RS-CO microhardness survey matrix overview

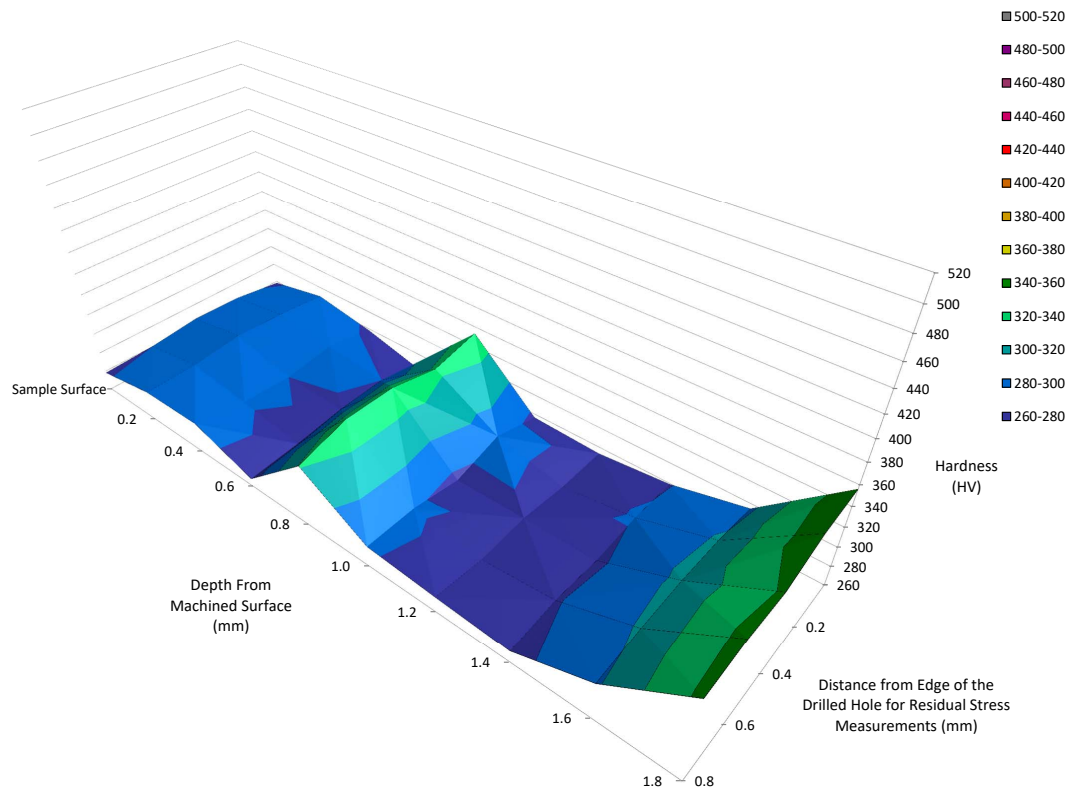


Figure 9.96: RS-CO microhardness map

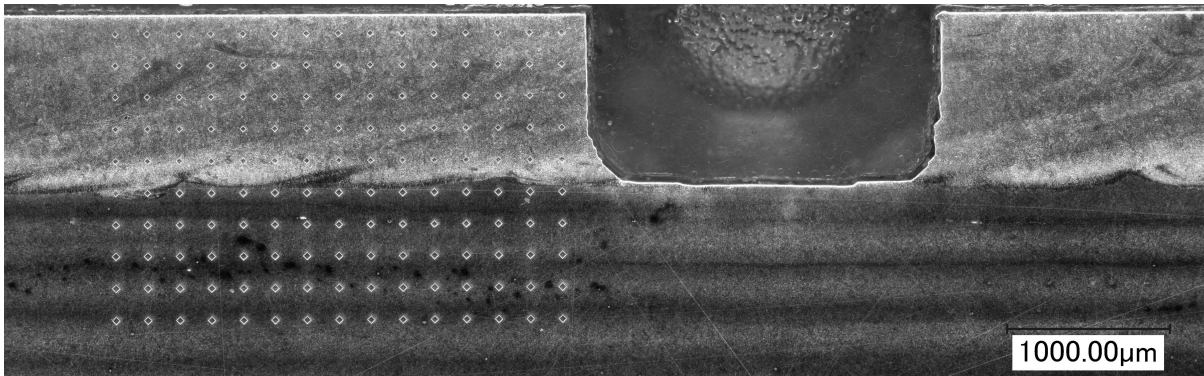


Figure 9.97: RS-NO hardness survey matrix overview

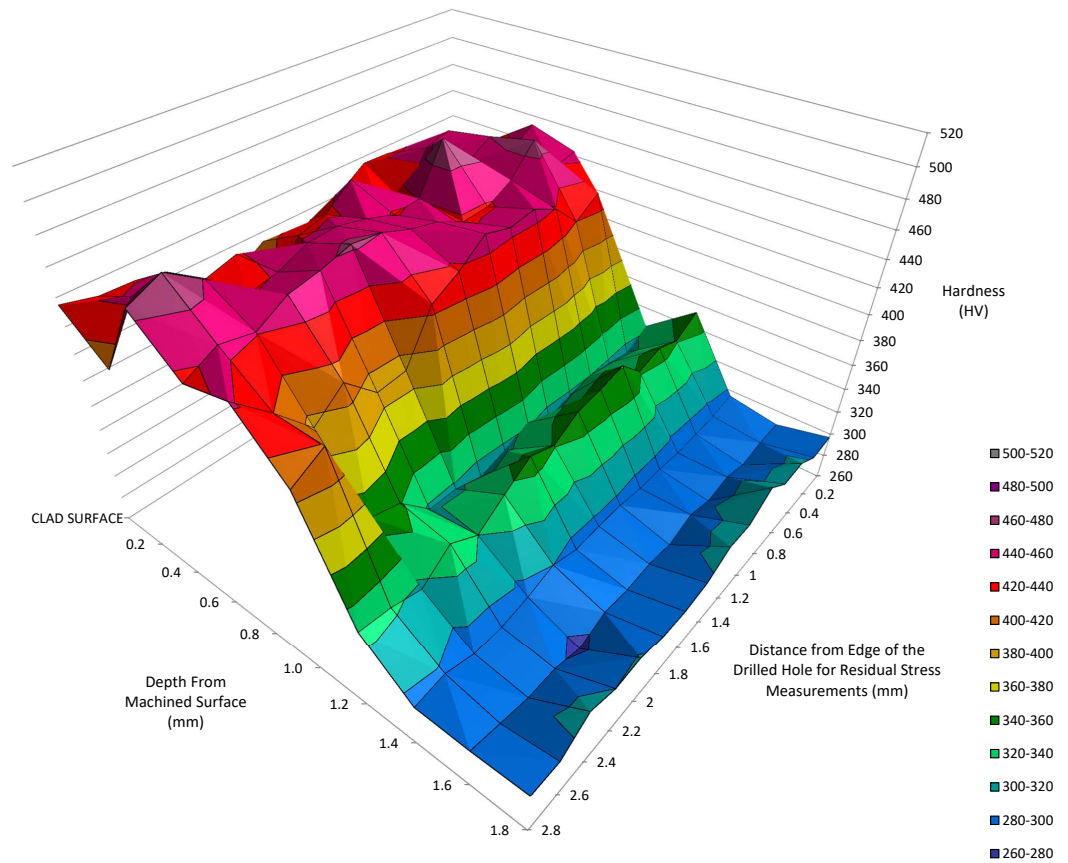


Figure 9.98: RS-NO microhardness map

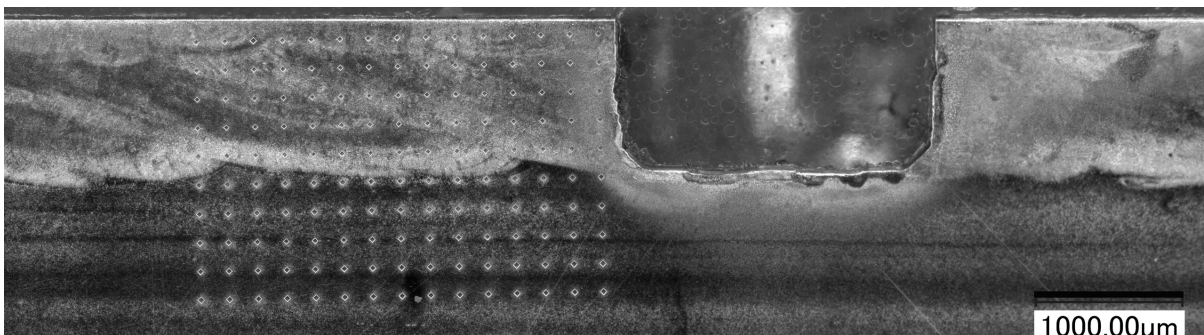


Figure 9.99: RS-30 microhardness survey matrix overview

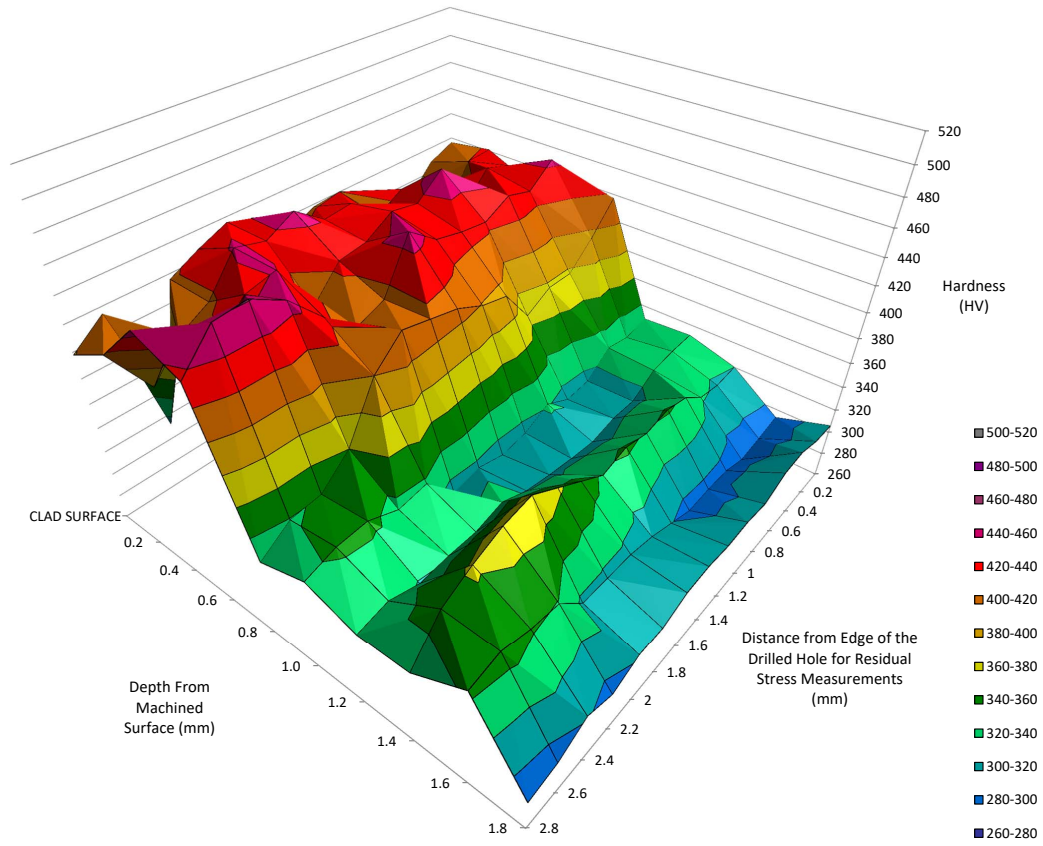


Figure 9.100: RS-30 microhardness map

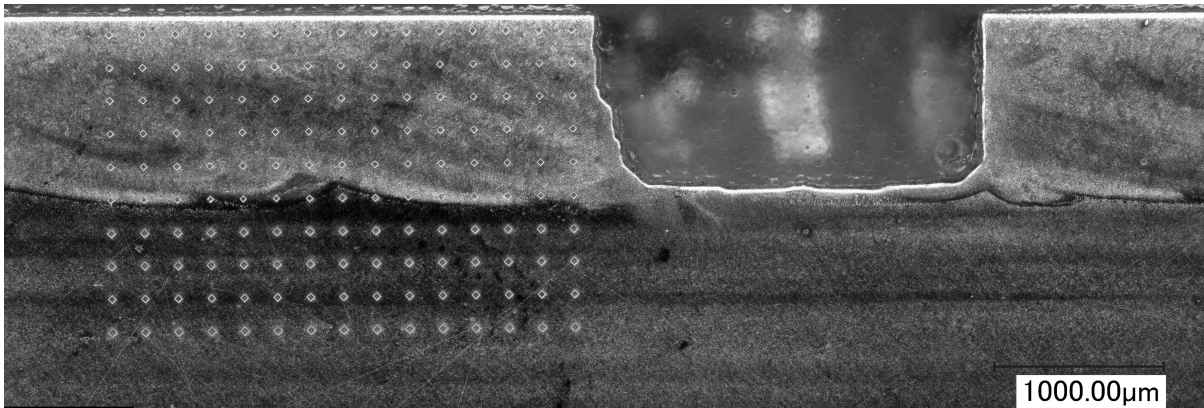


Figure 9.101: RS-60 microhardness survey matrix overview

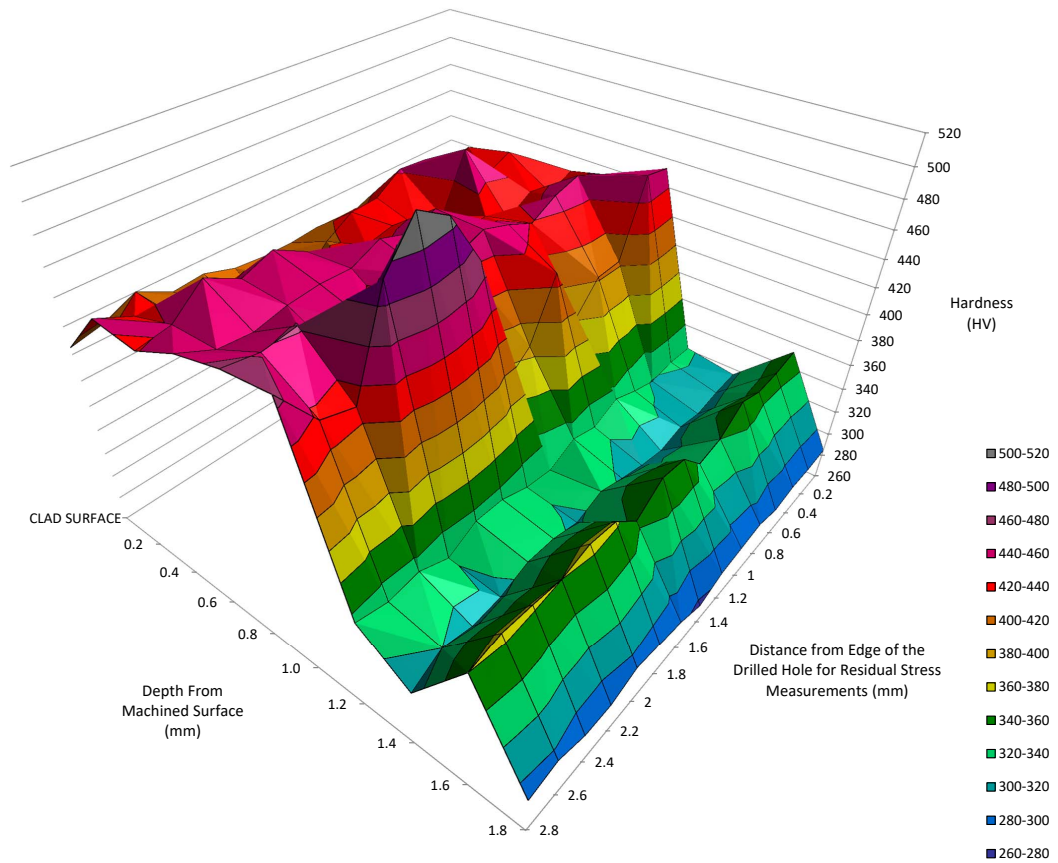


Figure 9.102: RS-60 microhardness hardness map

Appendix F – MatLab Scripts

10.1 Introduction

The following script was created to perform the iterative calculations outlined in ASTM E837-2008 for non-uniform stresses in a thick work-piece.

10.2 Main MatLab Program

```
1 %This script is used to calculate the residual stress in a part through
2 %the Vishay hole-drilling method as per ASTM E837-08.
3 %This method is based upon non-uniform stress conditions in a thick
4 %workpiece using a 1/16" Nominal TYPE A/B Rosette.
5 %USE OF ANYOTHER TYPE OR SIZE OF ROSETTE WILL LEAD TO INVALID
6 %CALCULATIONS!!!!
7
8 display('This script is used to calculate residual stresses as per')
9 display('ASTM E837-08. It is designed to be used with a 1/16in nominal')
10 display('Type A/B Rosette-USE OF ANYOTHER SIZE OR ROSETTE TYPE WILL LEAD')
11 display('TO INVALID CALCULATIONS!!!! ')
12 display('Make sure proper calibration matrix values are saved in the ...
    working file')
```

```
13 display('To proceed ensure that all strain data is saved in')
14 display('C:\Documents\MATLAB\Residual Stress\Strain Gauge Rosette ...
    Data.xlsx')
15 display('and formatted by column in the following order: HoleDepth | ...
    ep1 | ep2 | ep3 where')
16 display('ep1 represents strain in the reference direction')
17 display('the hole depth must be listed in 0.002in steps and begin at i ...
    = 1 = 0.002in')
18 display('(i.e. OMIT 0in depth) and terminate at i = 20 = 0.040in')
19
20 %Prompt to ensure display above is being followed.
21 prompt=input(['Did you use type A or B Rosette & Save data ...
    appropriately?'],...
    ' Enter '1' for y, '0' for no ans= ');
22
23 if isempty(prompt);
24     disp('Invalid Entry...exiting script');
25     return
26 elseif prompt==0;
27     disp(['I don't have what you need...its not you...its me',...
    ' exiting script']);
28     return
29 elseif prompt~=0 & prompt~=1;
30     disp('invalid key - exiting script');
31     return
32 elseif prompt==1;
33
34
35 end
36
37 %Prompts for output filename
38 prompt = {'Enter Data Output file name: '};
39 dlg_title = 'Excel Output File Name';
```

```
40 num_lines=1;
41 def= {'DEMO1.xlsx'};
42 file_name = inputdlg(prompt,dlg_title,num_lines,def);
43
44 %Changes filename to .ppt extension for use with saveppt.m function
45 ppt=cellstr('.ppt')
46 ppt_name=strcat(file_name{1},ppt)
47
48 [E]=modulus(); %input prompt for modulus
49 [mu]=poisson(); %input prompt for poissons ratio
50 [hole_dia]=hole_dia(); %input prompt for the measured hole diameter
51 [a]=calib_matrix_a(hole_dia); %Generate Calibration Matix a for calcs
52 [b]=calib_matrix_b(hole_dia); %Generate Calibration Matix b for calcs
53 [c]=matrix_c(); %Generate Calibration Matix c for calcs
54
55 strain_data = xlsread('Strain Gauge Rosette Data.xlsx');
56 holeddepth = strain_data(:,1);
57 ep1 = strain_data(:,2)*1E-6;
58 ep2 = strain_data(:,3)*1E-6;
59 ep3 = strain_data(:,4)*1E-6;
60
61 %Plot strain data to ensure the data follows smooth trends
62 figure(1);
63 plot(holeddepth,ep1,'b-',holeddepth,ep2,'g--',holeddepth,ep3,'r-.');
64 xlabel('Hole Depth (in)');
65 ylabel('Strain');
66 set(gca,'YTickLabel',num2str(get(gca,'YTick').'));
67 title('Strain Vs. Hole Depth Trend');
68 legend('epsilon 1', 'epsilon 2', 'epsilon 3','Location', 'NorthWest');
69 grid on;
70 F1=gcf;
```

```
71
72 prompt=input('Does Fig. 1 Plot data follow smooth trends? 1=y, 0=n ans=');
73 if isempty(prompt);
74     disp('Check yo''data, before you wreck yo''data...exiting script');
75     return
76 elseif prompt==0;
77     disp('Check yo''data, before you wreck yo''data...exiting script');
78     return
79 elseif prompt≠0 & prompt≠1 ;
80     disp('invalid key - exiting script');
81     return
82 elseif prompt==1;
83
84 end
85
86 %p,q,t strain vector calculation
87 p=(ep3+ep1)/2;
88 q=(ep3-ep1)/2;
89 t=(ep3+ep1-2*ep2)/2;
90
91 %p_std err, q_std error, t_std error Calculation
92 [p_std_err_sum,q_std_err_sum,t_std_err_sum]=strain_std_err(p,q,t);
93
94 %Calculation of Stress P for nonuniform stress state
95 [P]=stress_calc_P(a,c,E,mu,p,p_std_err_sum);
96
97 %Calculation of Stress Q for nonuniform stress state
98 [Q]=stress_calc_Q(b,c,E,q,q_std_err_sum);
99
100 %Calculation of Stress T for nonuniform stress state
101 [T]=stress_calc_T(b,c,E,t,t_std_err_sum);
```

```
102
103 %Cartesian Stress Calculation
104 sig_x=P-Q;
105 sig_y=P+Q;
106 shear_xy=T;
107
108 %Principal Stress and Direction
109 sig_max=P+sqrt(Q.^2+t.^2);
110 sig_min=P-sqrt(Q.^2+t.^2);
111 beta_direc = 0.5 * atan2d(-T,-Q);
112
113 %Plot Max and Min Stress Vs. Hole Depth
114 figure(2);
115 plot(holedepth,sig_max,'b-',holedepth,sig_min,'r--');
116 xlabel('Hole Depth (in)');
117 ylabel('Stress (PSI)');
118 set(gca,'YTickLabel',num2str(get(gca,'YTick').'));
119 title('Maximum and Minimum Stresses Vs. Hole Depth');
120 legend('Maximum Stress', 'Minimum Stress','Location', 'NorthWest');
121 grid on;
122 F2=gcf;
123
124 %Plot Cartesian stress and shear Vs. Hole Depth
125 figure(3);
126 plot(holedepth,sig_x,'b-',holedepth,sig_y,'r--', holedepth,shear_xy,'g-.');
127 xlabel('Hole Depth (in)');
128 ylabel('Stress (PSI)');
129 set(gca,'YTickLabel',num2str(get(gca,'YTick').'));
130 title('Cartesian Stress Vs. Hole Depth');
131 legend('\sigma-{X}', '\sigma-{y}', '\tau-{XY}','Location', 'NorthWest');
132 grid on;
```

```
133 F3=gcf;
134
135
136 %Create Tablulated Data and Export to Excel
137 warning('off','MATLAB:xlswrite:AddSheet') %suppress add-sheet error
138 run max_stress_table
139 run min_stress_table
140 run xy_stress_table
141 run strain_data_tabulation
142 run comb_strain_data_tabulation
143 run std_err_tabulation
144
145 %Save All Figures to Power Point
146 saveppt(char(ppt_name),'Strain Vs. Hole Depth','-f1')
147 pause(2)
148 saveppt(char(ppt_name),'Max and Min. Stresses Vs. Hole Depth','-f2')
149 pause(2)
150 saveppt(char(ppt_name),'Cartesian Stress Vs. Hole Depth','-f3')
151 pause(2)
152 saveppt(char(ppt_name),'Max. Stress & Direction Table','-f4')
153 pause(2)
154 saveppt(char(ppt_name),'Min. Stress & Direction Table','-f5')
155 pause(2)
156 saveppt(char(ppt_name),'X/Y Stresses Table','-f6')
157 pause(2)
158 saveppt(char(ppt_name),'Strain Data Tabulation','-f7')
159 pause(2)
160 saveppt(char(ppt_name),'Combination Strain Data Table','-f8')
161 pause(2)
162 saveppt(char(ppt_name),'Estimated Std. Errors','-f9')
```

10.3 Functions

```
1
2 function[a]=calib_matrix_a(hole_dia)
3 %Retrives ASTM E837-08 calibration matrix a for non-uniform calculations
4 %Ensure excel file "ASTM E837-08 Calibration Matrix A Values" is saved in
5 %the current directory
6
7 calibration_matrix_raw=xlsread('ASTM E837-08 Calibration Matrix A ...
      Values','B4:U23');
8 a=calibration_matrix_raw*( hole_dia/0.080 );
9
10 function[b]=calib_matrix_b(hole_dia)
11 %Retrives ASTM E837-08 calibration matrix a for non-uniform calculations
12 %Ensure excel file "ASTM E837-08 Calibration Matrix B Values" is saved in
13 %the current directory
14
15
16 calibration_matrix_raw=xlsread('ASTM E837-08 Calibration Matrix B ...
      Values','B4:U23');
17 b=calibration_matrix_raw*( hole_dia/0.080 );
18
19 function[filename]=Filename_prompt()
20 %This function requests the user to input the file name underwhich all
21 %data outputs will be saved. All data will be saved in
22 % Mydocuments/matlab/filename
23
24 prompt = {'Enter output file name:  '}
25 dlg_title = 'Output file name'
```

```
26 num_lines=1
27 def= {'demo1.xlsx'}
28 file_name = inputdlg(prompt,dlg_title,num_lines,def)
29
30
31 filename=input('Please enter filename for data output: ')
32 if isempty{filename}
33     filename='data'
34 end
35
36
37 function[hole_dia]=hole_dia()
38 %Function requires the operator to enter the measured diameter of the hole
39 %This value is essential because it modifies both calibration matrices
40 hole_dia=input('Input measured hole dia.(min = 0.075'''' max= ...
    0.085'''' ) =')
41 if isempty(hole_dia)
42     hole_dia=0.080
43 end
44
45 function [c] = matrix_c()
46 %function generates tri-diagonal "second derivitive" matrix c
47 %Used for Tikhonov Refularization of Non-Uniform Stress data per E837-08
48 n=20;
49 D=sparse(1:n,1:n,2*ones(1,n),n,n);
50 E=sparse(2:n,1:n-1, -ones(1,n-1),n,n);
51 S=E+D+E';
52 c=full(S);
53 c(1,1)=0;
54 c(1,2)=0;
55 c(n,n)=0;
```

```
56 c(n,n-1)=0;
57
58 function[E]=modulus()
59 %This function requests the user to input the modulus of elasticity for
60 %use in calculations
61 E=input('Modulus of Elasticity (psi) leave blank for 30x10^6=')
62 if isempty(E)
63     E=30000000
64 end
65
66 function[mu]=poisson()
67 %Function requires the operator to enter the value of Poissons ratio for
68 %use in calculations (generally 0.30 for steels)
69 mu=input('Poisson's Ratio (leave blank for mu=0.30) =')
70 if isempty(mu)
71     mu=0.30
72 end
73
74 function[p_std_err_sum,q_std_err_sum,t_std_err_sum]=strain_std_err(p,q,t)
75 %Calculates the Combined Strain Standard Error
76 %Ensure combined strains are labeled p, q, and t and are arranged as column
77 %vectors
78 n=numel(p)-3;
79 p_std_err=zeros(n,1);
80 for i=1:n
81     p_std_err(i)=( p(i,1)-3*p(i+1,1)+3*p(i+2,1)-p(i+3,1) )^2 / ( 20 * n);
82 end
83 p_std_err_sum=sum(p_std_err);
84
85 n=numel(q)-3;
86 q_std_err=zeros(n,1);
```

```

87 for i=1:n
88     q_std_err(i)=( q(i,1)-3*q(i+1,1)+3*q(i+2,1)-q(i+3,1) )^2 / ( 20 * n);
89 end
90 q_std_err_sum=sum(q_std_err);
91
92 n=numel(t)-3;
93 t_std_err=zeros(n,1);
94 for i=1:n
95     t_std_err(i)=( t(i,1)-3*t(i+1,1)+3*t(i+2,1)-t(i+3,1) )^2 / ( 20 * n);
96 end
97 t_std_err_sum=su
98
99 function[P]=stress_calc_P(a,c,E,mu,p,p_std_err_sum)
100 %Calc. of stress P for non-unifor(a,c,E,mu,p)m stress calcs per ASTM ...
    E837-08
101 %Initial geuss for alpha_p = 1x10^-6
102
103 %Initial Stress P Calculation
104 alpha_p=1E-06 ;
105 A=a'*a + alpha_p*(c'*c) ;
106 B=(E/(1+mu))*a'*p ;
107 P=A\B ;
108
109 P_misfit=p-((1+mu)/E)*a*P; %misfit vector calcualtion
110 p_rms_misfit=(sum(P_misfit.^2))/numel(P_misfit);
111
112 if ((p_std_err_sum*0.95)<=p_rms_misfit...
113     & p_rms_misfit<=(p_std_err_sum*1.05))%checks validity of initial ...
        alpha geuss
114     disp(P)

```

```

115     %if the initial geuss if off, the following loop should recalculate ...
        the value
116 else while ((p_std_err_sum*0.95)≥p_rms_misfit...
        | p_rms_misfit≥(p_std_err_sum*1.05))
117     alpha_p=(p_std_err_sum/p_rms_misfit)*alpha_p
118     A=a'*a + alpha_p*(c'*c) ;
119     P=A\B ;
120     P_misfit=p-((1+mu)/E)*a*P; %misfit vector calcaultion
121     p_rms_misfit=(sum(P_misfit.^2))/numel(P_misfit);
122
123
124 end
125 P
126 end
127
128
129 function [Q]=stress_calc_Q(b,c,E,q,q_std_err_sum)
130 %Calc. of stress Q for non-unifor(a,c,E,mu,p)m stress calcs per ASTM ...
        E837-08
131 %Initial geuss for alpha_p = 1x10^-6
132
133 %Initial Stress P Calculation
134 alpha_q=1E-06 ;
135 A=b'*b + alpha_q*(c'*c) ;
136 B=E*b'*q ;
137 Q=A\B ;
138
139 Q_misfit=q-(1/E)*b*Q; %misfit vector calcaultion
140 q_rms_misfit=(sum(Q_misfit.^2))/numel(Q_misfit);
141
142 if ((q_std_err_sum*0.95)≤q_rms_misfit...

```

```

143     & q_rms_misfit<=(q_std_err_sum*1.05))%checks validity of initial ...
        alpha_geuss
144     disp(Q)
145     %if the initial geuss if off, the following loop should recalculate ...
        the value
146 else while ((q_std_err_sum*0.95)>=q_rms_misfit...
        | q_rms_misfit>=(q_std_err_sum*1.05))
147     alpha_q=(q_std_err_sum/q_rms_misfit)*alpha_q
148     A=b'*b + alpha_q*(c'*c) ;
149     Q=A\B ;
150     Q_misfit=q-(1/E)*b*Q; %misfit vector calcualtion
151     q_rms_misfit=(sum(Q_misfit.^2))/numel(Q_misfit);
152
153
154 end
155 Q
156 end
157
158 function [T]=stress_calc_T(b,c,E,t,t_std_err_sum)
159 %Calc. of stress Q for non-unifor(a,c,E,mu,p)m stress calcs per ASTM ...
        E837-08
160 %Initial geuss for alpha_p = 1x10^-6
161
162 %Initial Stress P Calculation
163 alpha_t=1E-06 ;
164 A=b'*b + alpha_t*(c'*c) ;
165 B=E*b'*t ;
166 T=A\B ;
167
168 T_misfit=t-(1/E)*b*T; %misfit vector calcualtion
169 t_rms_misfit=(sum(T_misfit.^2))/numel(T_misfit);
170

```

```
171 if ((t_std_err_sum*0.95)≤t_rms_misfit...
172     & t_rms_misfit≤(t_std_err_sum*1.05))%checks validity of initial ...
        alpha geuss
173     disp(T)
174     %if the initial geuss if off, the following loop should recalculate ...
        the value
175 else while ((t_std_err_sum*0.95)≥t_rms_misfit...
        | t_rms_misfit≥(t_std_err_sum*1.05))
176     alpha_t=(t_std_err_sum/t_rms_misfit)*alpha_t
177     A=b'*b + alpha_t*(c'*c) ;
178     T=A\B ;
179     T_misfit=t-(1/E)*b*T; %misfit vector calcualtion
180     t_rms_misfit=(sum(T_misfit.^2))/numel(T_misfit);
181
182
183     end
184 T
185 end
```